U.PORTO
FEUP FACULDADE DE ENGENHARIA
UNIVERSIDADE DO PORTO
DEPARTMENT OF MECHANICAL ENGINEERING

WHEEL/RAIL MATERIALS FATIGUE CRACK PROPAGATION BEHAVIOUR

DANIEL FILIPE COUTINHO PEIXOTO

2013

DISSERTATION SUBMITTED TO THE FACULTY OF ENGINEERING OF THE UNIVERSITY OF PORTO

FOR THE DOCTORAL PROGRAM IN MECHANICAL ENGINEERING

SUPERVISOR:

PAULO MANUEL SALGADO TAVARES DE CASTRO

CO-SUPERVISOR:

LUIS ANTÓNIO DE ANDRADE FERREIRA

Acknowledgments

D.F.C. Peixoto acknowledges a Calouste Gulbenkian Foundation PhD grant, number 104047-B and the financial support of the Portuguese Government through the Fundação para a Ciência e a Tecnologia - FCT under the project "Railways" PTDC/EME-PME/100204/2008.
The author could not forget to acknowledge also all colleagues and friends that helped and turned the thesis preparation into an interesting and enjoyable time.
In this context, special thanks go to the individuals and entities listed below.

Supervisors:

- Professor Paulo Manuel Salgado Tavares de Castro (supervisor)
- Professor Luis António de Andrade Ferreira (co-supervisor)

The guidance of Professor Professor Jorge H. O. Seabra on the development of the Chapter 9, "Contact fatigue damage on waved surfaces", is noted and gratefully acknowledged.

Co-workers on the FCT project "Railways":

- Mr. Diogo Ramos
- Professor António Castanhola Baptista (CMDRX , FCTUC , residual stress measurements)

Colleagues:

- Ana Ferreira
- André Pinto
- Ana Silva
- Daniel Braga
- Liliana Azevedo

- Sérgio Tavares
- Valentin Richter-Trummer

Co-workers in other areas:

- Mr. Albino A. C. Dias (workshop FEUP)
- Mr. José F. R. de Almeida (workshop FEUP)
- Mr. Miguel A. V. de Figueiredo (LET at FEUP)
- Dr. Pedro M. G. P. Moreira (general help)
- Mr. Rui A. M. da Silva (LET at FEUP)

Involved institutions:

- Faculdade de Engenharia da Universidade do Porto (FEUP), Porto, Portugal
- Faculdade de Ciências e Tecnologia da Universidade de Coimbra (FCTUC), Coimbra, Portugal
- Instituto de Engenharia Mecânica (IDMEC), Porto, Portugal

The support of ALSTOM Spain, providing the AVE train wheel, and the support of REFER, through the Civil Engineering Department of the Faculty of Engineering of the University of Porto, supplying the rail, are gratefully acknowledged.
I would like also to thank Professor José António Martins Ferreira (FCTUC) and Professor Luís Filipe Pires Borrego (ISEC) for supporting the mixed mode loading study, by lending a set of special grips .

Resumo

A maior causa de falhas nos caminhos-de-ferro deve-se à fadiga de contacto. Este tipo de fadiga surge em componentes sujeitos a tensões de contacto variáveis e a falha é causada por fendas que surgem não só à superfície como também no interior dos corpos em contacto, dependendo da magnitude da carga. Os mais importantes tipos de defeitos causados pela interacção roda/carril serão descritos.

Apesar da maioria das falhas que surgem no transporte ferroviários causadas por fadiga de contacto não causarem perda de vidas, são uma origem de preocupações no que diz respeito à manutenção dos equipamentos ferroviários, pois causam paragens para manutenção imprevistas que provocam a diminuição do número de veículos disponíveis para a realização dos diversos serviços e consequentemente atrasos na sua prestação.

O trabalho experimental foi iniciado com a caracterização dos materiais da roda e carril que mais tarde viriam a ser testados. Esta caracterização inclui análise de composição química, determinação das propriedades mecânicas, análise de microestrutura e medições de dureza. Todos estes testes foram realizados em provetes retirados de uma roda de um comboio espanhol de alta velocidade AVE que atingiu o seu limite de desgaste e de um carril de secção UIC60.

Uma máquina de discos, onde é possível simular condições de contacto semelhantes às verificadas no contacto roda/carril real, foi utilizada para testar o comportamento ao desgaste e a resistência à fadiga de contacto dos materiais de roda e de carril estudados. De forma a obter uma caracterização mais completa do comportamento destes materiais, foram realizados ensaios de contacto seco e lubrificado.

Os testes de contacto seco realizados na máquina de discos revelaram que em condições de contacto seco o desgaste é o fenómeno predominante, relativamente à fadiga de contacto. Isto significa que do ponto de vista do estudo de propagação de fendas de fadiga será mais interessante estudar a propagação de uma fenda que teve início no interior do material. Este tipo de fenda também pode ser considerada mais perigoso, já que quando surgem à superfície a sua extensão é completamente desconhecida.

Assim, foram realizados ensaios de medição de velocidade de propagação de fendas de fadiga, seguindo a norma ASTM E647, em provetes extraídos da roda de comboio de alta velocidade espanhol AVE e do carril de secção UIC60. Foram realizados testes com três razões de carga diferente, de forma a obter uma caracterização o mais próximo possível do

comportamento de propagação das fendas em situações de carregamento reais. Foram utilizadas duas abordagens diferentes para determinar o limite de não propagação de fendas de fadiga: *i)* o procedimento experimental *K*-decrescente descrito na norma ASTM E647 e *ii)* o método com K_{max} constante com K_{min} crescente.

Foram também realizados testes de propagação de fendas de fadiga em modo misto (modo I e modo II) em provetes CTS com uma espessura de 9 mm retirados da roda do comboio de alta velocidade espanhol AVE. Estes ensaios serviram para caracterizar o comportamento do material da roda em condições de carregamento misto. Durante estes ensaios mediram-se as velocidades de propagação das fendas de fadiga e a respectiva direcção (ângulo) de propagação.

O ângulo de propagação das fendas de fadiga sujeitas ao carregamento misto medido experimentalmente foi comparado com o angulo de propagação numericamente calculado, de forma a validar as técnicas numéricas utilizadas que foram depois utilizadas em modelos de propagação de fendas de fadiga em rodas de comboio.

Quatro provetes C(T), dois retirados da roda e dois retirados do carril, nos quais foram realizados os ensaios de determinação da velocidade de propagação de fendas de fadiga, foram objecto de medições de espaçamento entre estrias de fadiga. Durante estas medições observou-se que as estrias possuem uma direcção aleatória e que não existe qualquer relação entre a velocidade de propagação da fenda de fadiga e o espaçamento entre estrias.

Além do trabalho experimental, foram tamém realizados trabalhos numéricos, de onde se destacam a simulação em 2D da propagação de uma fenda de fadiga no contacto roda/carril e o estudo paramétrico sobre a influência dos parâmetros de rugosidade e dos parâmetros critério de Dang Van na resistência à fadiga de superfícies rugosas em contacto linear. O estudo paramétrico foi realizado com recurso a uma ferramenta numérica baseada no critério de Dang Van, desenvolvida especialmente para este fim.

Algumas conclusões finais e sugestões para trabalhos futuros que podem servir para completar o trabalho desenvolvido e apresentado nesta tese, serão finalmente apresentados.

Abstract

The most crucial subject in railways' components failure is rolling contact fatigue (RCF). Rolling contact fatigue appears in components subjected to variable contact stress. In this kind of fatigue loading, rupture is caused by cracks that appear not only at the surface but also in the interior of bodies in contact, depending on load magnitude. The most important defects caused by the wheel/rail interaction will be described.

Although most of the failures caused by RCF degradation in railway transportation do not cause casualties involving loss of life, they are a matter of concern since they cause unplanned maintenance interventions, with decreased service availability and delays in train traffic.

The experimental work began with the characterization of the wheel and rail materials to be tested. This material characterization includes chemical composition analysis, mechanical properties determination, microstructure and hardness measurements, performed on samples taken from a Spanish high speed AVE train wheel that reached the geometrical limits for continued usage and from a UIC60 section rail.

An evaluation of the wear and of the rolling contact fatigue resistance of the wheel/rail contact materials, was performed using a twin-disc machine, where the most important dynamic conditions of a real contact can be simulated. Dry and lubricated tests were performed in order to obtain an extended characterization of the contact fatigue behavior of these two materials.

Dry tests, performed on the twin-disc machine revealed that wear is the dominant phenomenon compared to fatigue crack initiation at the contact surface, which means that it could be more interesting to study crack propagation from the interior of the material. These cracks can be more dangerous, since when they appear at the contact surface their extension is unknown.

Consequently, fatigue crack growth rate measurement tests according to the ASTM E647 standard were performed in specimens taken from a Spanish high speed AVE train wheel and from a UIC60 rail. Three different load ratios were used in order to obtain an extended range of crack propagation for different types of loading observed in real operation. Two different approaches were used to determine the fatigue crack growth threshold of these two materials: i) the *K*-decreasing test procedure described in the ASTM E647 and ii) the constant K_{max} with increasing K_{min} method.

Mixed-mode (mode I and mode II) fatigue crack growth tests were also performed on Compact Tension Shear (CTS) specimens with a thickness of 9 mm, taken from a Spanish AVE train wheel to evaluate the fatigue behavior of the wheel steel under mixed mode loadings. Fatigue crack growth rates and the propagation direction (angle) of a crack subjected to mixed mode loading were measured. The crack propagation direction (angle) for the tested mixed mode loading conditions was experimentally measured and numerically calculated, and the obtained results were then compared in order to validate the used numerical techniques that would be used for future numerical models of fatigue crack propagation in wheels.

Striation spacing measurements were performed in four different C(T) specimens, two taken from an AVE wheel and the other two from a UIC60 rail, which were used in fatigue crack growth rate tests. During these measurements it was observed that the striations have a random orientation and no correlation was found between the striation spacing and the fatigue crack growth rate.

Numerical work, also developed, consisted of wheel/rail 2D fatigue crack propagation simulation and a parametric study on the influence of the waviness parameters and Dang Van's criterion parameters on the contact fatigue damage of waved surfaces in line contact.

Some final conclusions and suggestions for future work, that could be done to continue the work developed and presented in this thesis, will be also presented.

Contents

List of Figures

List of Tables

Acronyms and Symbols

Symbols

β	crack propagation angle
Δa	crack length variation
ΔK_{th}	stress intensity factor range threshold
ΔK	stress intensity factor range
ΔP	load range
λ	waviness wavelength
μ	friction coefficient
σ_{-1}	material fatigue limit in reversed bending
σ_h	hydrostatic stress
τ_{-1}	material fatigue limit in reversed torsion
τ_a	amplitude of the shear stress
τ_{Tresca}	Tresca criterion stress

$a_{contact}$	contact width
a_{DV}	non-dimensional constant, which represents the influence of hydrostatic stress on the Dang Van's criterion
amp	waviness amplitude
a	crack length
B	specimen thickness
b	Dang Van's criterion parameter

da/dN	fatigue crack growth rate
F_N	applied normal force
FP	Qiao *et al.* fatigue parameter
K_{II}	mode II stress intensity factor
K_I	mode I stress intensity factor
K_{max}	maximum stress intensity factor
K_{min}	minimum stress intensity factor
K_V	mixed mode equivalent stress intensity factor
P_0	maximum Hertz pressure
Ra	roughness average
Rq	RMS roughness average
R	load ratio
Sa	arithmetical mean height of the surface
Sq	RMS height of the surface
s	striation spacing
W	specimen width
Z_s	depth of the maximum the Tresca stress value

Acronyms

AAR	Association of American Railroads
ADI	Austempered Ductile Iron
ASTM	American Society for Testing and Materials
AVE	Alta Velocidad Española
BS	British standard
C(T)	compact tension specimen
CEMUP	Centro de Materiais da Universidade do Porto

CETRIB	Unidade de Tribologia e Manutenção Industrial do INEGI
CMDRX	Centro de Estudos de Materiais por Difracção de Raios-X
CTS	Compact Tension Shear specimen
EDM	Electric Discharge Machining
EN	European standard
FCG	Fatigue crack growth
FCGR	Fatigue crack growth rate
FCTUC	Faculdade de Ciências e Tecnologia da Universidade de Coimbra
INEGI	Instituto de Engenharia Mecânica e Gestão Industrial
ISEC	Instituto Superior de Engenharia de Coimbra
LET	Laboratório de Ensaios Tecnológicos, FEUP
MCL	Modified Crack Layer
MERR	Maximum Energy Release Rate
MTS	Maximum Energy Release Rate
RCF	Rolling Contact Fatigue
SEM	Scanning Electron Microscope
UIC	Union Internationale des Chemins de Fer
VCCT	Virtual Crack Closure Technique
VDI	Association of German Engineers
XFEM	Extended Finite Element Method

Chapter 1

General Introduction

The most crucial subject in railways' components failure is rolling contact fatigue (RCF). Rolling contact fatigue appears in components subjected to variable contact stress. In this kind of fatigue loading, rupture is caused by cracks that appear not only on the surface but also in the interior of the bodies in contact, depending on load magnitude. In general, a complete RCF load cycle involves changes in the principal stresses' orientation.

It is clear that the analysis of rolling contact fatigue defects on rails is more complicated than on wheels because of greater randomness and deviations in acting loads, contact geometries and fatigue strengths. The rolling contact fatigue problem in railway components is dealt in, *e.g.*, refs. [1, 2, 3, 4, 5].

The fatigue analysis of contact problems is a very complex problem since it implies the analysis of a multiaxial stress state. To solve this issue multiaxial fatigue criteria can be used to calculate an equivalent stress which can be compared with material parameters obtained by uniaxial tests. Among others, Dang Van proposed in [6] a criterion to establish an equivalent stress based on the analysis of local stresses distinguishing the macroscopic stresses, in the scale of the mm, from the mesoscopic stresses at the scale of a few grains of the material.

Some aspects such as wear, corrosion, and surface corrugation, affect components fatigue life and must be considered in this type of fatigue behavior. The most important defects caused by the wheel/rail interaction will be described the following paragraphs.

It has been shown by Donzella *et al.* in [7] that there is a competition between fatigue crack propagation and wear. Improving material wear resistance implies a reduction of the maintenance costs, increasing grinding intervals and extending the rail life but it also increases the risk that small cracks are not worn away and can grow to a critical size causing rail failure.

Although most of the failures caused by RCF degradation in railway transportation do not cause casualties involving loss of life, they are a matter of concern since they cause unplanned maintenance interventions, with decreased service availability and delays in train traffic.

The regions of wheel and rail most affected by RCF are presented in Figure 1.1.

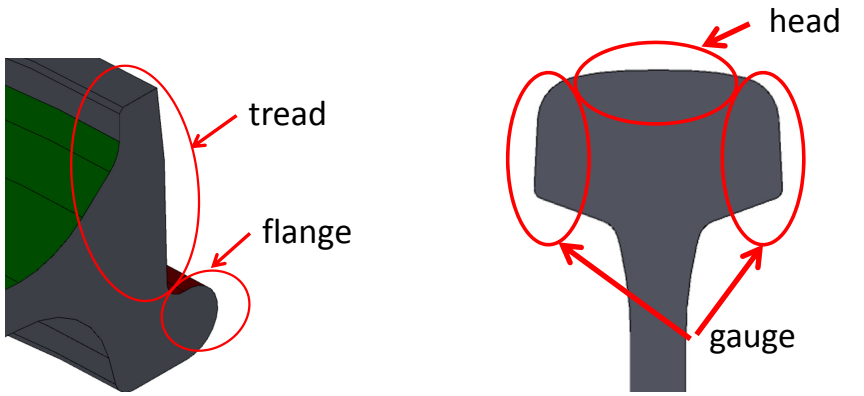

(a) Wheel parts most affected by RCF.

(b) Rail parts most affected by RCF.

Figure 1.1: Wheel and rail parts most affected by RCF.

1.1 Wheel and rail typical defects

Wheel and rail defects are caused by several phenomena such as heat generation, fatigue, wear and impacts [8], as shown in Figure 1.2.

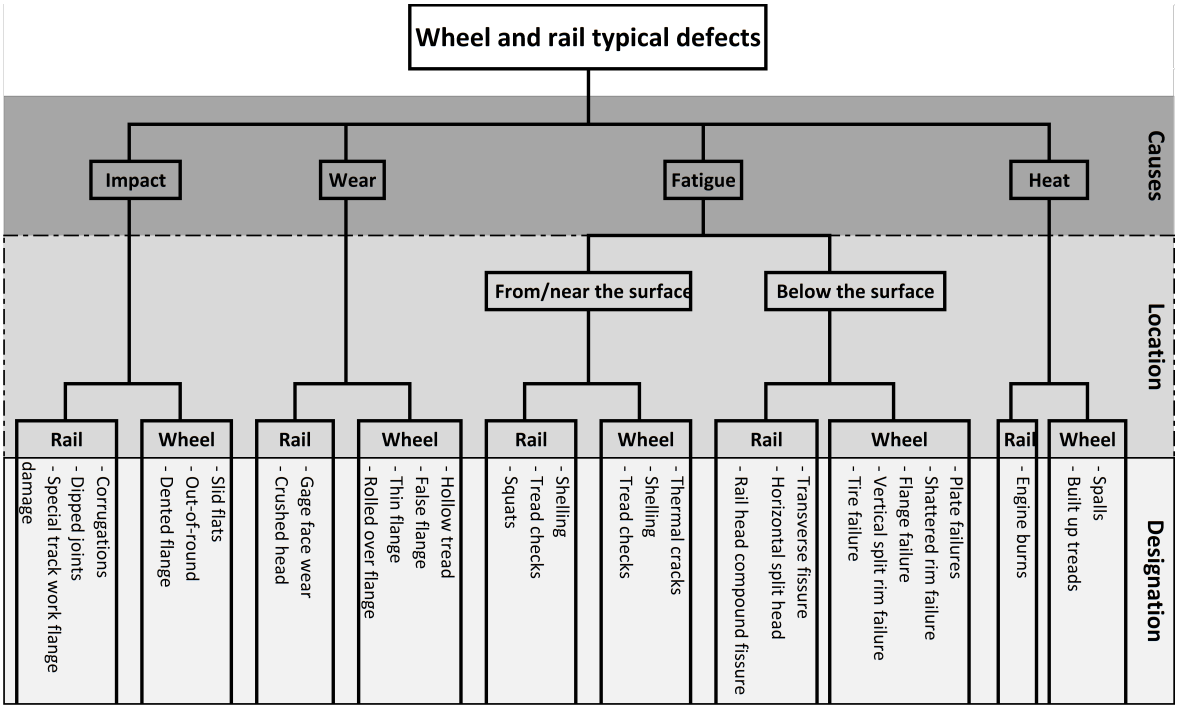

Figure 1.2: Wheel and rail typical defects causes, [8].

Heat, generated by sliding or spinning, can cause spalls and *build up treads* on wheels and *engine burns* on rails. Spalls are initiated from wheel surface martensite spots caused by rapid heating and cooling during wheel sliding. They occur more frequently in winter or wet

conditions due to lower wheel/rail adhesion and accelerated crack propagation due to water trapped in cracks.
Figure 1.3 shows the appearance of a spall and a micrograph picture of a section through a spall, where the white area at surface is martensite.

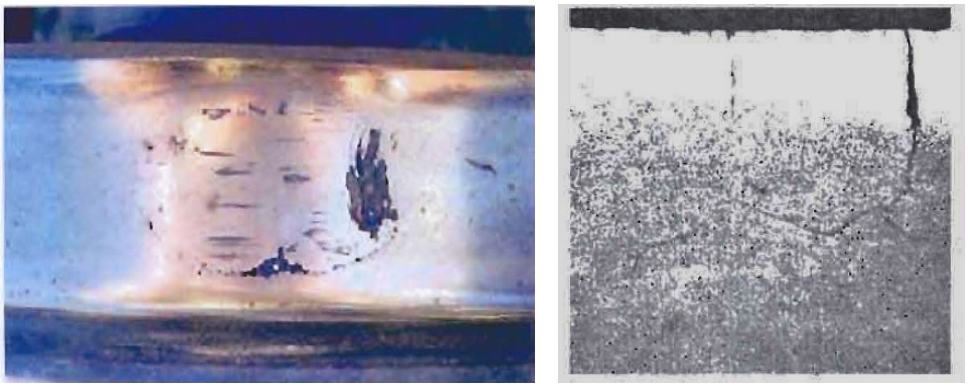

(a) spall appearance (b) Micrograph of section through spall

Figure 1.3: Spall, [8].

Wheel tread metal build up occurs on wheels when rail debris are welded to wheel tread due to heavy braking. They occur more frequently during wet and winter conditions. The mechanism of tread metal pick is currently not well understood [8].
Wheel spinning promotes the appearance of engine burns, which consist of a layer of martensite that will eventually crack and may develop into a transverse defect.
Fatigue defects can be originated below the surface or from surface. Defects originated below the wheel surface are plate failures, shattered rim defects, flange failures, vertical split rim failures and tire failures. Some pictures of these defects are shown in Figure 1.4c.

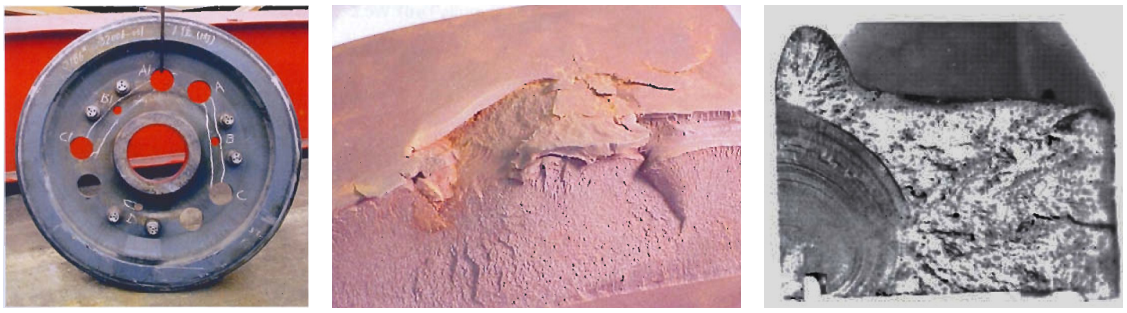

(a) Plate failure (b) Vertical split rim failure (c) Tire failure

Figure 1.4: Fatigue defects originated below the wheel surface, [8].

Plate failures appear as circumferential cracks entirely within the wheel plate, initiated by a fatigue crack from a stress concentration, such as a hole, improper machining groove or

dent. Most of them occur in wheels with a plate thickness below specified minimum. The fatigue crack will eventually trigger a brittle fracture if not removed.

Shattered rim defects are deep shelling and spread rims. They typically initiate in forged wheels at aluminum oxide inclusions or in cast wheels voids and tend to occur in worn wheels. Their initiation is accelerated by impact loading.

Flange failures typically initiated by flange striking on rail.

Vertical split rim failure is a brittle fracture originated from wrecked rims, surface shell, or a spall.

The existence of a false flange produces a bending moment on the rim gauge side.

Tire failure is also a brittle fracture originated from stress concentration, internal defect and tensile stress caused by tight assembly.

Therefore, the rail defects originated below surface are transverse cracks, horizontal split rail head and rail head compound crack.

Rail transverse cracks are caused by fatigue cracks originated from hydrogen embrittlement, alumina or silicate inclusions. Horizontal split rail head is a longitudinal fatigue crack originated from an alumina-manganese oxide stringer or seam. Rail head compound crack is a combination of horizontal and transverse cracking which begins as a rail horizontal split head defect, but turns into a transverse direction.

As mentioned before, fatigue defects can also initiate at the surface or near surface. On the wheel, these defects are thermal cracks, shelling and tread checks and on the rail are shelling and tread checks, also, and squats.

Thermal cracks are radial fatigue cracks that initiate by thermal fatigue, metallurgical damage or surface ratcheting. They grow if the circumferential residual compressive stresses imparted during manufacture are reversed by excessive brake heat input. Attention should be paid to tires that have tensile stresses from mounting[1]. These cracks will eventually trigger a brittle fracture if not removed.

Shelling is a subsurface initiated rolling contact fatigue defect. It initiates under multiple action of tangential stresses predominantly at stringers of oxide inclusions in the wheel steel. The critical metallurgical factor contributing to the initiation of shells is the oxide volume of fraction and length. Mechanical factors, such as normal, lateral and traction loads and residual stresses, also contribute to the development of shells. The visual appearance of these defects is similar to spalls, as can be seen in Figure 1.5. In this figure a non-metallic inclusion at top center can be seen. The typical depths of shell cracks are 4-6 mm and there are traces of fatigue cracks.

[1] As in interference or shrink fits.

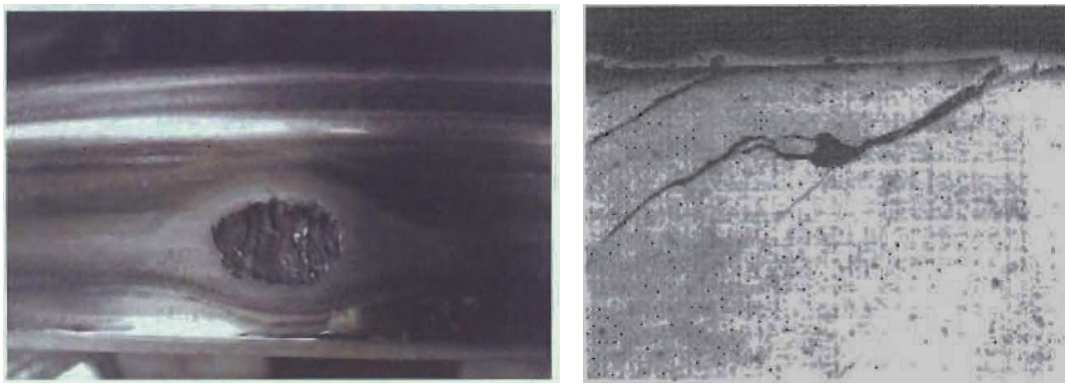

(a) Shelling appearance. (b) Micrograph of section through a shell

Figure 1.5: Shelling pictures, [8].

Tread checks initiate at the wheel tread surface as a consequence of large unidirectional plastic strains. These strains arise from an incremental accumulation of plastic strain during each cycle of wheel/rail loading. Accumulation of a large number of unidirectional strain increments ratchet the surface layer of wheel material until its ductility is exhausted. Cracks initiated by ratcheting grow perpendicular to the prevailing direction of the traction force. The critical conditions for initiation of cracks are a high ratio of the normal contact stress to the material strength and a high ratio of the tangential to the normal load.

Figure 1.6: Picture of a tread checks, [8].

Shelling defects on rails are caused by plastic flow and shearing due to gauge corner overloading and occur most frequently in curves, but will also appear in tangent track.
Rail head checks can be found at the gauge corner of high rails of curved tracks and on both rails of straight tracks. They appear in an angle of 45° relatively to the running direction. Head checks do not happen at very sharp curved tracks where gauge face wear severely due

to large lateral forces between rails and wheels. The hunting motions [9] of bogies rises lateral forces on gauge corners of rails of straight tracks causing rail head checks. Rolling contact fatigue resulting from non-conformal wheel or rail profiles, high adhesion conditions, loading from operation at incorrect balance speed or increased contact stresses at false flanges causes also rail head checks. A picture of a rail head check is shown on Figure 1.7.

Figure 1.7: Rail head check, [8].

Rail squats are rolling contact fatigue defects associated with the operation of trains, not only high speed, from 200 to 300 km/h, but also medium speed around 100 km/h. Squats can initiate at the rail surface or shallow rail subsurface horizontal crack below running surface which initiate a transverse defect.

Wear and/or improperly steering bogies can originate hollow tread, false flange appearance, thin flange and rolled over tread defects on train wheels. They also can originate rail gauge face wear and crushed rail head.

Hollow tread and false flange are caused by improper bogie steering, operation on rails with narrow heads or continuous running on tight gauge track. Hollow treads will accelerate degradation along the field side of low rails. Hollow treads will cause negative wheelset yawning in curves, leading to increased high-rail side-wear. Hollow treads can also cause rail and wheel shelling, and accelerate degradation at open throat crossings.

Figure 1.8: Hollow tread and false flange on a train wheel, [8].

Thin flanges results from curving on small radius tracks or improperly steering bogies.
If the outer edge of the tread spreads beyond the vertical face of the rim it can cause a rolled over tread defect. Usually this is associated with bogie misalignment, improperly machined wheels, excessive hollow wear and wheel tread contact at points and crossings. The opposite wheel usually has a thin flange defect.
Rail gauge face wear may be the result of normal wear in areas of sharp curvature, the result of operating trains at over balance speed (high rail) or poorly steering bogies if there is Gage face wear in tangent track.
Some defects are caused or result from impacts. These are wheels slide flats, out-of-round wheels, wheel's dented flange, rail long wave length corrugations, rail short pitch corrugations, rail dipped joints and rail flange damage.
Slide flats are caused by wheel slides. They will eventually cause out-of-round wheel if left in service.
According to [8], out-of-round wheels defects can be classified as type A, tread defect initiated, or type B, polygonization. The tread defects initiated are produced when spalls, shells, and slid flats that are pounded out during service. They will also facilitate the initiation of shattered rims. The out-of-round defects type B produce a series of corrugation like non homogeneous wear around the circumference of the wheel and are produced by dynamic action of an non concentric mounted wheel, a new wheel machined out-off center, from an axle with its center off by a machining error or a worn axle center, non-uniform wheel rim hardness or non-uniform brake application.
These defects are usually not observable. However, they produce high impacts when passing over impact load detectors and produce a characteristic thumping with train passage.
A high flange striking the rail flange of special track work, or the rail flange of a special track work that have not sufficient depth, can cause a dented flange defect.
Long wave length corrugations are originated by vertical resonance (typically triggered from vertical track irregularity) that develops from subsequent plastic flow in troughs. This type

of corrugation, whose wavelengths are in the range 500 to 1200mm, can be found in straight tracks and curved tracks where high speed and medium speed trains are operated. The wavelength is related with the train speed and natural frequency of unsprung mass of vehicle supported with track stiffness.
Short pitch corrugations, as the ones shown on Figure 1.9, can be formed at low rails in sharp curved tracks whose radii of curvature are mostly less than 400m. Lateral forces interacting on running surface between wheels and rails can have the most significant influence on this type of defect formation.

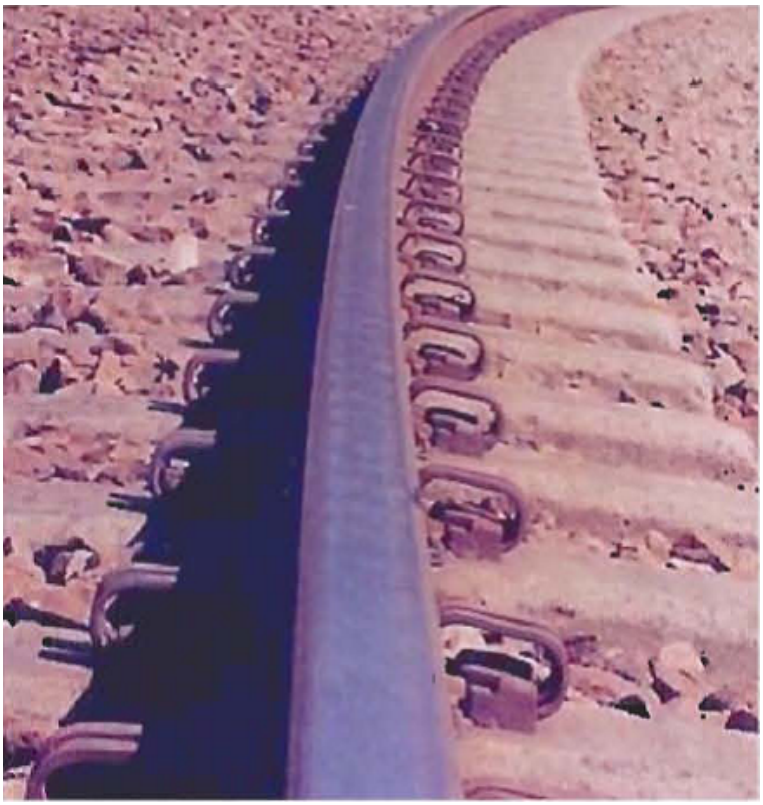

Figure 1.9: Short pitch corrugations, [8].

However, this type of corrugations can be found in straight tracks where medium speed trains are operated. The cause of this type of corrugation is not clearly understood, but it is theorized that troughs are worn from oscillations due to torsional wheel set resistance, traction creepage, vertical resonance, lateral creepage and torsional twist on the low rail.
A dipped joint occurs due to the lower hardness of the weld metal in the case of aluminothermite welds or in the heat-affected-zones of flash butt welds.

1.2 RCF of railway wheels - failure characterization

Railways' wheels may fail in several ways as shown in the section 1.1. Mechanisms related with cracks initiation and growth, due to wheel tread surface rolling contact fatigue, will be

presented in more detail in the next paragraphs.
Fatigue failures due to rolling contact fatigue in railway wheels can be categorized as surface initiated defects or subsurface initiated defects.

Surface initiated defects

These surface initiated defects are normally caused by gross plastic deformation of the wheel material close to the running surface, due to repeated applications of high friction loads as consequences of traction, braking, curving, etc.
If that deformation occurs in a dominant direction the material will harden and when residual stresses are not sufficient to prevent further accumulation of plastic strains and fracture strain is exceeded, cracks will eventually appear. That phenomenon explains the benefits of the residual compressive stresses on the wheel tread[2]. Such a mode of fracture is referred to as ratchetting, the defect caused is referred as tread checks, and is frequently studied in twin-disc tests.
On the other hand, if the frictional loading has an alternating direction, as an example the alternating between braking and traction, the material will not ratchet in the same manner, since plastic deformations will occur in both directions, causing accumulated plastic strain close to zero. In this case fatigue will be caused by low-cycle fatigue.
Surface initiated cracks at first grow at a shallow angle, corresponding to the texture of the plastically deformed surface material, and next deviate into an almost radial direction. At a depth of about half a millimeter, the crack will tend to deviate (or branch) towards a circumferential direction, as shown in Figure 1.10

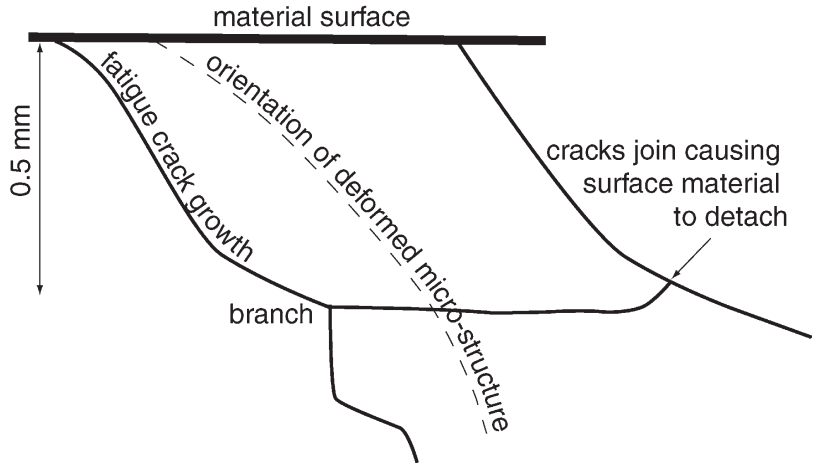

Figure 1.10: Schematic representation of growth of surface initiated fatigue cracks in wheels, [1].

[2]These compressive stresses are obtained with water projection into the wheel tread, which promotes a faster cooling.

Final fracture normally occurs as a new branching of the crack onto the surface, causing material removal. However, it can be possible that the crack grows in the radial direction, towards the hub.
The influence of lubrication in surface initiated cracks growth must be considered [10, 11, 12]. However, lubrication is referred in a wide sense including several fluids which may enter the crack such as water, grease, oil, etc.
Three possible mechanisms to explain the role of lubrication in crack propagation have been presented in [11]:

1. crack face lubrication which decreases crack face friction and increases the crack driving forces.

2. the influence of a fluid forced into the crack distributing the contact pressure acting on the fluid at the crack mouth to a 'hydraulic pressure' on the crack faces. This effect will also prevent crack closure.

3. the influence of a trapped fluid as shown in Figure 1.11. This effect causes a marked increase in the mode I stress intensity factor.

Figure 1.11: Mechanism of crack propagation due to hydrostatic pressure, [10].

The influence of lubrication in surface initiated crack propagation is a matter of different opinions, but is supported by several empirical findings such as large seasonal variations in wheel reprofilings to eliminate cracks [13] and greater number of cracks growing in the motion direction, reflecting the influence of the presence of water on rails. Cracks initiated on wheels' surface will be opened by a braking torque, allowing lubricant to enter the crack and will be closed by traction.
The phenomenon of a major number of cracks growing in the motion direction is explained by the fact that the lubricant will be squeezed out of the crack in the opposite direction of the motion, see Figure 1.11, and the altered sequence of loading [11].
The influence of lubrication in crack growth, described before, enforces the idea that usage of lubrication to reduce friction, and consequently the risk of crack initiation, must be made carefully.

Subsurface initiated defects

Rolling contact fatigue failures in railway wheels, also, can be caused by subsurface defects, when there are moderate surface friction coefficients ($\mu < 0.3$).

In-field observations lead to conclude that subsurface defects can initiate at depths between 3 and 25 mm, depending on material characteristics. However, in numerical analysis [14], where the material is considered to be homogeneous and isotropic, fatigue failure is predicted at a depth of 3 to 5 mm. This observation leads to conclude that the initiation of cracks below the wheel tread is promoted by the presence of material heterogeneities, or material defects which cause very high localized stresses. But other factor must be considered to the initiation of such type of defects, as residual compressive stresses at the surface due to manufacturing and material hardening, which tends to suppress fatigue initiation on the surface.

Kabo argued in [4] that cracks are less likely to initiate from manganese sulphide (MnS) due to its small size, but a crack already initiated would easily grow through it. Unfortunately, this hypothesis is difficult to verify by metallographic examinations, since manganese sulfide-inclusions are soft and thus likely to wear off by the action of compressive and shear loads during the process of crack propagation.

Subsurface initiated fatigue cracks propagate in the radial direction towards a depth of about 20 mm. At this depth it will deviate into circumferential propagation. Until final fracture, cracks can growth between 15 and 300 mm. As happen with the surface initiated cracks, final fracture of subsurface initiated cracks occurs as a branching of the crack to the surface, or, more rarely, towards the wheel hub.

Chapter 2

Work motivation

Fatigue and wear are the most important aspects that must be analyzed in the wheel/rail interaction.
The quality of the rail and wheel running surfaces and the track geometry quality are of high importance on the wheel/rail interaction forces and consequently contribute to track damage and geometry deterioration. The rolling stock speed on track also has a great importance on the wheel/rail interaction forces magnitude.
On train wheels fatigue cracks can appear on the tread surface and also near the tread surface. Rolling contact fatigue defects appearance and growth can be reduced with preventive maintenance of rails, through the use of grinding, and on wheels through re-profiling.
Wear of rails and wheels can be reduced by lubrication of the wheel flange, which reduces the friction between the wheel flange and rail gauge.
At the beginning, the aim of this work was to use a twin-disc machine to simulate the most important dynamic conditions of the wheel/rail real contact and then study the initiation and propagation of fatigue cracks in the wheel and rail materials, taking into consideration the evolution of the residual stress of the specimens.
However, the twin-disc tests performed revealed a high wear rate of these two materials in dry contact, which removes any crack/defect that may appear at the contact surface, the only cracks that could be identified using the available laboratory means.
Subsequently it was decided to change the main objective of the present work to study the propagation behavior of fatigue cracks that appears in a generic way, not specifically identified in the present work, performing fatigue crack growth tests in mode I according to the ASTM E647 standard. Fatigue crack propagation threshold tests were also performed as mixed mode (I+II) tests.
Using some of the obtained experimental results, a 2D numerical simulation on the propagation of fatigue cracks on the wheel was performed.
The initiation of cracks was addressed concentrating the attention on the roughness of the contact surfaces, and a numerical tool based on the Dang Van's criterion was developed to predict fatigue damage initiation on waved contacts. This numerical tool was then used to

study the influence of the material fatigue parameters and waviness wavelength and waviness amplitude on the fatigue resistance of the bodies in contact.
In the following chapters all performed tests and their results will be presented and discussed.

Part I

EXPERIMENTAL WORK

Chapter 3

Material characterization

The experimental work of this thesis began with the characterization of the wheel and rail materials that will be tested.
This material characterization includes chemical composition analysis, mechanical properties determination, microstructure and hardness measurements, performed on samples taken from an Spanish high speed AVE train wheel and from a UIC60 section rail. It should be mentioned that the AVE train wheel is a used wheel that reached the geometrical limits for continued usage as can be seen in Figure 3.1.
ALSTOM Spain provided the AVE train wheel, and REFER, through the Civil Engineering Department of the Faculty of Engineering of the University of Porto, the rail.

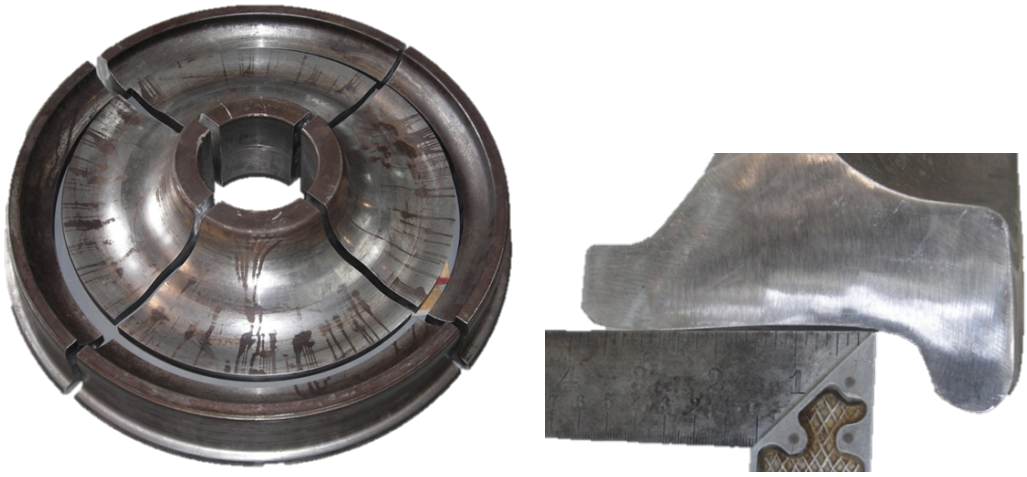

(a) AVE train wheel cut. (b) Worn wheel profile.

Figure 3.1: AVE train wheel pictures.

3.1 Materials used to manufacture railway wheels and rails

Steels used for the manufacture of railway wheels and rails are classified as carbon steels. Railway wheel materials within the 'carbon steel' group are generally classed as low carbon steel (Carbon %<0.30), medium carbon steel (0.3< Carbon % <0.6) with some wheel steels classed as high carbon (0.6< Carbon % <1.0).

A high carbon content raises the hardness of the wheel and makes it more wear and RCF resistant. Unluckily, high carbon content makes the wheel much more susceptible to the thermal effects of braking and slip, because it is easier to produce brittle martensite, a phase that is more susceptible to thermal cracking, especially when tread braking is used. The resistance of the wheel to brittle fracture is reduced as the carbon content increases [15].

The choice of a particular wheel grade steel is dependent among other factors upon its usage (locomotives, passenger trains, high speed trains, etc.) and braking mechanism. The rail plays a very vital role in the reliability of the railway system.

The rail steel chemical composition, especially the carbon content that increases the tensile strength and hardness and decreases the ductility of the rail steel, is of high importance since it determines the rolling contact fatigue and wear resistance of the rail. Hence various percentage of carbon contents are tried to produce different types of rails in order to obtain the most appropriate rail steel for all different applications of rails (crossings, straight railway lines, curves, etc.). In rail steels it is common to find a carbon percentage between 0.60% and 0.80% depending on the grade of the rail steel [16].

Apart of iron, which is obviously the main constituent in any steel, carbon steels are combinations of carbon with manganese, silicon, sulphur, aluminum, chromium, molybdenum and vanadium. In addition, steel may contain oxygen (if not completely oxidized), traces of nitrogen and hydrogen etc. The effects these elements will be discussed below.

Manganese increases the strength and improves toughness, but it also makes the wheel more susceptible to thermal cracking [15]. It also improves the depth of hardening, important in wheels and rails throughout their service life, through many wheel reprofilings and rail grinding [15, 16]. Manganese also increases high temperature strength.

In a similar way silicon also increases high temperature strength and the hardenability of the steel. However, silicon is normally used as a deoxidant, to reduce the steel oxygen level. The increase of silicon content reduces ductility and impact resistance of the steel [15].

To help control hydrogen cracking sulphur is controlled or added during steelmaking in mainly non-vacuum degassed steels. Sulphur is also added to make the machining easiest has it allows the swarf to break more easily [15].

Aluminum is added to steels to develop a fine grained structure and this is generally found to be advantageous, has it improves strength, toughness and fatigue resistance [15].

Chromium and Molybdenum are added to improve wear resistance and form very hard wear

resistant stable carbides in the steel. Chromium and molybdenum both increase high temperature strength [15].
Vanadium promotes the formation of stable carbides, fine grained structure, toughness, ductility and mechanical strength [15].
Sometimes, some residual elements are added deliberately to carbon steels to improve certain properties on the wheel, however their usage as alloys increases the cost of the steel, especially the addition of nickel [15].
The addition of elements such as copper, aluminum, silicon and chromium improve the steel corrosion resistance. These elements form thin, dense and adherent oxide films which protect the surface of the steel from oxidation [16].
Table 3.1 shows the chemical composition and Table 3.2 presents the mechanical properties of some railways wheel steel grades used to manufacture wheels for locomotives, high speed passenger trains with disc brakes or tread breaks. The EN13262 standard was considered but there are other equivalent standards, as the British standard BS5892, American standard AAR M107 among others that could be considered.

Table 3.1: Maximum values of wheel steel chemical elements in % weight according to the EN 13262 standard.

Grade	ER6	ER7	ER8
C	0.48	0.52	0.56
Si	0.40	0.40	0.40
Mn	0.75	0.80	0.80
P	0.02	0.02	0.02
S	0.015	0.015	0.015
Cr	0.30	0.30	0.30
Cu	0.30	0.30	0.30
Mo	0.08	0.08	0.08
Ni	0.30	0.30	0.30
V	0.06	0.06	0.06

Table 3.2: Wheel steel mechanical properties according to the EN 13262 standard.

Grade	ER6	ER7	ER8
σ_Y [MPa]	>500	>520	>540
σ_U [MPa]	780-900	820-940	860-980
A [%]	15	14	13
$Hardness$ [HB]	>225	>235	>245

Table 3.3 and Table 3.4 shows the chemical composition and the mechanical properties of some rail steel grades. In this case the EN 13674 standard was considered but, similarly with what was said for the railway wheel steel grades, there are other equivalent standards, as the UIC 860 and British standard BS 11:1965[3] among others that could be considered.

Table 3.3: Rail steel chemical elements in % weight according to the EN 13674 standard.

Grade	R200	R260	R260 MN	350 HT	350 LHT
C	0.40-0.60	0.62-0.80	0.55-0.75	0.72-0.80	0.72-0.80
Mn	0.70-1.20	0.70-1.20	1.30-1.70	0.70-1.20	0.70-1.20
Si	0.15-0.58	0.15-0.68	0.15-0.60	0.15-0.58	0.15-0.58
P	<0.035	<0.025	<0.025	<0.02	<0.02
S	0.008-0.035	0.008-0.025	0.008-0.025	0.008-0.025	0.008-0.025
Ni	<0.10	<0.10	<0.10	<0.10	<0.10
Mo	<0.02	<0.02	<0.02	<0.02	<0.02
Al	<0.004	<0.004	<0.004	<0.004	<0.004
Cr	<0.15	<0.15	<0.15	<0.15	<0.30
V	<0.03	<0.03	<0.03	<0.03	<0.03
N	<0.009	<0.009	<0.009	<0.009	<0.009
Cu	<0.015	<0.015	<0.015	<0.015	<0.015
Nb	<0.01	<0.01	<0.01	<0.01	<0.01

Table 3.4: Rail steel mechanical properties according to the EN 13674 standard.

Grade	R200	R260	R260 MN	350 HT	350 LHT
σ_Y [MPa]	-	-	-	-	-
σ_U [MPa]	>680	>880	>880	>1175	>1175
$elongation$ [%]	>14	>10	>10	>9	>9
$Hardness$ [HB]	200-240	260-300	260-300	350-390	350-390

3.2 Microstructure found in railway wheels and rails materials

When carbon steels had, at room temperature, 0.8% of carbon they are called eutectoid steels and their microstructure is fully pearlitic. At lower carbon contents, less than 0.8%, the microstructure is composed of pearlite with free ferrite areas. Above 0.8% carbon, the cementite phase occurs.

[3]Replaced by EN 13674-1:2003+A1:2007, replaced by BS EN 13674-1:2011.

According to this, and considering the most common percentage of carbon content in railway wheels and rails steels the most common microstructure is the pearlitic.
However in lower/medium carbon railway wheels steels (Carbon % <0.6) a ferrite phase can also be found, which adds more resilience and impact resistance to the wheel. Other alternative railway wheels microstructures have been studied but "it appears that pearlitic steels offer the best performance, are inexpensive and are well understood" [15].
On the other hand, the need to obtain rails with higher wear resistance, since the limit to the hardness that can be reached with pearlitic steels was reached, lead to develop other rail steels microstructures such as bainite that are harder than pearlite and could improve rail wear performance [17] and mechanical properties [18]. These rail steels are low carbon steel, Mn-Cr-Mo-V and in some cases they can have little addition of nickel [18].

3.3 Experimental results

Chemical composition

The chemical composition of the studied wheel steel, presented in Table 3.5, was performed on samples taken from the AVE and the chemical composition of the studied rail steel, presented in Table 3.6, was performed on samples taken from a UIC60 section rail. These chemical compositions were obtained at the INEGI's Laboratory of Mechanical Testing by optical emission spectrometry, using a SPECTRO's SPECTROLAB M7 spectrometer.

Table 3.5: Wheel material chemical composition [% weight].

C	Si	Mn	P	S	Cr	Cu	Mo	Ni	V	Al
0.49	0.25	0.74	0.01	<0.005	0.26	0.12	0.06	0.18	<0.005	0.03
Ti	W	Pb	Sn	As	Zr	Ca	Sb	B	Zn	Fe
<0.001	<0.01	<0.003	<0.01	<0.01	<0.002	<0.003	<0.002	<0.0001	<0.003	97.8

Table 3.6: Rail material chemical composition [% weight].

C	Si	Mn	P	S	Ni	Mo	Al	Cr	V	Cu
0.72	0.35	1.1	0.02	0.01	0.02	<0.001	<0.005	0.02	<0.01	<0.01
Ti	W	Pb	Sn	As	Zr	Ca	Sb	B	Zn	Fe
0.02	<0.01	<0.005	<0.005	<0.01	<0.002	<0.001	<0.002	<0.0001	0.01	97.7

The chemical composition presented in Table 3.5 shows that we are dealing with a railway wheel material within the medium carbon group steel with 97.8% of Fe and 0.49% of C in which the principal chemical components are the Si, Mn, Cr, Ni and Cu. In the case of the

rail material chemical composition obtained, presented in Table 3.6, the rail steel is a carbon steel with 97.7% of Fe and 0.72% of C and has as principal chemical components Si and Mn.

Microstructure and hardness

The microstructure of the studied wheel and rail materials was observed using an optical microscope. A 2% nital solution was used as a reagent to obtain contrast between the different phases that can be identified in this type of materials. The microstructures are shown in Figure 3.2, where the average hardness of the observed samples, two for each material, is also recorded.

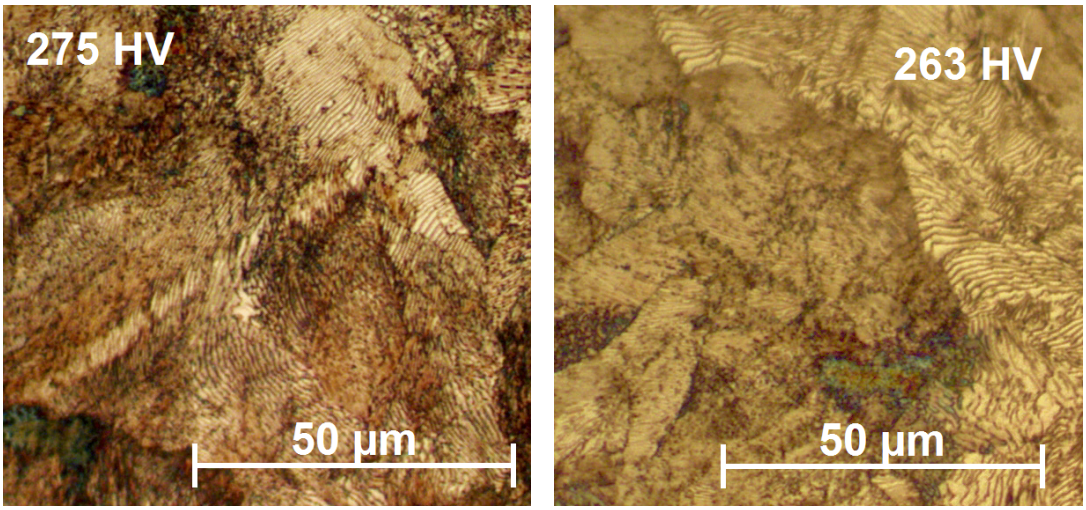

(a) wheel microstructure (b) rail microstructure

Figure 3.2: Studied materials microstructure.

From these analysis it can be concluded that the studied materials present a pearlitic microstructure.

It was expected that the rail material hardness would be higher than the wheel material, due to the higher carbon percentage, but this was not verified. In order to understand these results it was decided to perform several hardness measurements in a wheel cross-section sample to obtain the hardness distribution.

Analyzing the obtained hardness distribution and the location where the wheel material samples used to observe the microstructure were taken, shown in Figure 3.3, it can be concluded that the higher hardness value is due to the fact that the sample was taken from an out-of-service wheel in a zone where the material was hardened by usage.

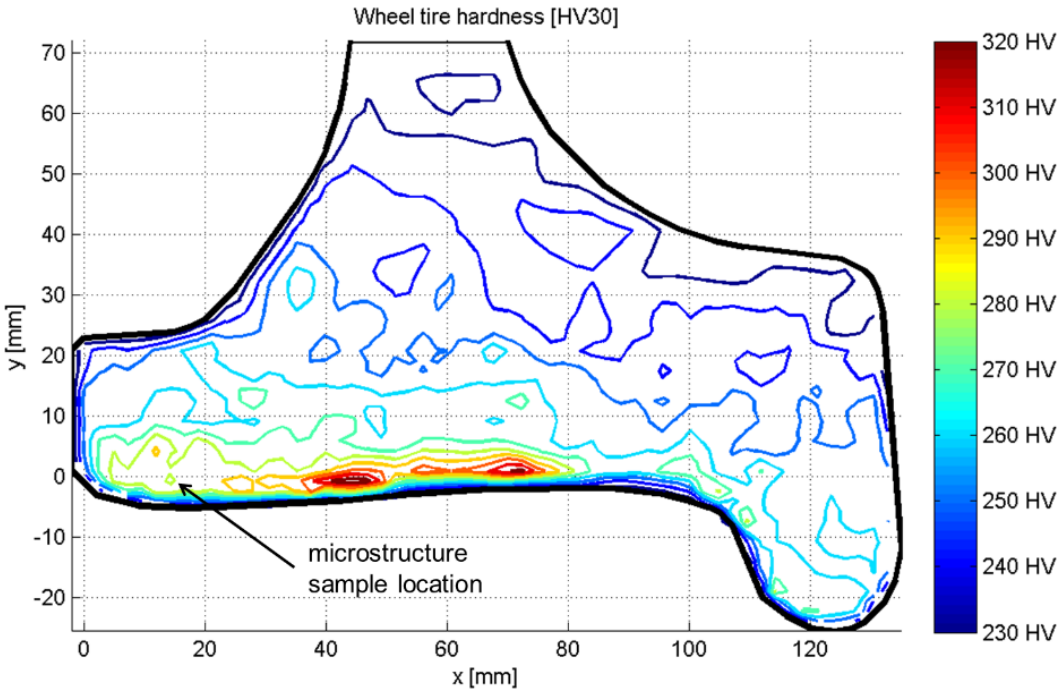

Figure 3.3: Wheel hardness distribution.

Mechanical properties

Tensile tests according to NP EN 10002-1 standard were made with the studied materials, using round cross-section specimens with Ø10mm with M16 threaded grips, see Figure 3.4. The specimens were extracted from the wheel tire in the tangential direction and from the rail head in the longitudinal direction, as shown in Figure 3.5.

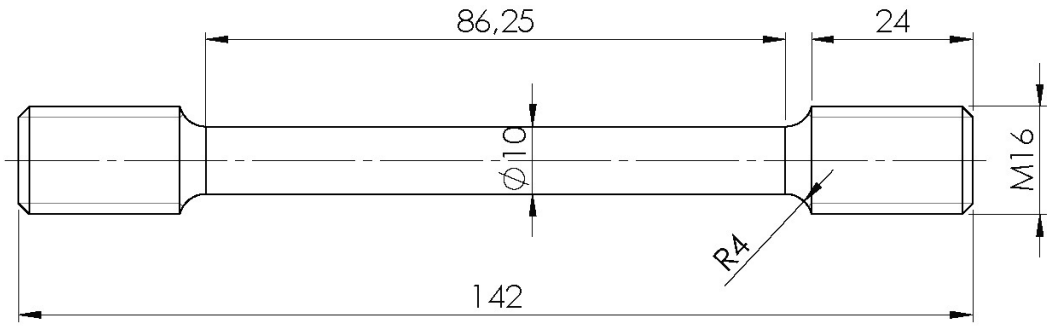

Figure 3.4: Tensile specimen dimensions.

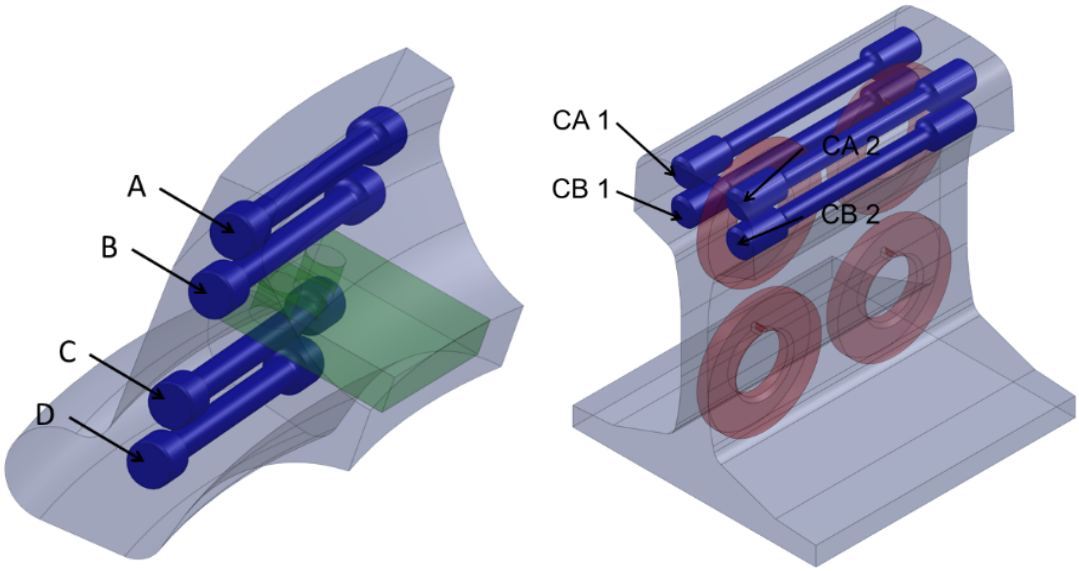

(a) wheel tensile specimens location. (b) rail tensile specimens location.

Figure 3.5: Tensile specimens' location.

The tensile tests were performed on an MTS® servo-hydraulic testing machine with 100kN of maximum capacity and at a displacement rate of 1mm/s.
The monotonic behavior of the wheel and rail materials is shown in Figure 3.6 and Figure 3.7, respectively. The corresponding mechanical properties are listed in Table 3.7, for the wheel and in Table 3.8 for the rail.

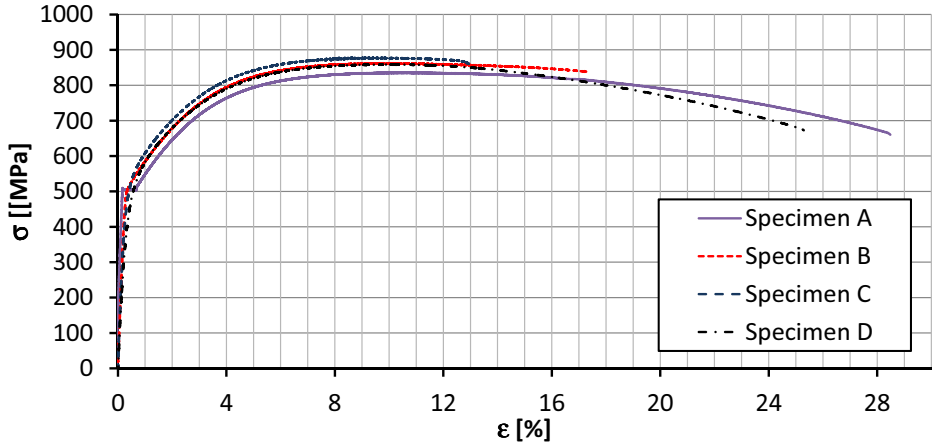

Figure 3.6: Monotonic σ *vs.* ε curves for wheel tensile specimens.

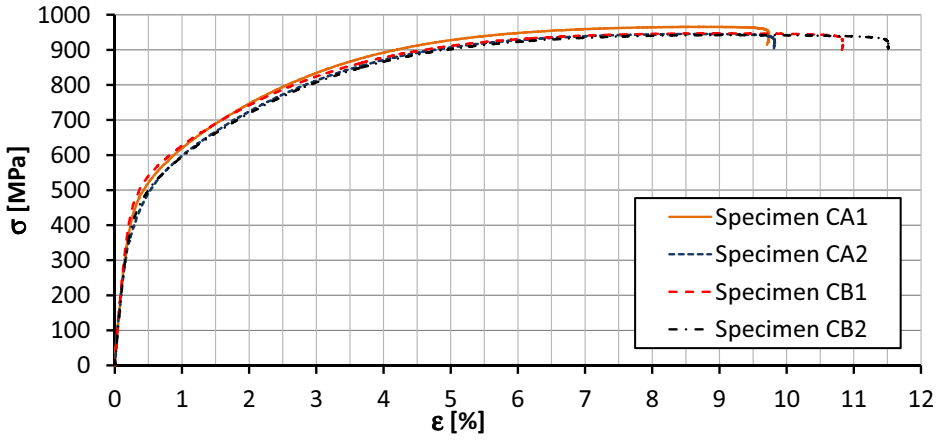

Figure 3.7: Monotonic σ *vs.* ε curves for rail tensile specimens.

Table 3.7: Wheel material mechanical properties.

Ref.	A	B	C	D	average
E [GPa]	213	199	203	173	197
σ_Y [MPa]	506	520	516	469	503
σ_U [MPa]	835	861	879	859	859
ε	20%	19%	17%	16%	18%

Table 3.8: Rail material mechanical properties.

Ref.	CA1	CA2	CB1	CB2	average
E [GPa]	191	157	218	199	191
σ_Y [MPa]	513	495	525	483	504
σ_U [MPa]	966	946	947	943	950
ε	12%	12%	12%	14%	13%

From these tensile tests it can be concluded that the wheel material has higher elongation than the rail material and so a higher capacity of energy absorption before the final fracture. Despite of the similar yield stress of the wheel and rail materials, the rail material has higher ultimate tensile stress.

The monotonic σ *vs.* ε curve of the wheel tensile specimens '*A*' shows a yield *plateau*, a behavior not observed on the other wheel specimens. This could be explained by the fact that this specimen was extracted from a location out of the contact area were the material has not hardened.

The analysis of the failure surfaces of the tested specimens, shown in Figure 3.8 and 3.9, lead to conclude that the wheel material has a ductile behavior and that the rail material has a brittle behavior.

(a) Tensile specimen tested. (b) Failure surface

Figure 3.8: Wheel tensile specimen after testing.

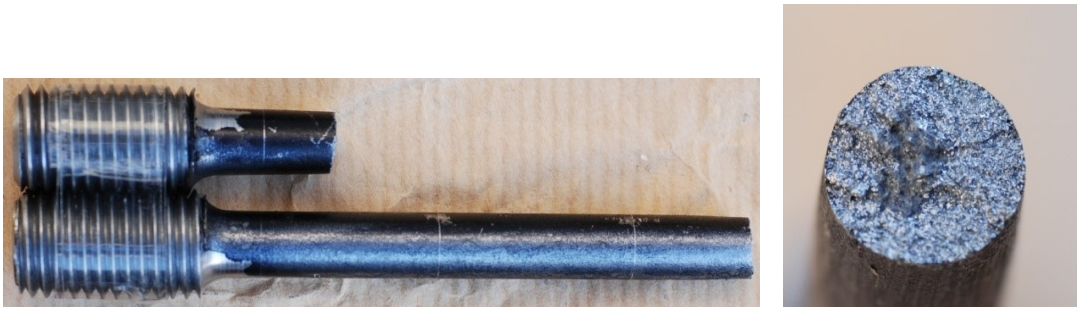

(a) Tensile specimen tested. (b) Failure surface

Figure 3.9: Rail tensile specimen after testing.

3.4 Concluding remarks

A material characterization including chemical composition analysis, mechanical properties determination, microstructure and hardness measurements, was performed on samples taken from an AVE train wheel that reached the geometrical limits for continued usage and from a UIC60 section rail.

If the railway wheel chemical composition and mechanical properties obtained in this study are compared with the values imposed by the EN 13262 standard, we can conclude that the steel that was tested is the ER7/ER8 grade wheel steel, used in high speed trains wheels.

In the case of the obtained chemical composition and mechanical properties for the rail steel, since they are with the values presented in the EN 13674 standard it can be concluded that the R260 MN grade rail steel was studied.

Taking into account the carbon percentage of each of the studied steels ($< 0.8\%$) it was expected that they have a pearlitic, what was verified by the microstructure analysis.

Chapter 4

Twin-disc tests

The current work aims at contributing with experimental results to the evaluation of the wear and the rolling contact fatigue resistance of the wheel-rail contact materials, using a twin-disc machine to simulate the most important dynamic conditions of a real contact.
Dry and lubricated tests were performed in order to obtain an extended characterization of the contact fatigue behavior of these two materials.
The contact surface integrity was analyzed during these tests.
Residual stress measurements at the contact surface and in depth were performed.
A methodology to calculate the mass loss from the variation of the contact surface profile was developed and applied to dry tests.

4.1 State of the art

On a twin-disc machine a disc is loaded against another disc and rotated under closely controlled conditions of load and slip. Twin disc test machines are commonly used to simulate hertzian contacts, like the ones existing in a rolling bearing or, in our case of interest, the wheel/rail contact and predict wheel and rail materials tribological properties, namely surface contact fatigue and wear resistance.
Ringsberg *et al.* in [19] used a twin disc machine to test the laser cladding using Co–Cr alloy to coat the UIC grade 900A (R260) material rail. In this study it was concluded that the residual stresses caused by the surface treatment processes reduced the safety margin against fatigue failure by applying the multiaxial fatigue initiation criterion proposed by Dang Van.
A thermal camera was used by Gallardo-Hernandez *et al.* [20] to measure the temperatures in twin-disc tests of wheel/rail materials. Disc body and contact temperatures were studied for a number of different contact conditions. The obtained results revealed that the temperature in a wheel/rail contact under severe contact conditions, such as high lateral loads and slips that occur when the wheel flange contacts with the rail gauge at railway track curves, may lead to a transition from severe wear to catastrophic wear.

Takikawa and Iriya presented in [21] a study where a twin disc machine was used to investigate the head check, a rolling contact fatigue defect observed on the gauge corner of the high rails on shallow curves.
In [22] Tassini *et al.* compared experimental wear rates of common railway wheel and rail steels obtained from twin disc tests results with results obtained from different numerical models. This study allowed the validation of the different wear algorithms considered.
In the paper [23], numerical algorithms based on the simplified theory of Kalker (FASTSIM software) and capable of modeling variable friction were studied and improved by Rovira *et al.* using experimental friction parameters.
The crack growth behavior on rail surface and it's relation with a variety of parameters was investigated by Jung-Won Seo *et al.* in [24] using twin-disc tests and finite element analysis.
Despite of twin disc machines being commonly used to perform studies on railway wheel and rail materials, they are also used to test other materials, as nylon-glass fiber composites [25], gear materials [26], austempered ductile iron (ADI) [27, 28], molybdenum disulphide/titanium low friction coating for gears [29], polyamide 66 [30], common bearing steel [31] or even the influence of grease composition on rolling contact wear [32].

4.2 Twin-disc machine used

Specimens taken from a AVE train wheel and from a UIC60 section rail were tested in a twin disc machine available at CETRIB-INEGI laboratory of the Faculty of Engineering of the University of Porto, that was recently up-graded [33], shown in Figure 4.1.

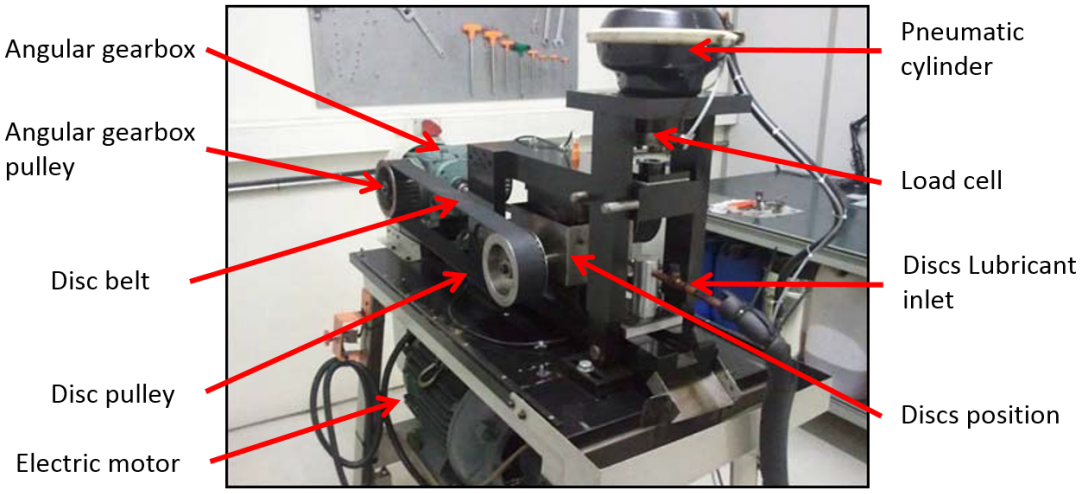

Figure 4.1: Twin disc machine.

Twin disc test machines are commonly used to simulate hertzian contacts, like the ones existing in a rolling bearing or, in our case of interest, the wheel/rail contact and predict wheel and rail materials tribological properties, namely surface contact fatigue and wear resistance.

Before testing any material, the twin-disc machine used was analyzed in depth in order to understand its capabilities. After this analysis it was decided to upgrade the lubricant distribution system and to calibrate the load cell, readjusting the micro-controller installed in the machine.

Twin-disc machine description and capabilities

The twin-disc machine used measures the temperature on the discs contact using an analog pyrometer with a temperature range of 0 to 200 °C. The motor speed is controlled by a speed variator, between 0 and 3000 rpm.
In lubricated tests jet lubrication of the contact and discs shaft supporting bearings is assured by a hydraulic central that guarantees constant lubricant flow and temperature. The return of the lubricant to the tank is assured by an inclination of 3% of the machine supporting table.
The twin-disc machine body, shown in Figure 4.2, is composed by two arms, one fixed (8) were the inferior disc is mounted and an articulated arm (7) which supports the superior disc.

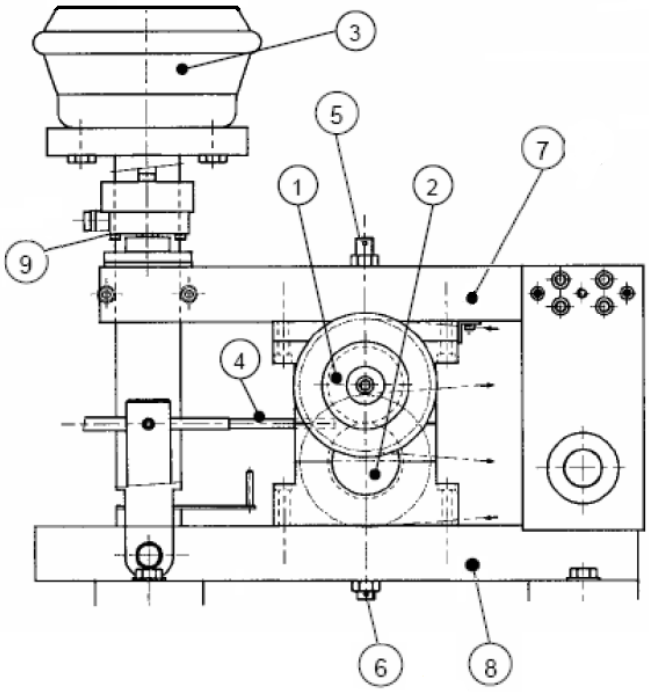

Figure 4.2: Partial view of the twin-disc machine body.

Changes in the discs' diameter, resulting from wear, or the discs' oscillation due to vibration, are measured by two inductive sensors (5) and (6). There is one sensor for each disc. These sensors are intended to be able to detect fatigue damage.
The used twin-disc machine provides a close control of the load, using a 20 kN load cell (9) and a pneumatic cylinder (3). The load can be adjusted using an electronic pressure regulator.

This machine produces plenty of noise and when is performing lubricated tests a cloud of lubricant smoke is produced, so, the machine must be installed in a space (in this case a 3 x 3 m^2 room) with acoustic isolation and forced ventilation.
Therefore, the control unit where all variables are monitored and adjusted, must be installed outside of this room.
The control unit, after being upgraded with a "Disc monitoring system" is capable to read all sensors and compare in real time their readings with predefined set points, and, if these set points are exceeded, a text message is send to the researcher, so that appropriate actions may be taken, and the system stops automatically, recording all data in a period of 10 seconds preceding the alarm. The data collected makes it possible to analyze the situation, and identify what parameter or parameters assumed unexpected values, in order to find the cause of the alarm. This upgrade turned the operation of this machine safer. The motor rotation, the load, the discs surface integrity and temperature and the lubricant flow are the "safe control" variables.
To perform dry tests in the used twin disc machine, it is necessary to change the discs supporting shaft bearings, since the original spherical roller bearings need auxiliary lubrication and are not capable to absorb the thermal expansion of the shafts without causing fails in the system. So when it is intended to perform dry tests these bearings must be changed by single row deep groove ball bearings, auto-lubricated and with the same dimensions of the original spherical roller bearings.

4.3 Experimental work

Preparation of a twin-disc test

Before starting a twin-disc test some attention must dedicated to defining some parameters as:

- the amount of specimens needed to perform all intended tests;
- the specimens geometry within the range of possibilities that can be tested in the machine;
- the specimens material and heat treatment;
- the roughness of the specimens;
- the geometry (transversal radii) of the contact surface of the discs to obtain the intended maximum Hertz pressure in the contact load range of the machine;
- the sliding speed, by choosing the combination of the angular gearbox pulley and the disc pulley,

- the lubricant, by specifying the viscosity at the operating temperature;
- the tangential speed on the contact.

The stock of bearings, security nuts, discs supporting shafts also must be checked, and reinforced if needed, before start any series of tests.

Tested specimens

Two types of discs, one cylindrical and another with a 'spherical' contact surface with 35 mm radius were used. Both types of discs have 70 mm in diameter and 7 mm in thickness, as shown in Figure 4.3[4].

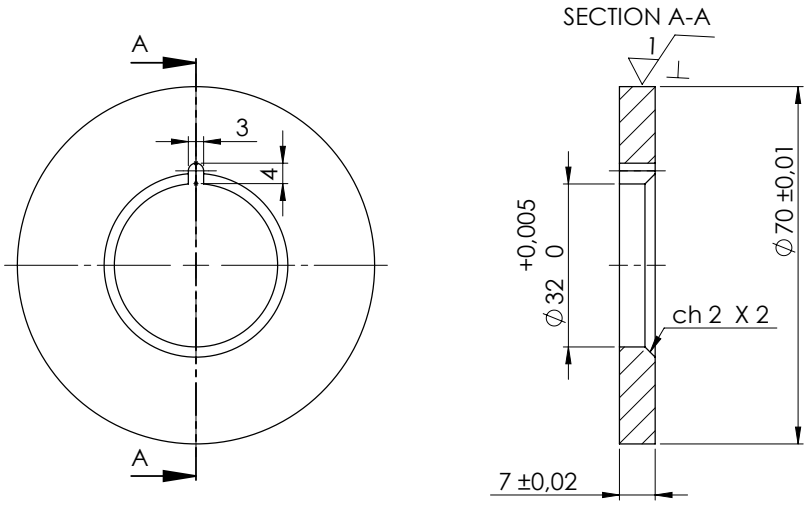

(a) Cylindrical disc.

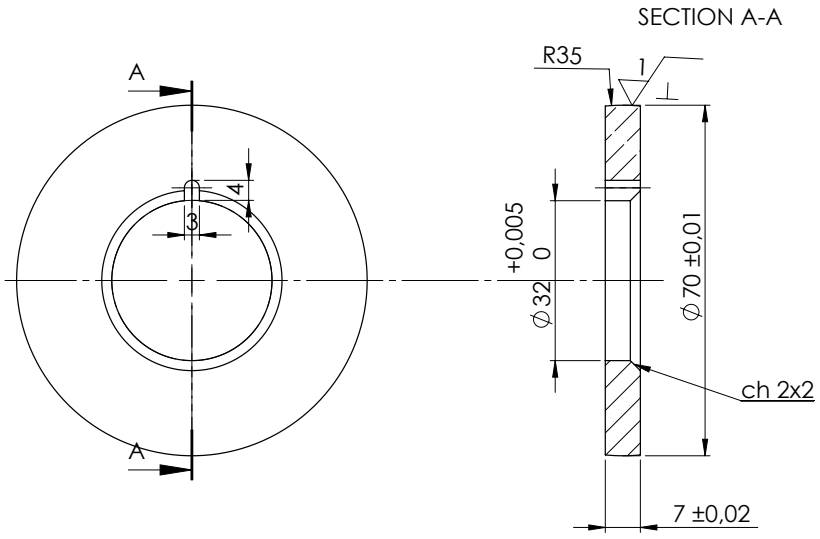

(b) 'Spherical' disc.

Figure 4.3: Disc dimensions.

[4]These specimens were machined at Irmãos SAS, Lda, Porto.

These types of discs were joined in pairs composed of one cylindrical disc and one 'spherical' disc. The 'spherical' discs were taken from a Spanish AVE wheel and the 'cylindrical' ones from a UIC60 rail as shown in Figure 4.4 and Figure 4.5, respectively.

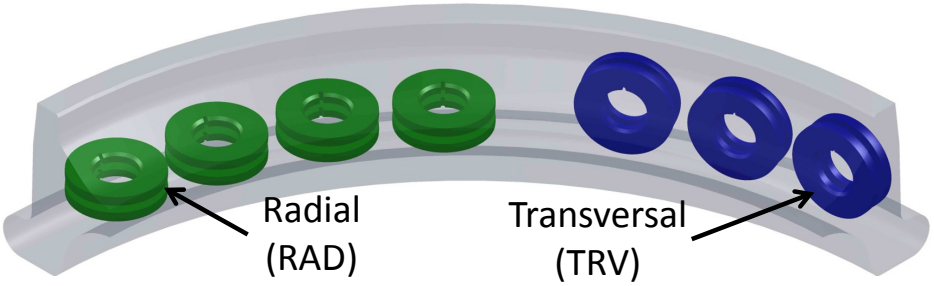

Figure 4.4: AVE wheel discs' location and used name references.

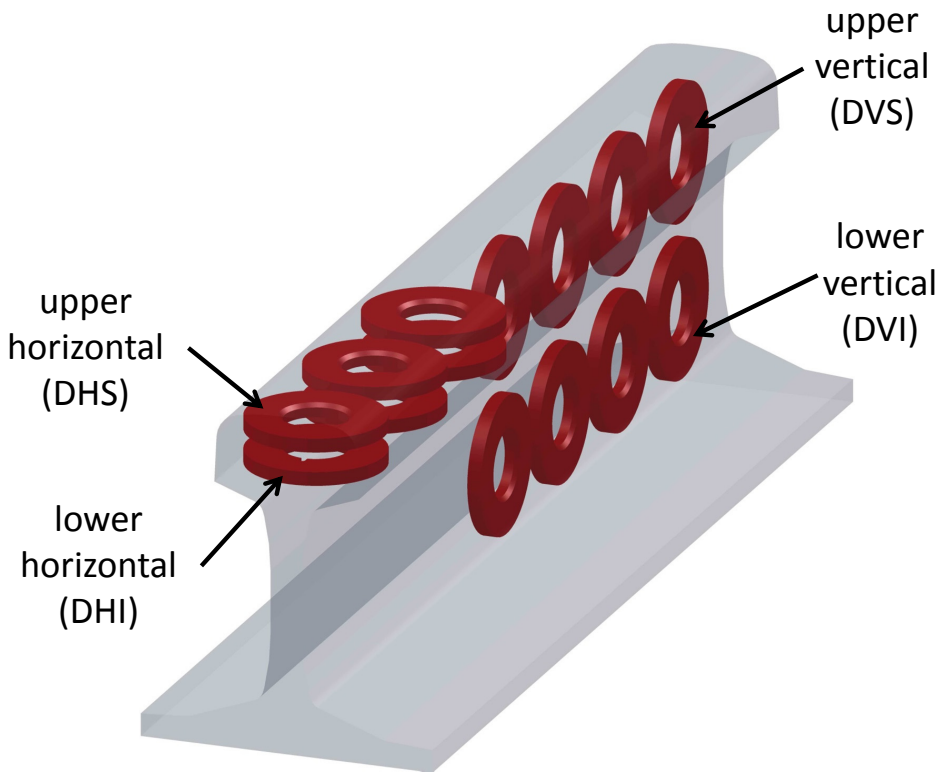

Figure 4.5: UIC60 rail discs' location and used name references.

Since the specimens were extracted from the real wheel and rail profiles it was decided to verify if the specimens' orientation and location has any influence in the RCF behavior by extracting these specimens in different orientations and locations on these two profiles.

Testing conditions

All tests were performed with an applied load of $F = 750$ N. Due to the discs' geometry and according to Hertz theory [34] the maximum contact pressure is $P_0 = 1.4$ GPa, a typical

value found in the wheel/rail contact, and the contact area assumes an elliptical shape with a maximum axis of $a = 0.6$ mm and a minimum axis of $b = 0.4$ mm.
A nominal rotational speed of 3000 rpm was used on the lubricated tests, but due to heat generated in dry tests we were forced to drop the rotational speed to 1000 rpm to obtain a stabilized temperature on the contact of about 30 ºC.
All these testing conditions are resumed on Table 4.1.

Table 4.1: Experimental parameters.

	Lubricated tests	Dry tests
Applied load	750 N	750 N
Maximum hertz pressure	$P_0 = 1.4$ GPa	$P_0 = 1.4$ GPa
Contact area dimensions	$a = 0.6$ mm $b = 0.4$ mm	$a = 0.6$ mm $b = 0.4$ mm
Testing speed	3000 rpm	1000 rpm
Contact temperature	40 - 50 ºC	30 ºC
Lubricant	Galp TM100	-

Table 4.2 shows the wheel and rail discs combinations tested on the lubricated and dry tests.

Table 4.2: Tested pairs

pair #	wheel disc ref.	rail disc ref.	lubricant
V	TRV1	DHS1	Galp TM100
VI	RAD3	DVI1	Galp TM100
VIII	RAD2	DHI1	-
IX	TRV5	DHI3	-

Galp TM100 oil was used as a lubricant as it is a mineral oil with no special additives, and reduces the wear, reducing its influence on the RCF and promoting the appearance of contact fatigue defects – which are the object of this study. Lubricant properties are shown in Table 4.3.

Table 4.3: Galp TM 100 properties.

Viscosity at 40°C [cSt]	Viscosity at 100°C [cSt]	Density [kg/m^3]	Viscosity index
100.8	10.9	891	95

During lubricated tests the lubricant was heated and injected in the contact between 40 ºC and 50 ºC.
In order to be possible to perform dry tests, as said before, the bearings of the discs supporting shaft were changed.

In this case the original spherical roller bearings with the reference SKF 22206 E were changed by single row deep groove ball bearings with the reference SKF 62206-2RS1. The technical drawings of these bearings are shown in Figure 4.6.

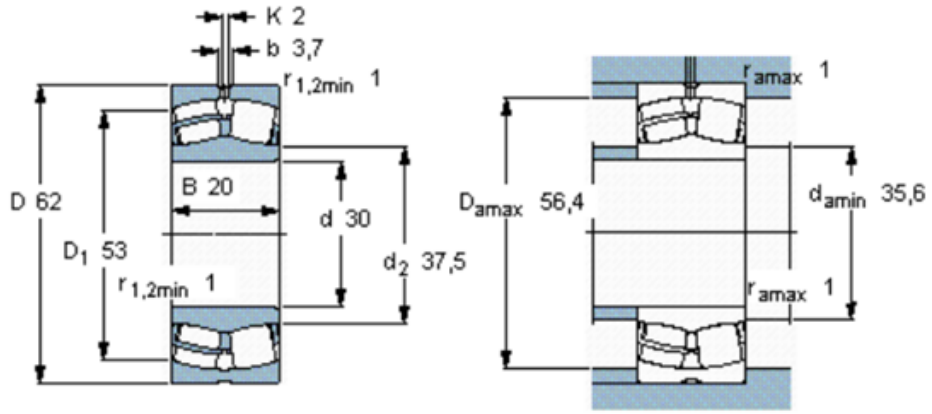

(a) SKF 22206 E bearing.

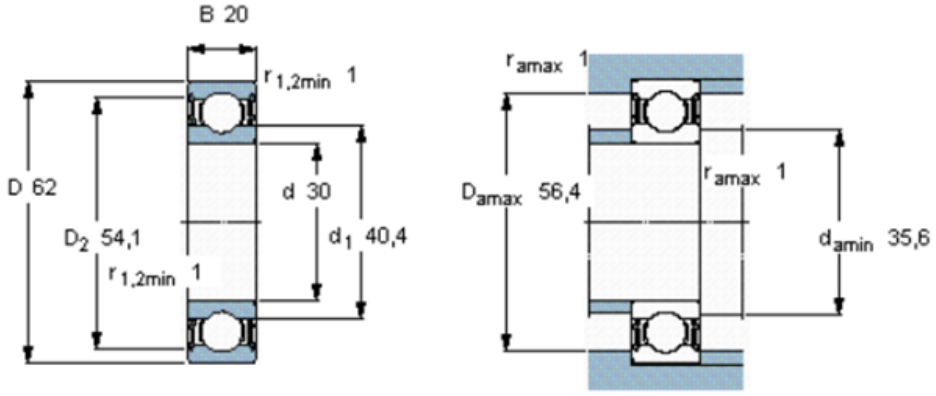

(b) SKF 62206-2RS1 bearing

Figure 4.6: Used bearings, technical drawings.

Specimens integrity inspections

Some interruptions of the twin disc tests were made for measuring the contact surface roughness and topography, the mass loss (due to wear) with the objective to follow their evolution during the rolling contact fatigue process.

The roughness and topography measurements were performed on a HOMMELWERKE T8000 measuring station equipped with a drive unit LV-50/50 E and a TKL 300 measuring probe, at CETRIB-INEGI.

Four roughness measurements of the contact band separated by 90º on the perimeter of the discs were made at every test stop and the control of the roughness evolution was made by following the average value of the roughness average (Ra) and the RMS roughness average (Rq) of these four points.

A topography registry with 5 mm of width and 1.5 mm of length was also made in every tested specimen at every stop and the control variables were the arithmetical mean height of

the surface (Sa) and RMS height of the surface (Sq). These variables were compared with Ra and Rq in order to verify if the measured topography is representative of the all disc contact surface.

The discs mass was measured using weighing-machine METTLER TOLEDO, model PR1203 with a maximum capacity of 1210 g and a resolution of 0.001 g. Three measurements were made of each discs at every stop and the considered mass is the average value of this three measurements.

The contact surfaces of the tested specimens were also observed by optic microscopy during twin disc tests interruptions to verify the existence of defects.

Residual stress measurements

Residual stress determination was performed by X-ray diffraction using the sin2ψ method [35, 36, 37]. The experiments were carried out with a PROTO iXRD equipment, shown in Figure 4.7a, available at CEMDRX-FCTUC, working on Ω mounting. Lattice deformations of the {211} diffraction planes ($2\theta \approx 156°$) were measured using Cr-Kα X-ray radiation, with 11 β angles (22 ψ angles), an acquisition time of 30 seconds by peak and ±2° oscillation in ψ. The stress was evaluated using the value of 5.83×10^{-6} MPa^{-1} for the (1/2) S2 X-ray elastic constant. For the material analyzed and considering the radiation used, the average penetration depth of the X-rays was about 5 μm.

The residual stresses were determined in the longitudinal and transversal directions of the rolling track, on a rectangular area with a maximum width between 0.7 and 0.9 mm, at the center of the rolling track, as shown in Figure 4.7b.

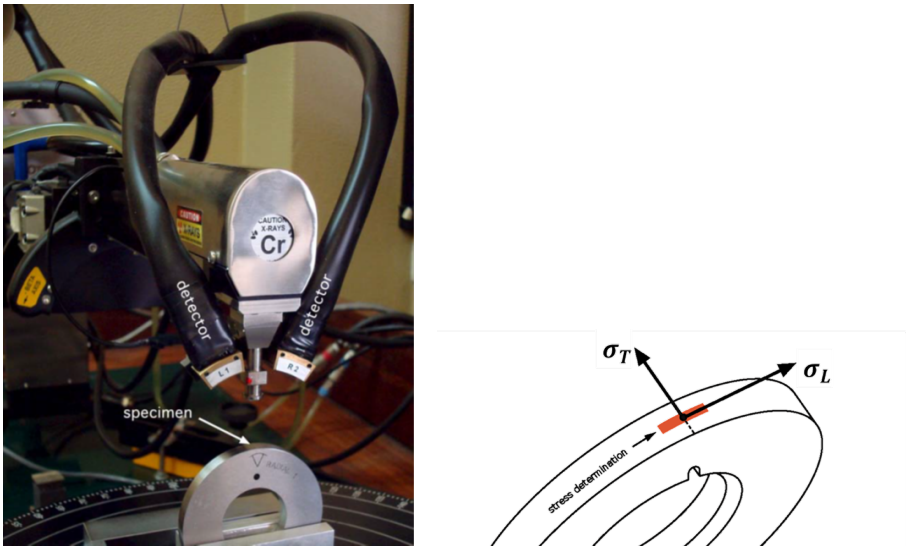

(a) Experimental apparatus

(b) Area and directions of residual stress measurements.

Figure 4.7: Residual stress measurements apparatus.

In Figure 4.8 the discs residual stresses evolution in depth before testing is shown. To obtain these profiles a mechanical polish technique was used to remove the material layers.

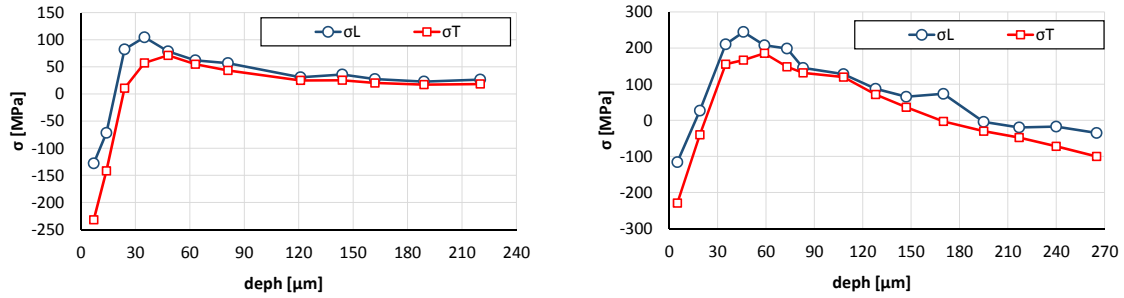

(a) Disc RAD1 residual stress evolution in depth.

(b) Disc DVS1 residual stress evolution in depth.

Figure 4.8: Discs residual stresses evolution in depth before testing.

4.4 Twin disc contact finite element model

A numerical model based on discs geometry was built with the software Abaqus - a commercial finite element program - in order to obtain the stress distribution in the contact.
To build this model 188160 C3D8R elements, with 205130 nodes, were used. The Lagrange multipliers were used to simulate the contact. The considered material behavior is linear-elastic, with a Young's modulus of 207 GPa and Poisson's ratio of 0.3. Due to specimens symmetry only a half was considered and special attention was dedicated to the mesh refinement on the contact zone, as can be seen in Figure 4.9 .
The applied normal force was 750 N.

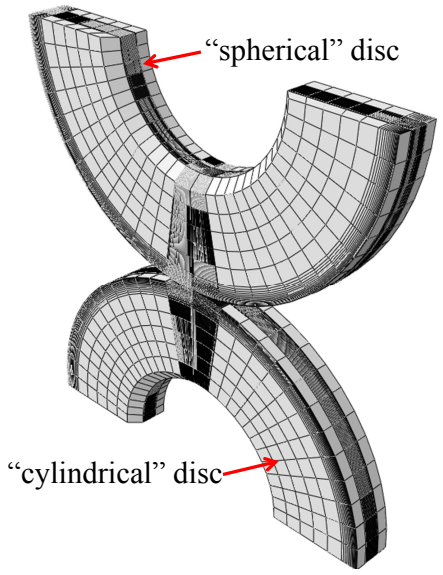

Figure 4.9: Twin disc finite element mesh

The obtained equivalent von Mises stress distribution is shown in Figure 4.10, which is quite similar on both discs.

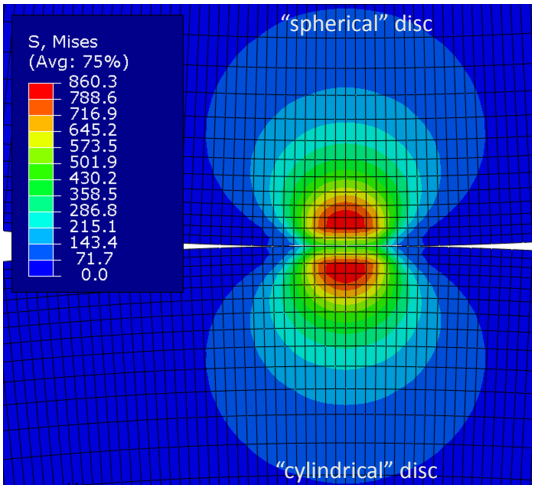

Figure 4.10: Equivalent von Mises stress distribution.

The contact pressure at the contact surface distribution for both discs is shown in Figure 4.11, where it can be observed that the maximum contact pressure is approximately 1.4 GPa as obtained with the Hertz theory. This Figure also revealed that the smallest radius is oriented in the rolling direction.

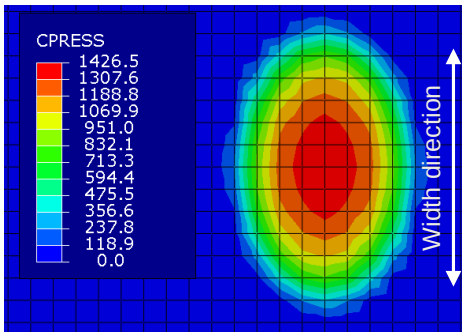

(a) "Cylindrical" disc surface contact pressure field.

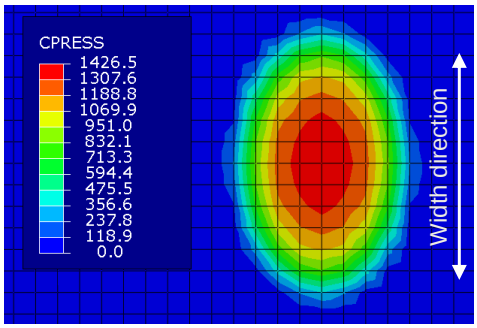

(b) "Spherical" disc surface contact pressure field

Figure 4.11: Contact pressure field at the discs contact surface.

4.5 Lubricated tests results

The mass evolution of the discs tested in lubricated conditions is shown in Figure 4.12 and Figure 4.13. The contact surface roughness parameters Ra, Rq, Sa and Sq evolution in lubricated tests are shown in Figure 4.14 and in Figure 4.15.

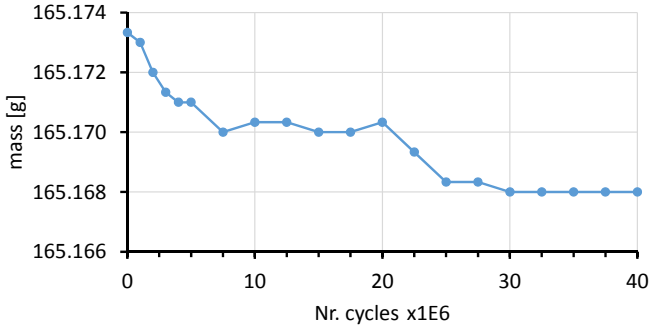

(a) Disc TRV1 mass evolution.

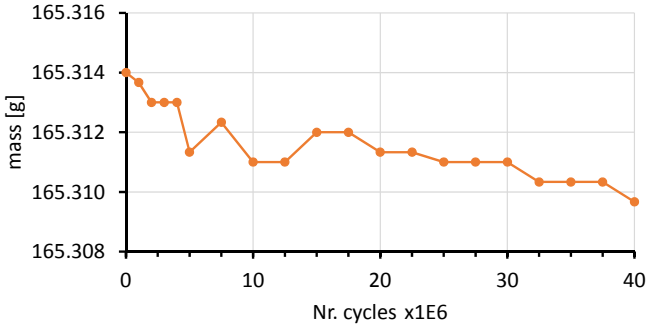

(b) Disc DHS1 mass evolution.

Figure 4.12: Discs pair V mass evolution during lubricated tests

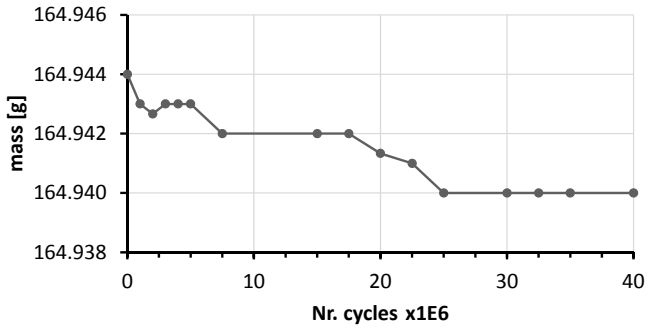

(a) Disc RAD3 mass evolution.

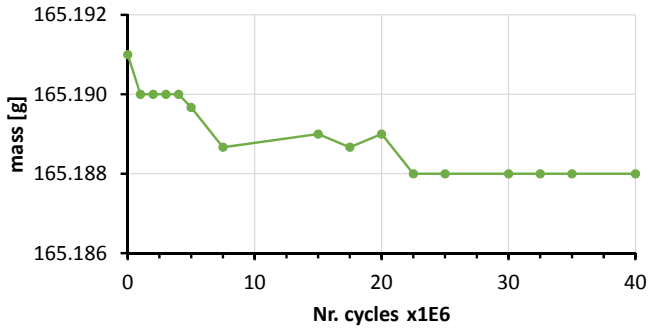

(b) Disc DVI1 mass evolution.

Figure 4.13: Discs pair VI mass evolution during lubricated tests

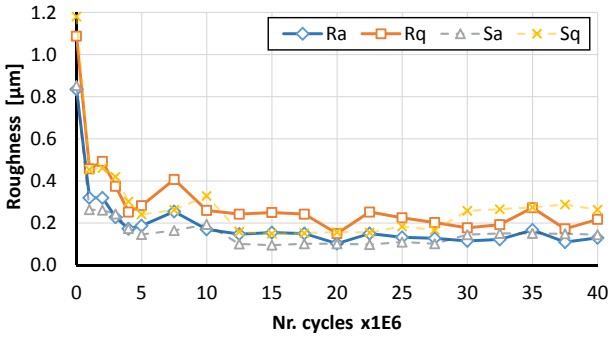

(a) Disc TRV1 roughness parameters evolution.

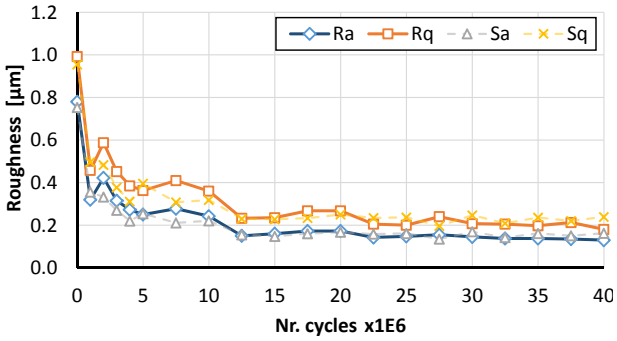

(b) Disc DHS1 roughness parameters evolution.

Figure 4.14: Discs pair V roughness parameters evolution during lubricated tests.

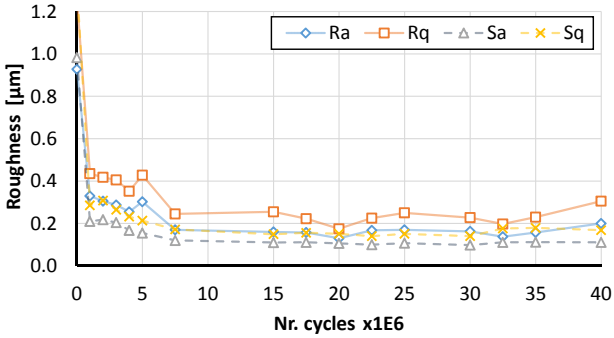

(a) Disc RAD3 roughness parameters evolution.

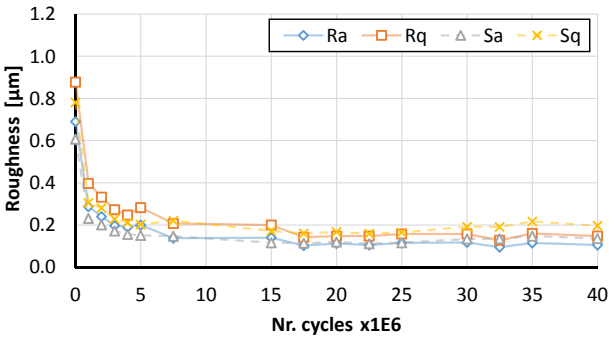

(b) Disc DVI1 roughness parameters evolution.

Figure 4.15: Discs pair VI roughness parameters evolution during lubricated tests.

Figure 4.16 shows some topography measurements taken of the discs pair V during lubricated tests, and Figure 4.17 shows similar results for discs pair VI.

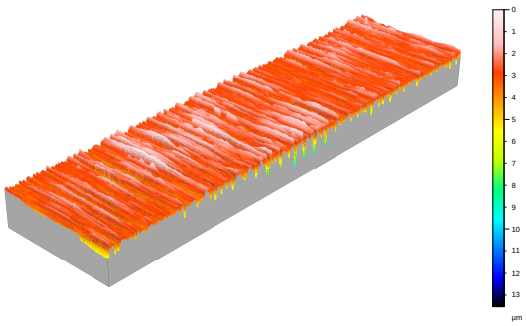

(a) Disc TRV1 topography before testing.

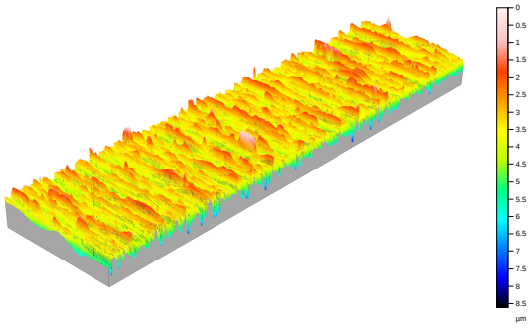

(b) Disc DHS1 topography before testing.

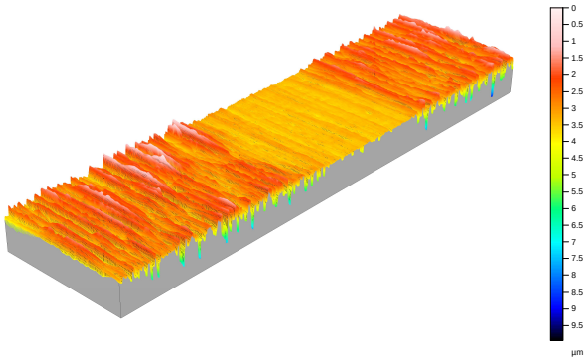

(c) Disc TRV1 topography after 5×10^6 cycles.

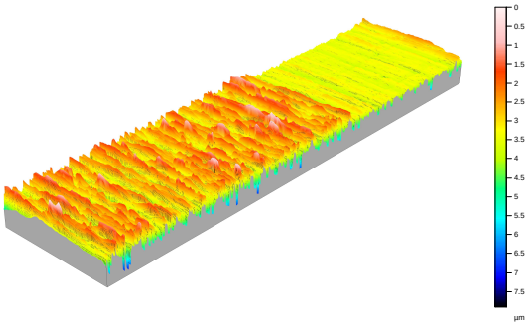

(d) Disc DHS1 topography after 5×10^6 cycles.

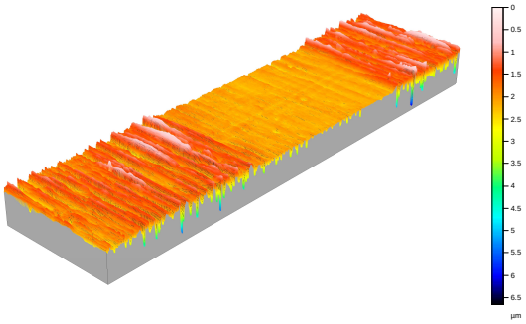

(e) Disc TRV1 topography after 40×10^6 cycles.

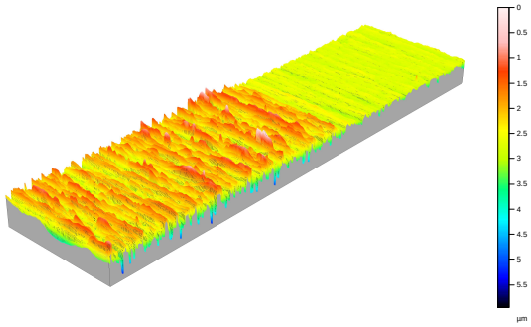

(f) Disc DHS1 topography after 40×10^6 cycles.

Figure 4.16: Pair V discs topography evolution during lubricated tests.

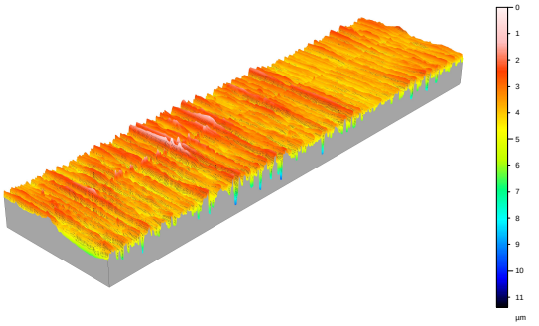

(a) Disc RAD3 topography before testing.

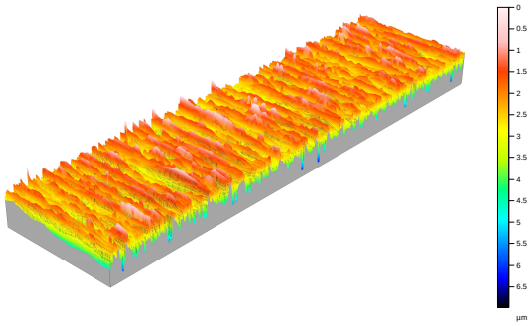

(b) Disc DVI1 topography before testing.

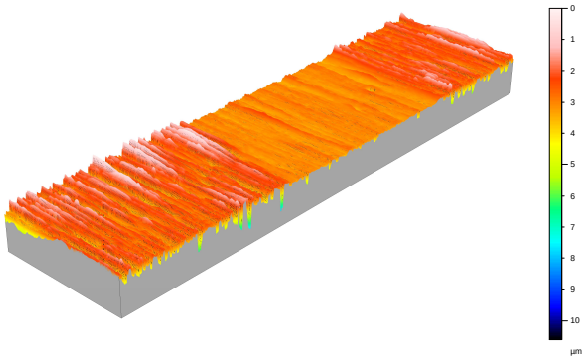

(c) Disc RAD3 topography after 5×10^6 cycles.

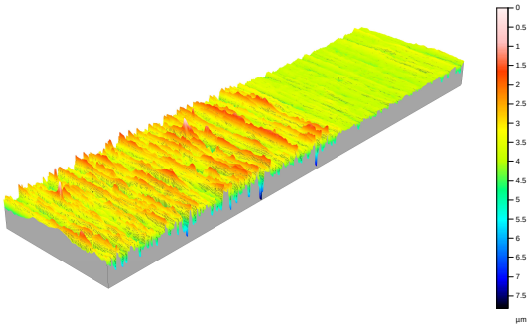

(d) Disc DVI1 topography after 5×10^6 cycles.

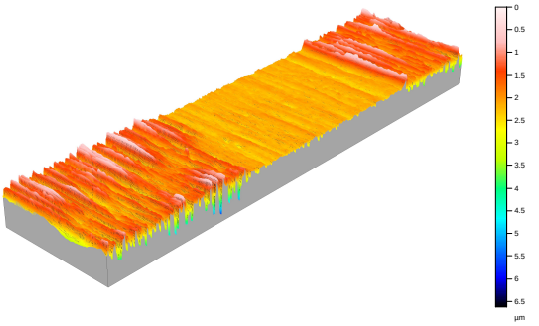

(e) Disc RAD3 topography after 40×10^6 cycles.

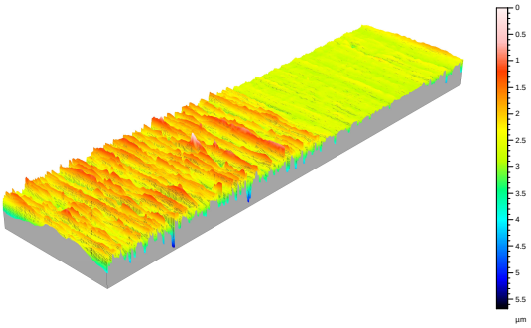

(f) Disc DVI1 topography after 40×10^6 cycles.

Figure 4.17: Pair VI discs topography evolution during lubricated tests.

Figure 4.18 shows some defects detected during lubricated tests.

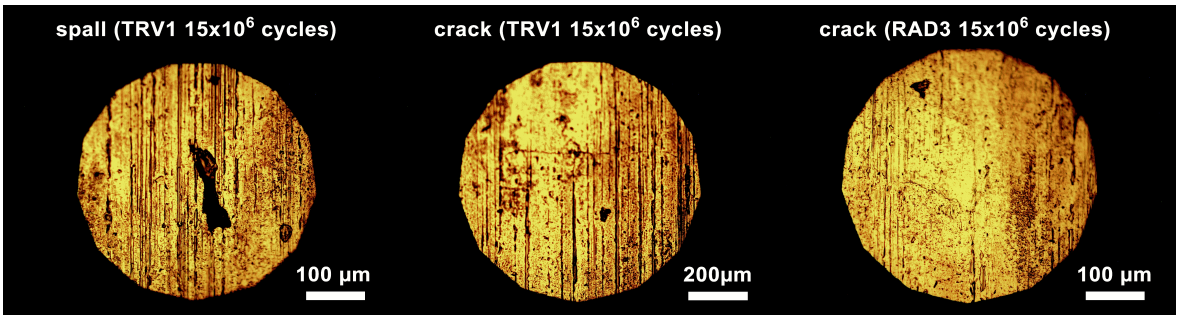

Figure 4.18: Some contact fatigue surface defects detected at lubricated tests.

As an example of the state of the discs contact surfaces after tested in lubricated conditions, Figure 4.19 shows a picture of the discs pair VI contact surface after testing.

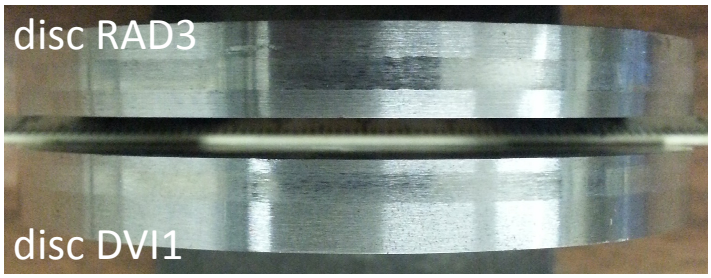

Figure 4.19: Contact surfaces after 40×10^6 cycles in lubricated conditions.

The evolution of the residual stresses at the discs' surface, during rolling contact fatigue of the discs pair V are shown in Figure 4.20 and in Figure 4.21for discs pair VI.

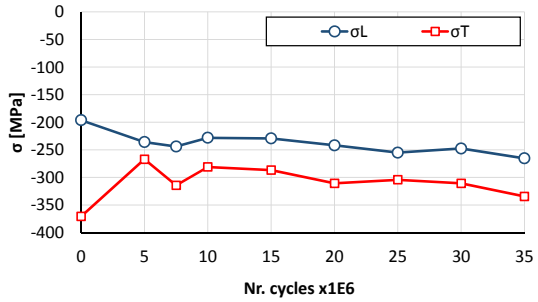

(a) Disc TRV1 residual stress evolution.

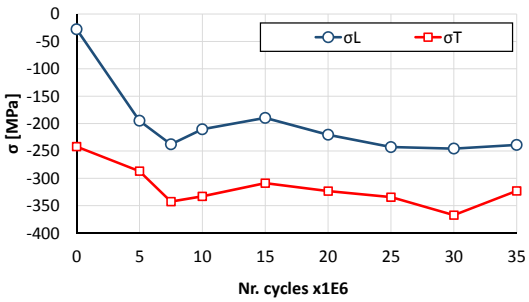

(b) Disc DHS1 residual stress evolution.

Figure 4.20: Residual stresses evolution at the discs' pair V surface

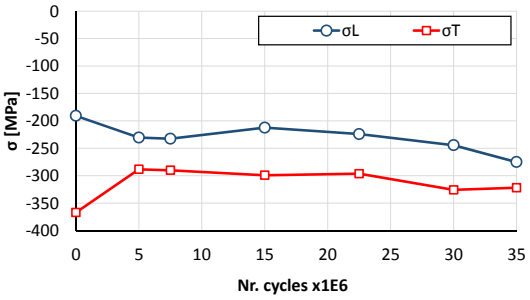

(a) Disc RAD3 residual stress evolution.

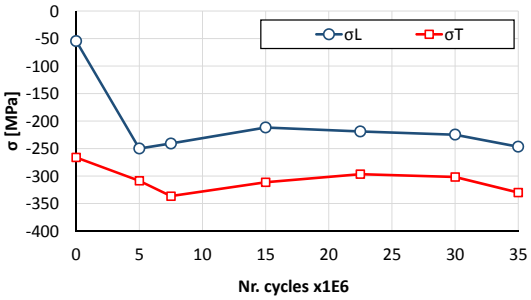

(b) Disc DVI1 residual stress evolution.

Figure 4.21: Residual stresses evolution at the discs' pair VI surface

These results show that before rolling contact fatigue tests, the specimens present an initial residual stress state in the surface layers essentially due to the machining and finishing of the specimens surface, since they were not submitted to any post-machining treatment. The specimens present compressive stresses near the surface, more intense in the transversal

direction. The initial stress state at the surface, however, is not the same on the discs obtained from the wheel and the rail due to the fact that the sequence of machining and finishing operations were not the same for the two types of specimens. Gradual changes of the residual stress state, mainly during the running-in phase are also observed. The surface residual stresses are always compressive for both types of discs and more intense in the transversal direction, compared to longitudinal. But the "stabilized stresses" are very similar for the same direction in both types of discs, even if they were very different before tests.
The residual stress profiles in depth after 40 millions of rolling contact fatigue cycles, under a maximum contact pressure of 1.4 GPa and in lubricated conditions can be observed in Figure 4.22.

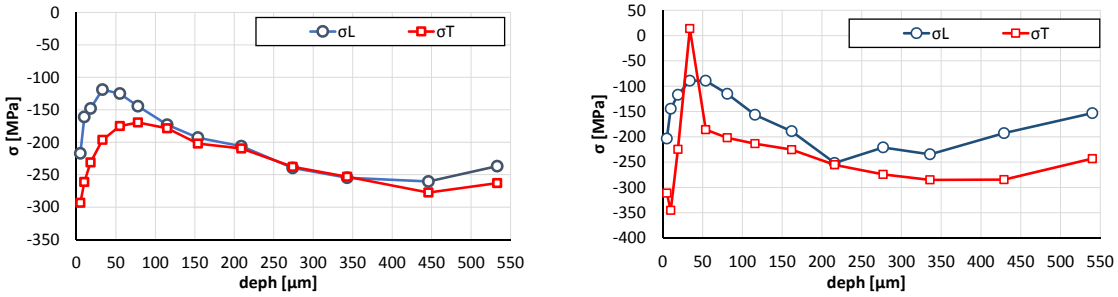

(a) Disc TRV1 residual stress evolution in depth.

(b) Disc DHS1 residual stress evolution in depth.

Figure 4.22: Disc's tested in lubricated conditions residual stress in depth after 40 millions of rolling contact fatigue cycles.

4.6 Dry tests results

The mass evolution of the discs tested in dry conditions is shown in Figure 4.23 and in Figure 4.24. The contact surface roughness parameters Ra, Rq, Sa and Sq evolution in dry tests are shown in Figure 4.25 and in Figure 4.26.

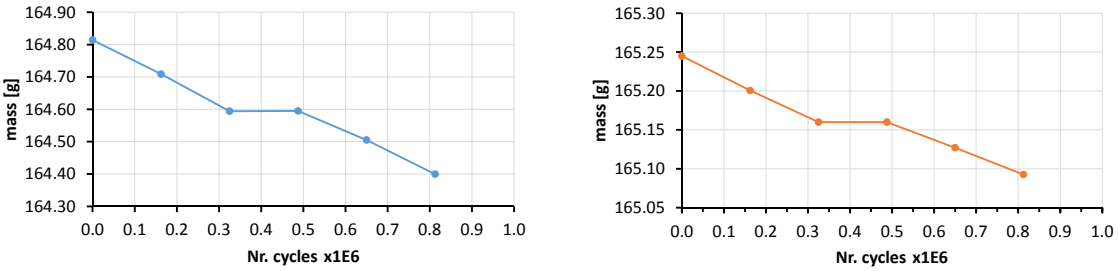

(a) Disc RAD2 mass evolution.

(b) Disc DHI1 mass evolution.

Figure 4.23: Discs pair VIII mass evolution during dry tests

Figure 4.23 shows no mass loss between 0.3 and 0.5 millions of cycles in the wheel and rail discs of the pair VIII; a phenomenon that could be explained by some error in the mechanism

that applies the load. Since the load cell is installed between the pneumatic cylinder and the supporting arm of the superior disc, and the self-weight of this arm is compensated by the tension on the belt, during the test the tension on the belt could increase making the control system read a load that's higher than the one applied on the discs.

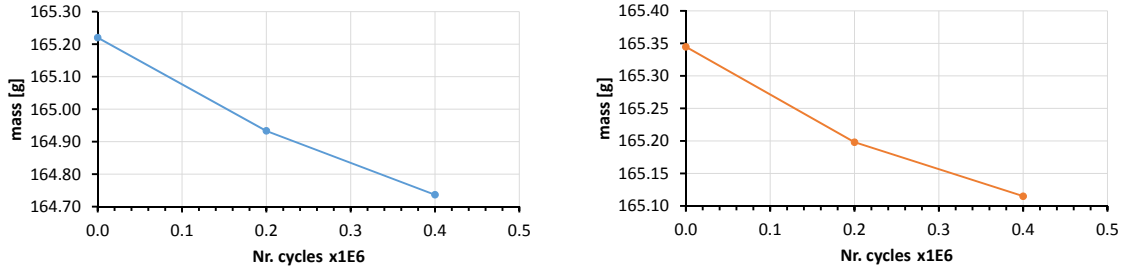

(a) Disc TRV4 mass evolution.

(b) Disc DHI3 mass evolution.

Figure 4.24: Discs pair IX mass evolution during dry tests

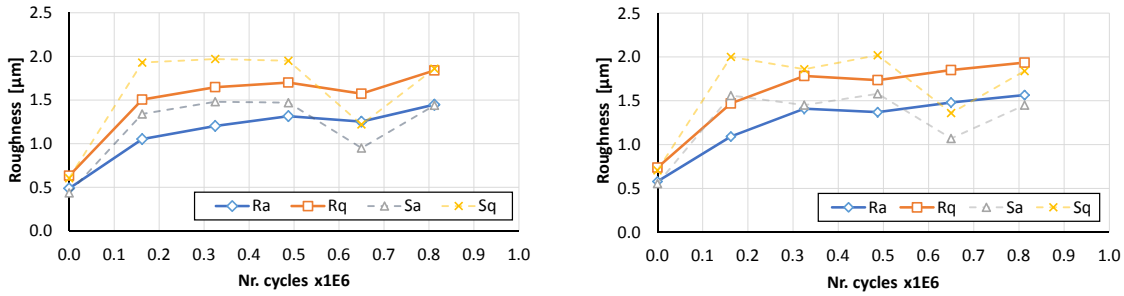

(a) Disc RAD2 roughness parameters evolution..

(b) Disc DHI1roughness parameters evolution..

Figure 4.25: Discs pair VIII roughness parameters evolution during dry tests.

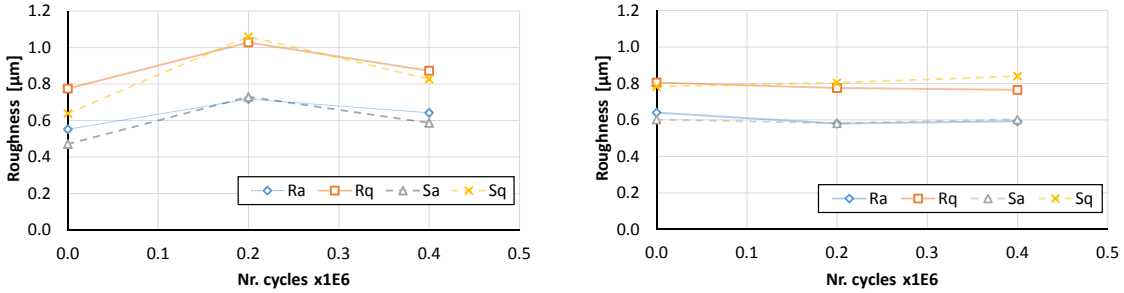

(a) Disc TRV4 roughness parameters evolution.

(b) Disc DHI3 roughness parameters evolution.

Figure 4.26: Discs pair IX roughness parameters evolution during dry tests.

Figure 4.27 shows some topography measurements taken of the discs pair VIII during dry tests, and Figure 4.28 shows similar results for discs pair IX.

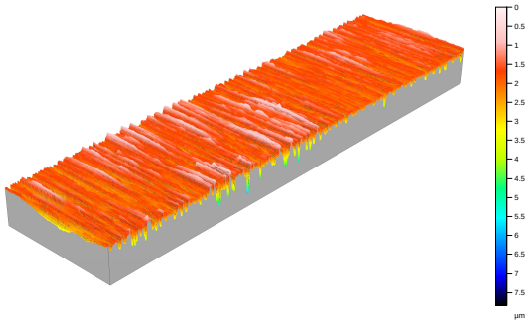

(a) Disc RAD2 topography before testing.

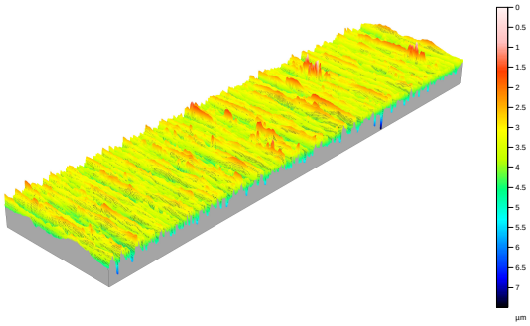

(b) Disc DHI1 topography before testing.

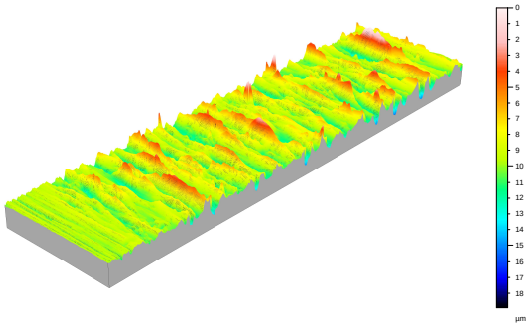

(c) Disc RAD2 topography after 0.6×10^6 cycles.

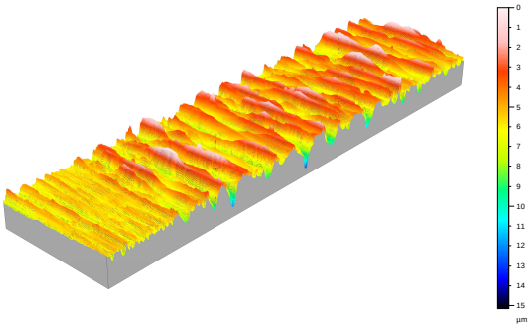

(d) Disc DHI1 topography after 0.6×10^6 cycles.

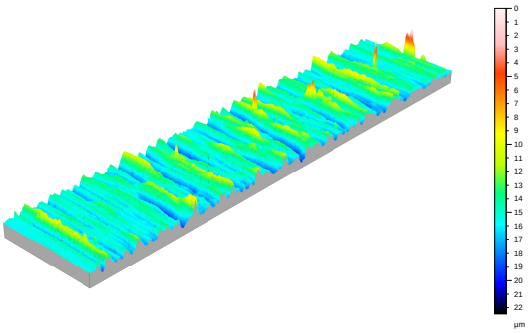

(e) Disc RAD2 topography after 1×10^6 cycles.

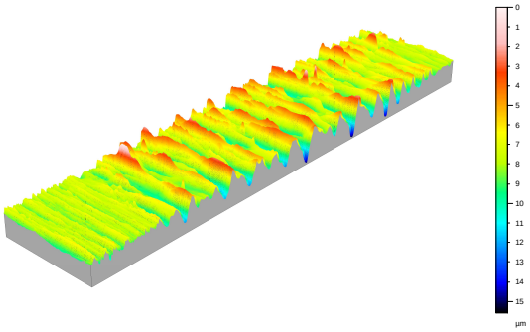

(f) Disc DHI1 topography after 1×10^6 cycles.

Figure 4.27: Pair VIII discs topography evolution during dry tests.

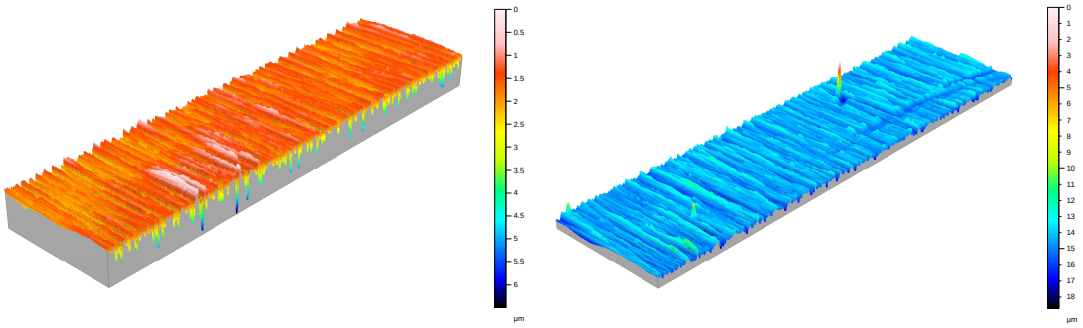

(a) Disc TRV4 topography before testing.

(b) Disc DHI3 topography before testing.

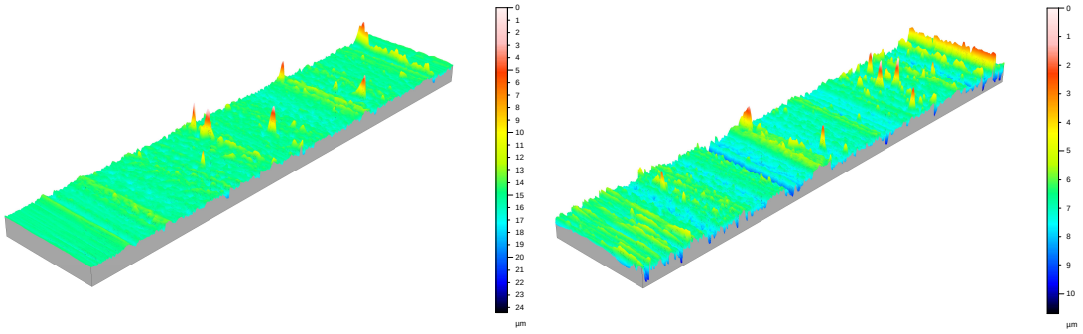

(c) Disc TRV4 topography after 0.2×10^6 cycles.

(d) Disc DHI3 topography after 0.2×10^6 cycles.

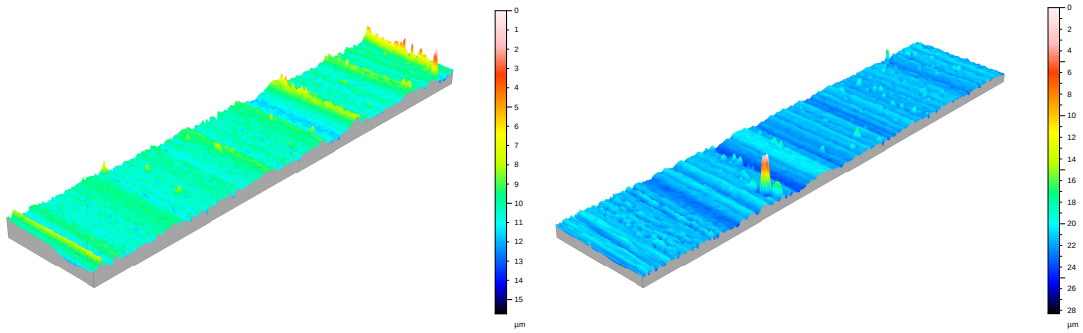

(e) Disc TRV4 topography after 0.4×10^6 cycles.

(f) Disc DHI3 topography after 0.4×10^6 cycles.

Figure 4.28: Pair IX discs topography evolution during dry tests.

As an example of the state of the discs contact surfaces after tested in dry conditions, Figure 4.29 shows a picture of the discs pair VIII contact surface after testing.

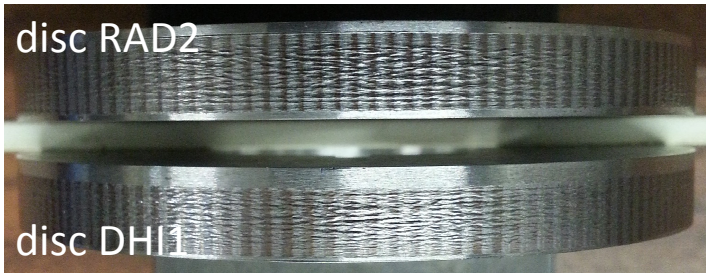

Figure 4.29: Contact surfaces after 0.8×10^6 cycles in dry conditions.

4.7 Calculation of wear from the topography

A methodology to calculate the mass loss from the variation of the contact surface profile was applied to the dry tests and the results are shown below. It was decided to apply this methodology to dry tests only, since they had the highest discs profile variation which renders more clear the difference between roughness measured profiles.
This methodology starts with the alignment of the roughness profiles taken in different stops of the tests, as shown in Figure 4.30 and in Figure 4.31 for the "spherical" disc and for the "cylindrical" disc respectively. Then the material lost volume is calculated by integration. Considering the lost volume and a material density of 7860 kg/m^3, the mass lost is calculated. The calculated mass loss results were compared with the measured ones and a good agreement was found, as shown in Table 4.4 and Table 4.5.
The presented results were calculated taking into account the measurements performed on discs pair VIII composed by the disc RAD2 taken from the wheel and by the disc DHI1 taken form the rail.

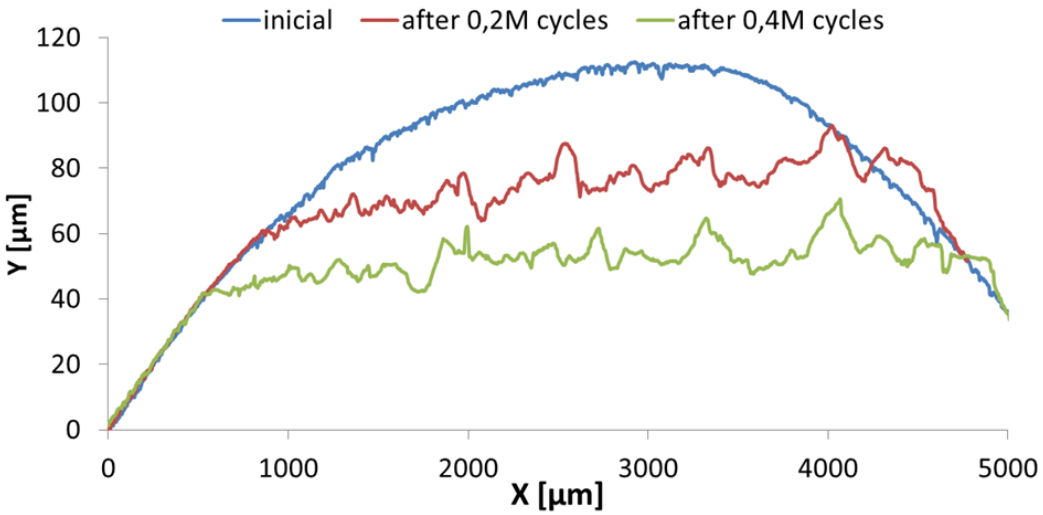

Figure 4.30: "Spherical" disc roughness profiles alignment.

Table 4.4: Mass loss on "spherical" disc.

Nr. cycles	Calculated [g]	Measured [g]
0.2×10^6	0.113	0.105
0.4×10^6	0.255	0.220

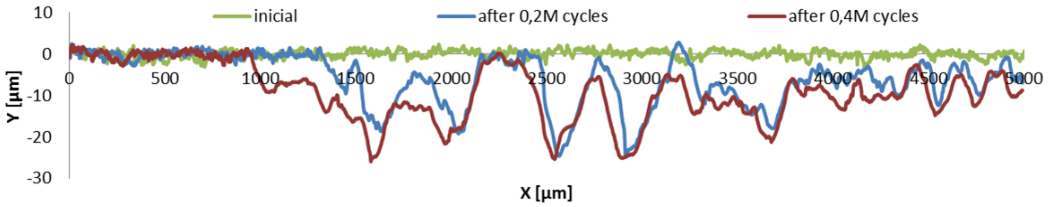

Figure 4.31: “Cylindrical” disc roughness profiles alignment.

Table 4.5: Mass loss on “cylindrical” disc.

Nr. cycles	Calculated [g]	Measured [g]
0.2×10^6	0.044	0.044
0.4×10^6	0.084	0.085

4.8 Concluding remarks

The twin disc rolling contact fatigue tests performed in wheel and rail materials allowed to conclude that under the tested conditions the running-in phase of the studied materials ends after approximately 5 million rotations, and rolling contact fatigue cracks appear at the contact surface after 15 to 18 million cycles in lubricated conditions.

It was verified, during lubricated tests, that the wheel material is more sensitive to defect initiation, since the larger number of defects was observed in the wheel specimens.

However, during dry tests no defect was detected, probably due to the high wear rate that removes any crack that appears at the contact surface.

The wheel material presents a higher wear rate than the rail material, which is more noticeable in dry tests. This difference in the wear rate is the cause of the corrugations observed in the contact surfaces of the discs tested in dry conditions, due to the fact that the used twin-disc machine imposes the same rotating speed in the two discs and if one has higher wear it’s diameter will be different than the other disc, consequently the tangential speed of the two discs on the contact will be different and sliding is verified.

Since the wheel material that composes the “spherical” discs is more soft than the rail material of the “cylindrical” discs, and has a higher wear rate, it’s curvature will decrease along the test and the contact pressure will decrease also, this phenomenon can be the explanation for the reduction of the wear rate between stops of dry tests, evidenced by the change in the slop of the lines of Figure 4.24 between stops.

No significant influence of the extraction position was detected on the results.

A methodology to calculate the mass loss from the variation of the roughness profile was developed and good agreement was found with mass measurements.

Chapter 5

Fatigue crack growth behavior

Fatigue crack growth rate (FCGR) measurement tests according to the ASTM E647 standard were performed in specimens taken from a Spanish high speed AVE train wheel and from a UIC60 rail. Three different load ratios were used in order to obtain an extended range of crack propagation for different types of loading observed in real operation. Two different approaches were used to determine the fatigue crack growth threshold of these two materials: *i)* the *K*-decreasing test procedure described in the ASTM E647 and *ii)* the constant K_{max} with increasing K_{min} method. The adopted experimental methodologies for obtaining results in the Paris law and near threshold regimes will be presented and discussed. Since the fatigue crack growth rate problem is widely discussed in the literature, which also includes some studies in wheel and rail steels, these will be used for comparison and for the discussion of the new results presented.

5.1 Introduction and literature review

Fatigue crack growth rate behavior tests according to the ASTM E647 standard [38] were performed from the non-propagation, near-threshold regime, up to limits related to the extent of plasticity ahead of the crack tip on steels of railway wheels and rails in order to characterize the stable crack propagation under cyclic loading over a wide range $\triangle K$ values.
The obtained data aims at contributing for the development of accurate fatigue models for the wheel/rail fatigue problems. The understanding of fatigue crack propagation originated in rolling contact fatigue will contribute for more efficient maintenance and safety procedures.
Fatigue crack growth rate tests involve cyclic loading of notched specimens which have been pre-cracked in fatigue. During these experimental tests the crack length (a) is recorded as a function of the number of cycles (N), together with the maximum and minimum values of the applied load. Using the recorded data and an appropriated methodology it is possible to obtain the fatigue crack growth rates (da/dN) and the corresponding values of the crack-tip stress-intensity factor range ($\triangle K$).

The obtained results can be represented as $da/dN = f(\triangle K)$ plots which provide results independent from the geometry. This enables comparison of obtained results from a variety of specimen configurations and loading conditions assuming the similitude concept which implies that cracks of different lengths subjected to the same nominal $\triangle K$ value will grow by equal increments of crack extension per cycle [38].

Several studies of fatigue crack growth rates in wheel and rail steels are published in the technical literature. Among these, El-Shabasy and Lewandowski presents in [39] the effect of changes in load ratio, R , and test temperature on the fatigue crack growth behavior of fully pearlitic eutectoid steel. This study revealed a significant effect of load ratio on the Paris law slope for a given test temperature and an increase in $\triangle K_{th}$ as the test temperature decreases.

The effect of rail residual stress in fatigue crack growth rates was studied by Skyttebol *et al.* and presented in [40]. The authors reported that due to the high tensile stresses in the lower part of the rail head a very high stress ratio is observed, $0.7 \leq R \leq 0.9$, implying that existing cracks are fully open during the load passage.

The fatigue crack growth behavior of a premium rail steel was studied using the Modified Crack Layer (MCL) theory by Aglan and Gan [41]. In that work, the fatigue test specimens were sliced longitudinally from the head of a new rail near the web which represents the microstructure of the base material, avoiding the vertical microstructure gradient inside the rail.

Bulloch presents in [42] a study of fatigue crack growth in welded rail steels concluding that the deformed rail steel exhibited fatigue crack growth rates that are slightly faster than undeformed rail steel and weld metal growth data are appreciably faster than rail steel growth results.

Zain *et al.* [43], tested compact tension specimens (C(T)) made from rail steel with a load ratio of 0.1 while simultaneously recorded the acoustic emission signal in order to obtain the acoustic emission count rate associated with the stress intensity factor.

Baseline fatigue crack growth data at $R = 0$ of different rail materials which were in service on U.S. in 1978 have been generated by Feddersen *et al.* [44] in order to develop a correlation of mechanical and metallurgical factors affecting crack behavior in rail steels.

Further to the more common determination of Paris law constants it is important to characterize the near-threshold regime and determine the fatigue crack growth threshold, because for crack propagation in actual service the initial values of $\triangle K$ are expected to be rather low. Typically cracks will initiate at the near-surface area or at the surface as a result of some local damage.

It is considered that the fatigue crack growth threshold is the asymptotic value of $\triangle K$ at which da/dN approaches zero, or according to the ASTM E647 standard $da/dN < 10^{-10}$ m/cycle, and if the stress intensity factor for a given crack is below the threshold value, the crack is assumed to be nonpropagating.

At near-threshold levels, several factors, such as microstructure, environment, loading condition, and crack size, significantly affect crack propagation rates [45].
The fatigue crack growth threshold is experimentally defined using ASTM standard E647, where a load reduction methodology is applied. Using this technique it is observed that $\triangle K_{th}$, decreases as the (positive) load ratio is increased.
Crack closure is generally considered to be the principal reason for the effect of load ratio on the $\triangle K_{th}$ fatigue threshold value in metallic materials [46].
This could be explained by the fact that the methodology described in the ASTM E647 standard uses a load reduction technique where the maximum and minimum load are reduced, and, when the threshold is being reached, during the unloading process the crack will close first at some point along the wake or blunt at the crack tip, reducing the load effect at the crack tip [47]. This phenomenon is schematized on Figure 5.1, adapted from [48].

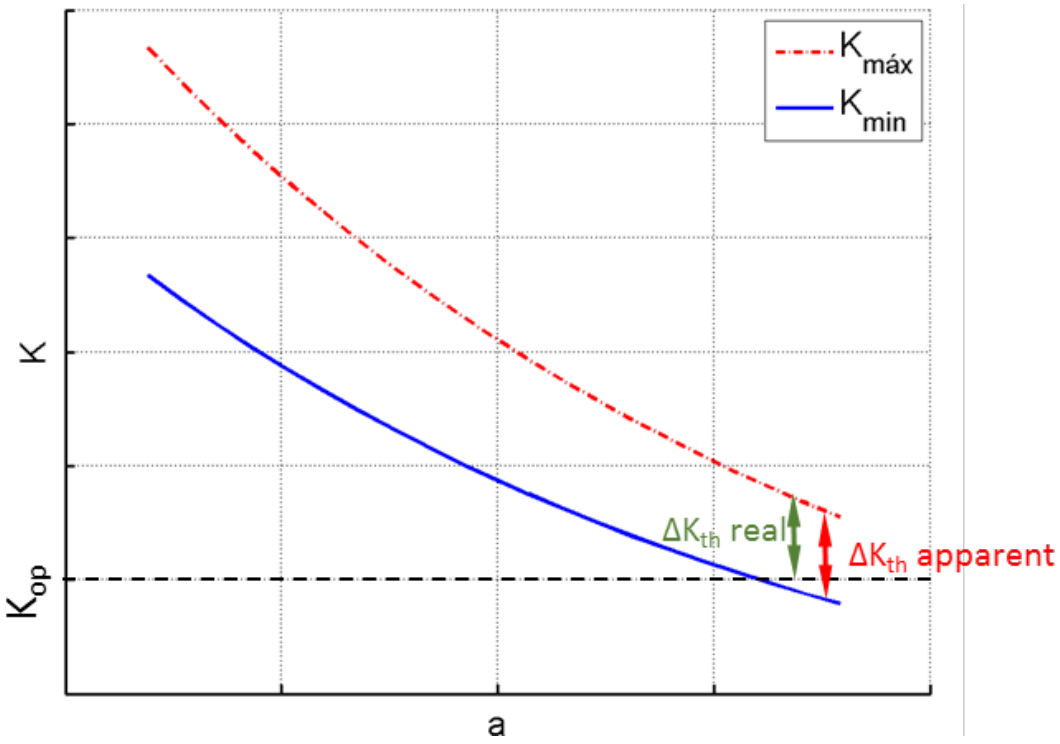

Figure 5.1: Schematic presentation of the ASTM threshold determination method.

According to this, the *K*-decreasing (ASTM E647) methodology presents anomalies since the load is shed in steps and the amount of crack-wake plastic deformation produced during a test is directly related to the magnitude of previously applied loads leading to remote plasticity-induced crack closure, which could generate artificially high threshold values.
An experimental study on two structural steels (normalized C45 and 25CrMo4 grades) conducted by Carboni and Regazzi [49] to determine the influence of the adopted technique onto the $\triangle K_{th}$ value lead to conclude that, in the threshold region, traditional approaches based on *K*-decreasing tests tend to systematically overestimate the $\triangle K_{th}$.

Despite of this, the test method defined by ASTM is the only standardized test designed to produce the range of fatigue crack thresholds.
Among others, the constant K_{max} with increasing K_{min} method [50] was implemented to solve this problem, as this maintains high $R-ratio$ levels that keep the entire crack open, as schematized in Figure 5.2, circumventing the difficulties and limitations mentioned above.

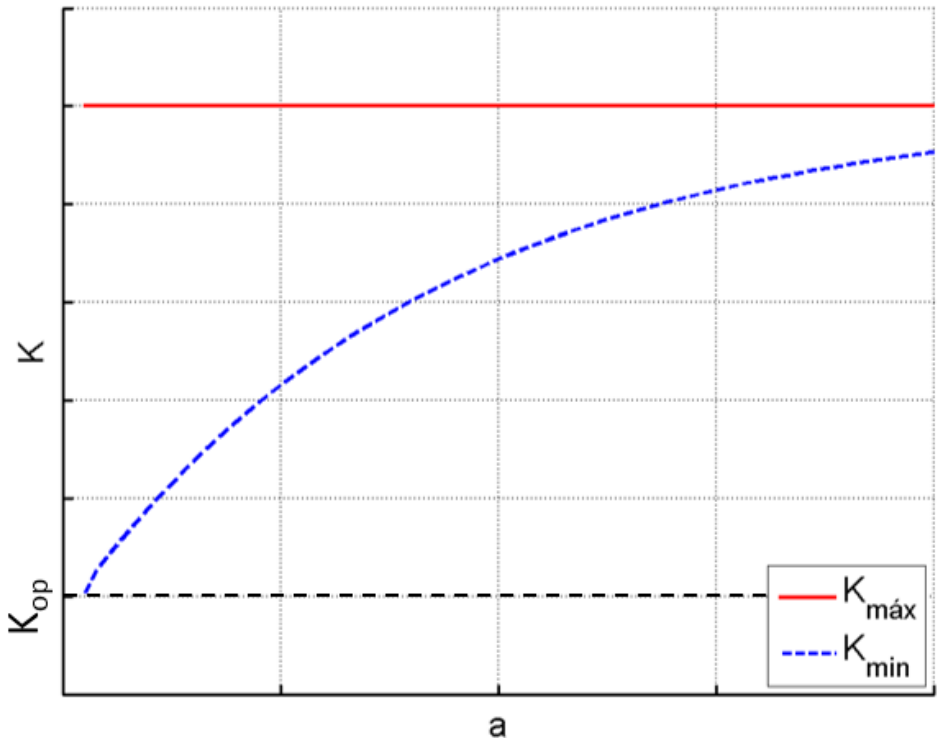

Figure 5.2: K_{max} with increasing K_{min} method for threshold determination.

5.2 Specimens

According to the ASTM E647 standard two main types of specimens can be used in fatigue crack growth rates tests, the compact specimen, C(T), which is a single edge-notch specimen that can be loaded in tension and the middle tension, M(T), which is a center cracked specimen that can be loaded in either tension-tension or tension-compression. In this work C(T) specimens were used because this type of specimen has the advantage of requiring a smaller amount of material then the M(T) specimen, and only tension-tension loads ($R > 0$) were used. Figure 5.3 shows the adopted dimensions for the C(T) specimens, according to the ASTM E647 standard.

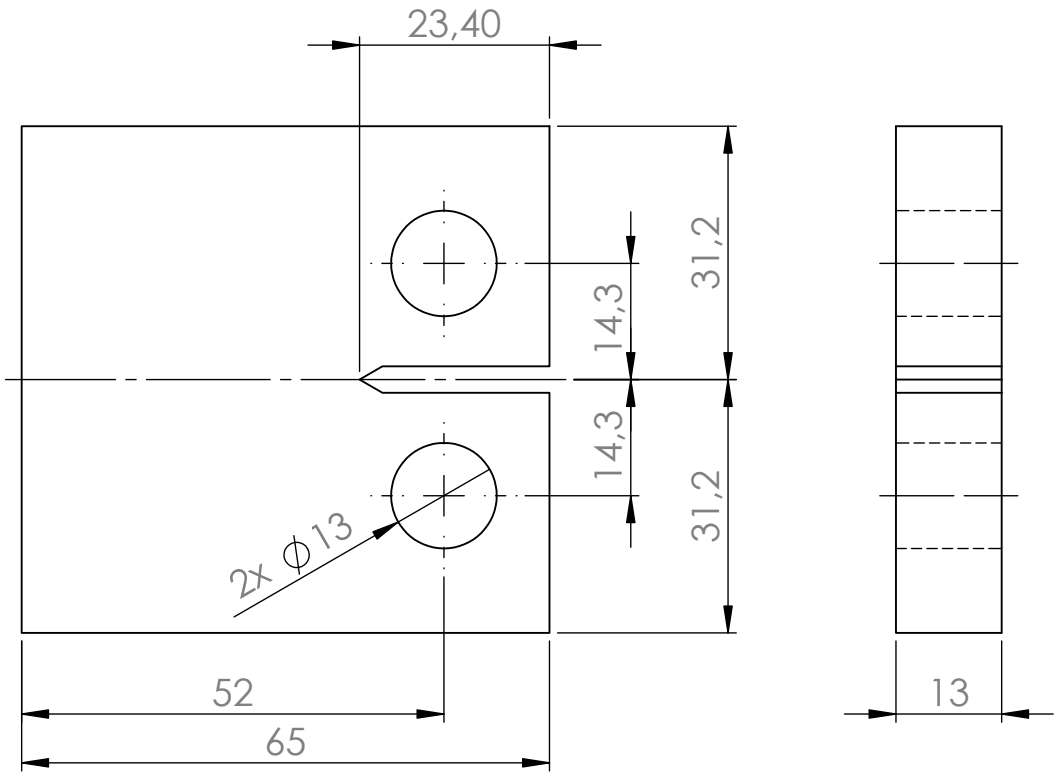

Figure 5.3: C(T) specimens dimensions [mm].

The same dimensions were adopted for the specimens taken from the wheel and from the rail. The 23.4 mm long and 0.3 mm thick notch was opened by electric discharge machining (EDM)[5]. To calculate the stress intensity factor range ($\triangle K$) the stress intensity factor calibration presented in the ASTM E647 standard for C(T) specimens can be used, as follows:

$$\triangle K = \frac{\triangle P}{B\sqrt{W}} \frac{2+\alpha}{(1-\alpha)^{3/2}} \left(0.886 + 4.64\alpha - 13.32\alpha^2 + 14.72\alpha^3 - 5.6\alpha^4\right) \tag{5.1}$$

where:

$\alpha = a/W$,

a: crack length;

W: specimen width;

B: specimen thickness;

$\triangle P$: load range.

This calibration is valid only when $a/W \geq 0.2$, which was verified in the presented tests. Since the main goal of the presented study is to characterize the behavior of the wheel and rail steels in the presence of defects near the contact surfaces, the wheel specimens were extracted from the wheel tread and the rail specimens from the rail head, as shown in Figure 5.4a and Figure 5.4b respectively.

[5]Performed at AUTOCONCEPTUS, Rio Tinto, Porto

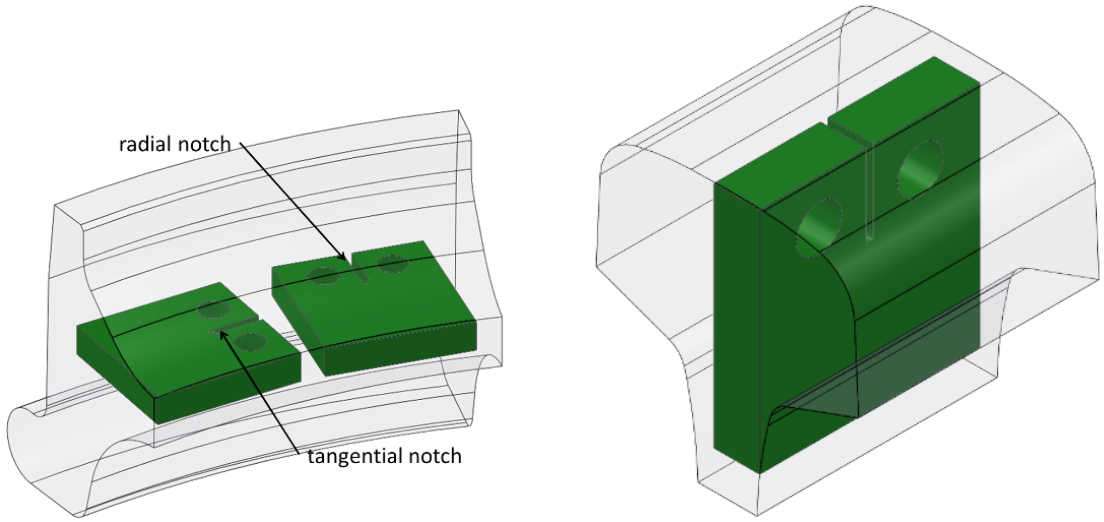

(a) location of wheel C(T) specimens.

(b) location of rail C(T) specimens.

Figure 5.4: Location for C(T) specimens extraction.

Two different orientations for the C(T) specimens taken from the wheel were chosen; in one of them the notch is oriented in the radial direction (R) and in the other the notch is oriented in a direction parallel to the tangent of the rolling surface of the wheel (T). Specimens taken from the rail had the notch oriented in the perpendicular direction to the rail head surface. This orientation was chosen since it represents the most dangerous crack propagation direction, which could cause the total separation of the rail. A fatigue pre-crack must be made in order to provide a sharpened fatigue crack which ensures that the effect of the machined notch is removed from the *K*-calibration, and the effects on subsequent crack growth rate data caused by changing crack front shape or pre-crack load history are eliminated. The pre-crack length is a function of specimen dimensions and, according to the ASTM E647 standard, for the considered geometry it must be at least 1.3 mm.

5.3 Experimental methodology

In the present study three different methodologies were used to characterize the fatigue crack propagation behavior of the two studied materials. The *K*-decreasing test procedure, described in the ASTM E647 standard, and the K_{max} constant with increasing K_{min} procedure were used to characterize fatigue crack propagation near the threshold; whereas the *K*-increasing with constant load range ($\triangle P$) method, also described in the ASTM E647 standard, was used in the Paris law regime. According to the ASTM E647 standard the *K*-increasing with constant load amplitude method is recommended for fatigue crack growth rates above 10^{-5} mm/cycle and the *K*-decreasing test procedure is better suited for rates below 10^{-5} mm/cycle. The constant K_{max} with increasing K_{min} method was used in com-

parison to the *K*-decreasing test procedure, in order to evaluate which able to obtain the more conservative value of threshold.

Fatigue crack growth rates in the Paris law regime

The *K*-increasing test method was used to obtain the fatigue crack growth rates of the wheel and rail materials in the Paris law regime. In the *K*-increasing with constant load amplitude method, as the name suggests, the load is kept constant along the test and $\triangle K$ increases as the fatigue crack tip becomes more distant from the point where the load is applied. This is quite visible in Figure 5.5.

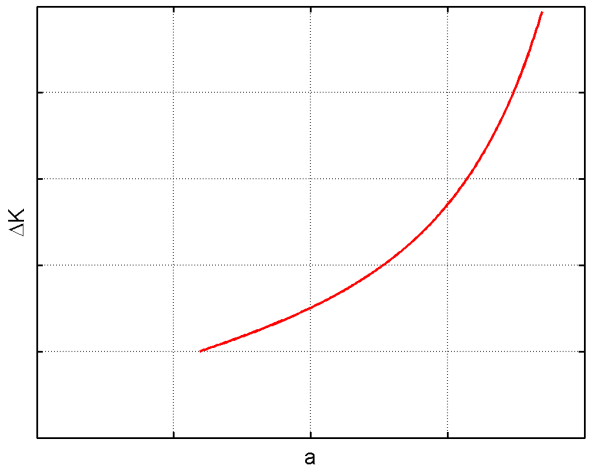

Figure 5.5: Typical behavior of *a vs.* $\triangle K$ during a *K*-increasing test.

Figure 5.6 shows the typical behavior of crack length vs. nr. of cycles during a *K*-increasing test.

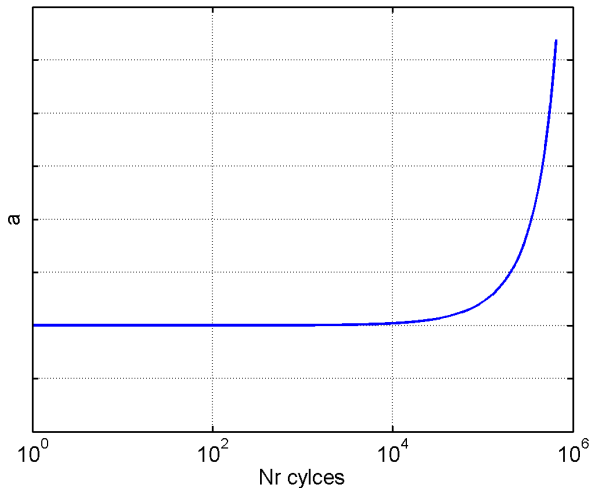

Figure 5.6: Typical behavior of crack length vs. nr. of cycles during a *K*-increasing test.

Fatigue crack growth rates can be calculated from the experimental data a *vs.* N using two approaches *i*) the secant method or *ii*) the incremental polynomial method. Both methods are

suitable for the *K*-increasing with constant load test. However, only the 7 point incremental polynomial method, described in the ASTM E647 standard, was used. To obtain an extended range of the fatigue crack propagation behavior of the studied materials three different load ratios, R = 0.1, R = 0.4 and R = 0.7, were tested, including two different directions of crack propagation on the wheel material, as shown before.

Near-threshold propagation fatigue crack growth rates

The *K*-decreasing procedure is started by load cycling at a stress intensity factor range ($\triangle K$) and maximum stress intensity factor (K_{max}) levels equal or greater than the terminal pre-cracking values. Subsequently, forces are decreased (shed) as the crack grows until the lowest $\triangle K$ or crack growth rate of interest is achieved. This test method is recommended by the ASTM E647 standard to obtain the fatigue crack growth rates in the near-threshold. During the force shedding procedure the normalized *K*-gradient value was kept algebraically equal or greater than - 0.08 mm^{-1}:

$$K - gradient = \frac{1}{\triangle K}\frac{d\triangle K}{da} > -0.08mm^{-1} \tag{5.2}$$

as recommended by the ASTM E647 standard. This requirement aims at ensuring that the step under a given load range does not correspond to such a large crack length variation ($\triangle a$) increment that the $\triangle K$ of the previous step is exceeded. This will prevent anomalous data resulting from reductions in the stress-intensity factor and associated transient growth rates. Force shedding of adjacent steps does not exceeded 10% and new fatigue crack growth rates were calculated only after a minimum crack extension of 0.50 mm, in order to avoid effects associated with discrete variations of load range: during the extension of up to 0.50 mm no crack growth data is recorded since it may be influenced by transient growth phenomena. An example of this experimental procedure is shown in Figure 5.7.

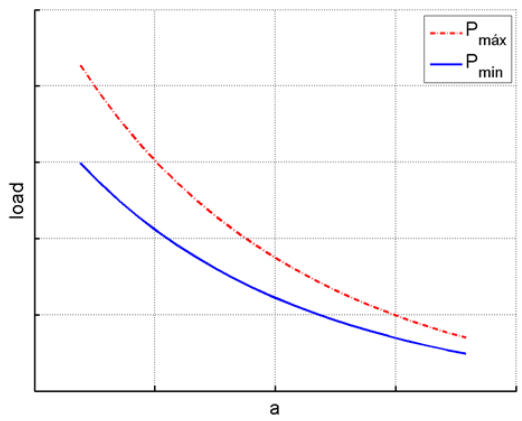

(a) Load shedding sequence.

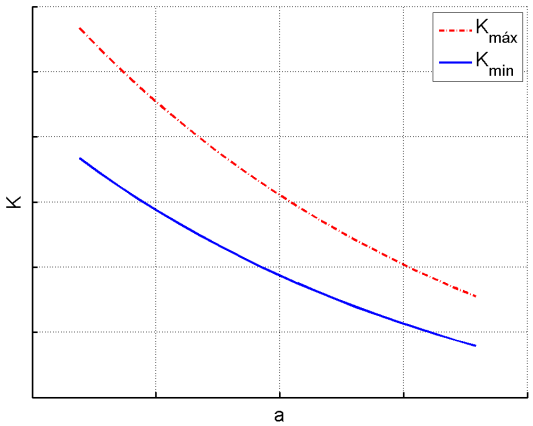

(b) K_{max} and K_{min} vs. a for the *K*-decreasing test.

Figure 5.7: Typical *K*-decreasing test by stepped force shedding.

For the *K*-decreasing tests where force is shed in decremental steps the secant method was used to calculate the fatigue crack growth rates. Three different load ratios $R = 0.1$, $R = 0.4$ and $R = 0.7$ were tested, as the value of the threshold is function of the load ratio when the *K*-decreasing test is used.

As an alternative to the *K*-decreasing method the constant K_{max} with increasing K_{min} methodology was used to determine the fatigue crack growth thresholds of railway wheel and rail steels.

For the constant K_{max} with increasing K_{min} test procedure, the applied loads are changed to maintain constant the K_{max} value, while the K_{min} value is increased until the crack growth rate reaches 1×10^{-7} mm/cycle, the value specified by the ASTM E647 standard for the threshold. In Figure 5.8 [6] an example of this methodology is shown.

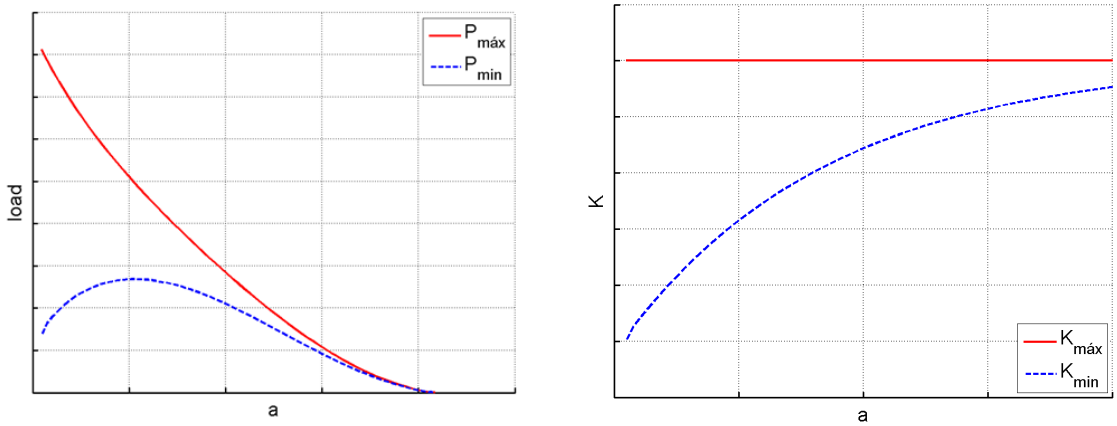

(a) P_{max} and P_{min} along K_{max}constant method. (b) K_{max} and K_{min} along K_{max}constant method.

Figure 5.8: Nominal values of P_{max},$P_{min}K_{máx}$ and K_{min} as a function of the crack length along the constant $K_{máx}$ with increasing K_{min} test.

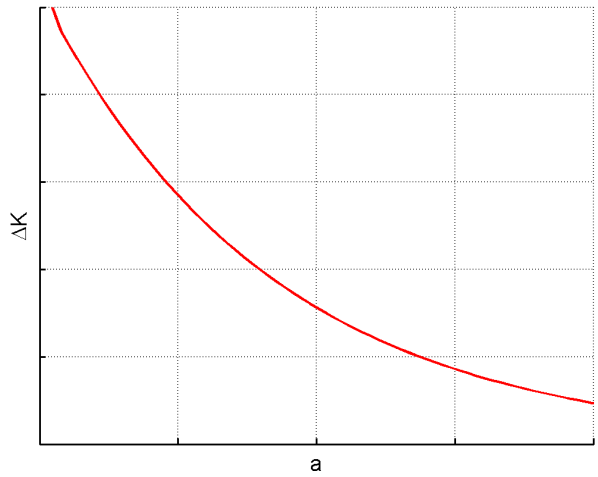

Figure 5.9: $\triangle K$as a function of the crack length along the constant $K_{máx}$ with increasing K_{min} test.

[6]These Figures were obtained using a developed MATLAB® code included in Appendix A

Similarly to the *K*-decreasing test, during the constant K_{max} with increasing K_{min} test the normalized *K-gradient* value was kept algebrically equal or greater than - 0.08 mm^{-1}.
As it could be expected, since the K_{max} is kept constant and theK_{min} is increased along the test, the load ratio increases as theK_{min} is increased, as shown in Figure 5.10. This behavior enables to obtain a threshold value that is independent from the load ratio.

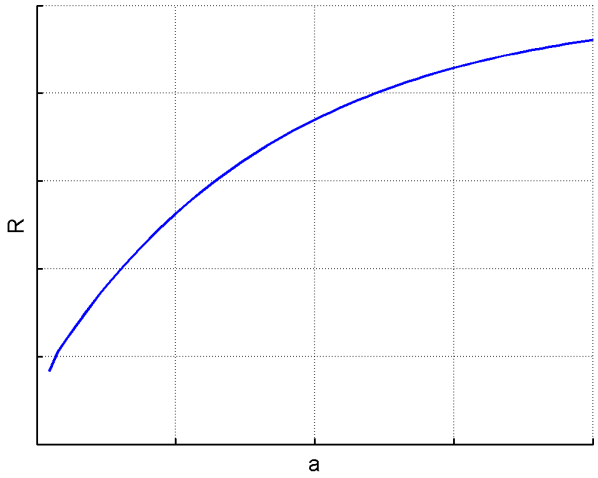

Figure 5.10: Load ratio as a function of the crack length along the constant K_{max} with increasing K_{min} test.

Experimental apparatus

All fatigue crack growth (FCG) tests were performed using an MTS® servo-hydraulic machine of 100 kN, shown in Figure 5.11, capacity, at room temperature. A sinusoidal waveform was used in all tests.

Figure 5.11: MTS® servo-hydraulic machine used to perform the fatigue crack growth tests.

The used servo-hydraulic machine was equipped with two traveling microscopes in order to measure crack length variations down to 0.01mm, using digital rulers and 20x magnifiers, as shown in Figure 5.12.

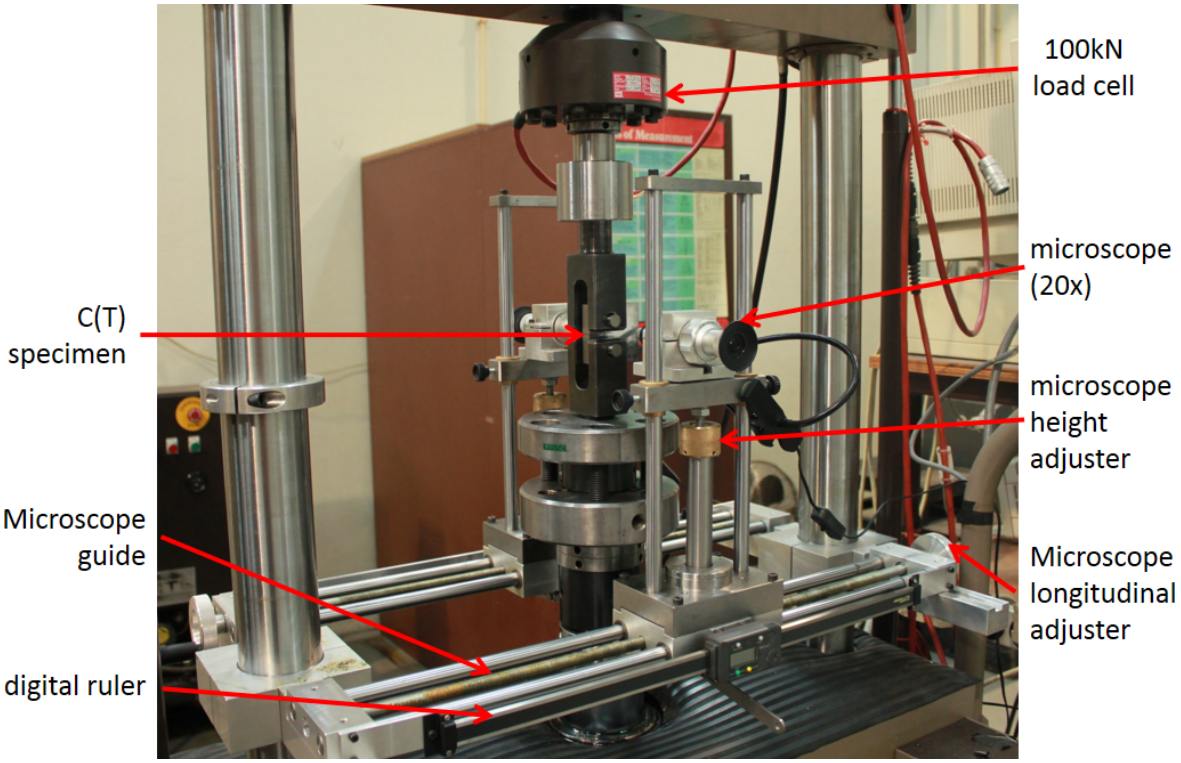

Figure 5.12: Experimental apparatus for fatigue crack growth measurements.

Because a visual measurement technique was used, the average value of the two surface crack lengths was considered to make all calculations, as recommended in the followed standard.

5.4 Results

Fatigue crack growth rates

Figure 5.13 and Figure 5.14 show the obtained fatigue crack growth rates for the wheel and rail materials, respectively. The points used for Paris law determination are represented by full symbols, whereas the near-threshold data for the wheel material are represented by open symbols.

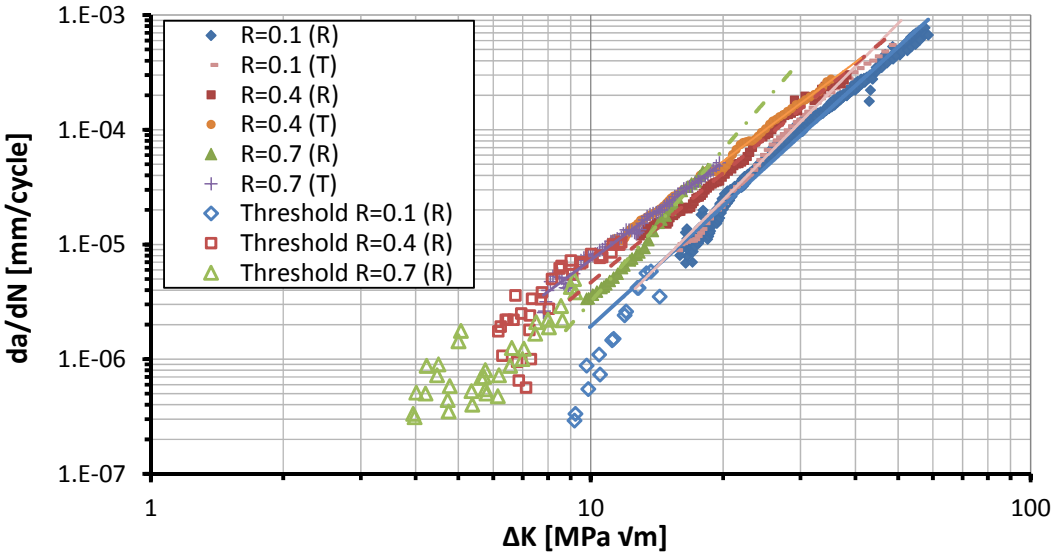

Figure 5.13: Fatigue crack growth rates for wheel material.

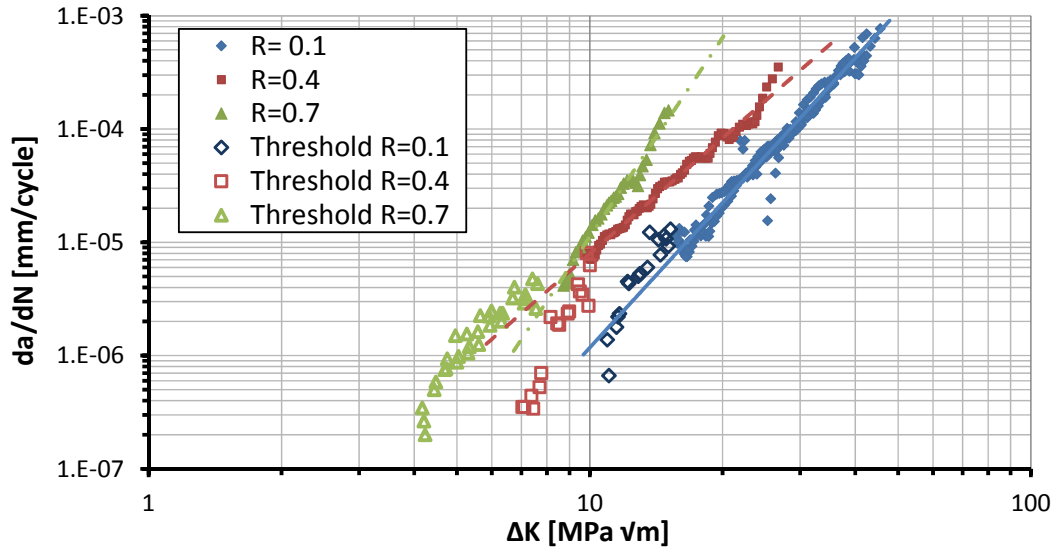

Figure 5.14: Fatigue crack growth rates for rail material.

The obtained Paris law constants, C and m, were derived by fitting the linear zone using a power function as:

$$\frac{da}{dN} = C\,(\triangle K)^m \tag{5.3}$$

These constants, including the R^2, and the fatigue crack growth threshold value are listed in Table 5.1 for the wheel and in Table 5.2 for the rail.

Table 5.1: Wheel material Paris law constants.

$R-ratio$	notch orientation	Paris law constants (fitting)		
		C	m	R^2
0.1	radial	6.33E-10	3.48	0.984
	tangential	2.29E-10	3.87	0.992
0.4	radial	3.16E-09	3.17	0.993
	tangential	9.89E-09	2.87	0.997
0.7	radial	1.24E-10	4.41	0.992
	tangential	1.05E-08	2.84	0.980

Table 5.2: Rail material Paris law constants.

$R-ratio$	Paris law constants (fitting)		
	C	m	R^2
0.1	6.64E-11	4.25	0.963
0.4	3.19E-09	3.39	0.987
0.7	1.61E-11	5.84	0.969

Note that all Paris law constants were obtained using da/dN in mm/cycle and $\triangle K$ in MPa $m^{1/2}$ units.

For the rail steel the influence of $R-ratio$ is higher than for the wheel steel, and a relevant change in the Paris law slope for $R = 0.7$ is observed.

It is observed that for the wheel a small influence of $R-ratio$ is found, with greater *R* implying higher fatigue crack growth rates. The literature suggests that in the Paris law regime little influence of $R-ratio$ is expected, [51], as observed *e.g.* in [39, 52].

The obtained results for the wheel steel did not reveal a significant difference between the fatigue crack propagation behavior in the two studied directions, except for the load ratio $R = 0.7$, where the Paris law slopes are very different for the two directions. For $R = 0.7$ and da/dN around 1×10^{-5} mm/cycle, the crack growth rates in the radial direction become lower than those obtained for $R = 0.4$ tests, suggesting the need for further testing in these conditions. The da/dN *vs.*$\triangle K$ data for values above 25 to 30 MPa $m^{1/2}$ collapses to a single curve, suggesting that there is little crack closure associated with these levels of $\triangle K$. However, there is an apparent $R-ratio$ dependency in the near-threshold region; the near-threshold results obtained indicate lower threshold values for higher $R-ratio$, a fact that is possibly associated with crack closure phenomena, a behavior also reported by El-Shabasy and Lewandowski in [39].

For the wheel steel the behavior observed indicates lack of an $R-ratio$ effect at moderate $\triangle K$ and $R-ratio$ dependency in the near-threshold region. Such behavior is described for

other types of steels for instance in [53, 54]. This suggests that crack closure may not be appropriate for modeling crack growth in these steels from $\triangle K_{th}$ up to large values of $\triangle K$ and further efforts needs to be given to explaining this phenomenon.

Threshold results

The $\triangle K_{th}$ values were calculated from the load and crack length at which the crack growth is less than 0.1 mm per 1×10^6 cycles (da/dN $<1\times10^{-7}$ mm/cycles). The obtained results are shown in Table 5.3 for the *K*-decreasing test and in Table 5.4 for the K_{max} with increasing K_{min} test.

A comparison of the results obtained with the two applied experimental methodologies is shown in Figure 5.15.

Table 5.3: ASTM E647 *K*-decreasing test results.

Material	R	$\triangle K_{th}$ [MPa m$^{1/2}$]	$K_{máx\,th}$ [MPa m$^{1/2}$]	*K-gradient* [1/mm]
wheel	0.1	9.25	10.28	-0.080
	0.4	6.19	10.32	-0.080
	0.7	3.42	11.41	-0.070
rail	0.1	10.03	11.14	-0.060
	0.4	6.42	10.71	-0.060
	0.7	3.86	12.86	-0.065

Table 5.4: Constant $K_{máx}$ with increasing $K_{máx}$ method results.

Material	R_{start}	R_{th}	$\triangle K_{th}$ [MPa m$^{1/2}$]	$K_{máx}$ [MPa m$^{1/2}$]	*K-gradient* [1/mm]
wheel	0.5	0.67	4.05	12	-0.075
rail	0.5	0.67	3.95	12	-0.075

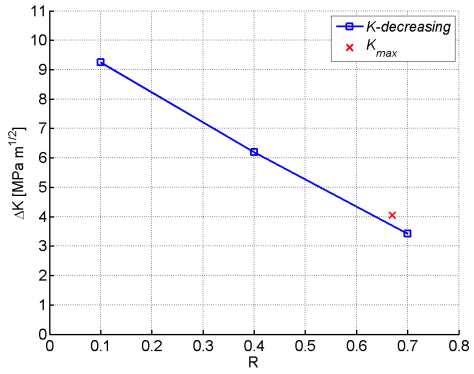

(a) Wheel material results

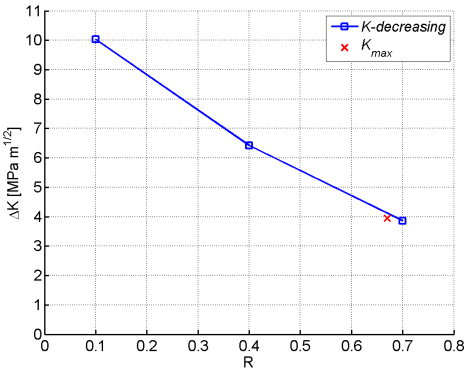

(b) Rail material results

Figure 5.15: Comparison of threshold results using the two different methodologies.

On the basis of the limited experimental evidence obtained in this work, it is concluded that the ASTM method leads to higher $\triangle K_{th}$ values than K_{max} constant procedure.
It can be observed that the measured threshold stress-intensity range for fatigue-crack propagation, $\triangle K_{th}$, decreases as the load ratio is increased, a phenomenon also reported by Boyce in [46].
In the K_{max} constant procedure it is assumed that the crack stops growing in a closure free situation due to the high $R - ratio$.
For the high $R - ratio$ tested according to the ASTM procedure the obtained results are very similar to the results obtained with K_{max} constant procedure.

Comparison with results from the literature

The obtained results in the Paris law regime were compared with others presented in the literature [39, 43, 52, 55, 56, 57]. The comparison was based on the Paris law constants shown in Table 5.5 and in the graphical representation presented in Figure 5.16. Table 5.5 also shows some values of $\triangle K_{th}$ found in the referred literature.
A good general agreement was found in this comparison and the relatively small differences identified may be due to differences in the chemical composition or wheel/rail fabrication process.
Given the direct comparability of the present data and data of Table 5.5, the lower, more conservative, values obtained in the present work are noticed.

Table 5.5: Results from the literature.

Author	*R*	Material	Paris law constants		$\triangle K_{th}$ [MPa m$^{1/2}$]
			C	m	
El-Shabasy[39]	0.1	rail	-	3.50	9.1
El-Shabasy [39]	0.7	rail	-	6.20	6.0
Zain [43]	0.1	rail	2.63E-12	3.29	-
Kim[52]	0.1	rail	4.47E-09	3.13	-
Heshmat [55]	0.1	rail (pearlitic)	1.13E-11	2.17	-
Sivaprasad [56]	0.1	cast wheel (rim-radial)	1.08E-09	3.35	12.97
Sivaprasad [56]	0.1	cast wheel (rim-circumferential)	1.08E-10	4.07	12.65
Sivaprasad [56]	0.1	forged wheel (rim-radial)	8.21E-10	3.53	12.07
Sivaprasad [56]	0.1	forged wheel (rim-circumferential)	7.39E-11	4.30	12.18
Hamam [57]	0.2	wheel	1.95E-09	3.40	-
Hamam [57]	0.4	wheel	2.47E-09	3.38	-

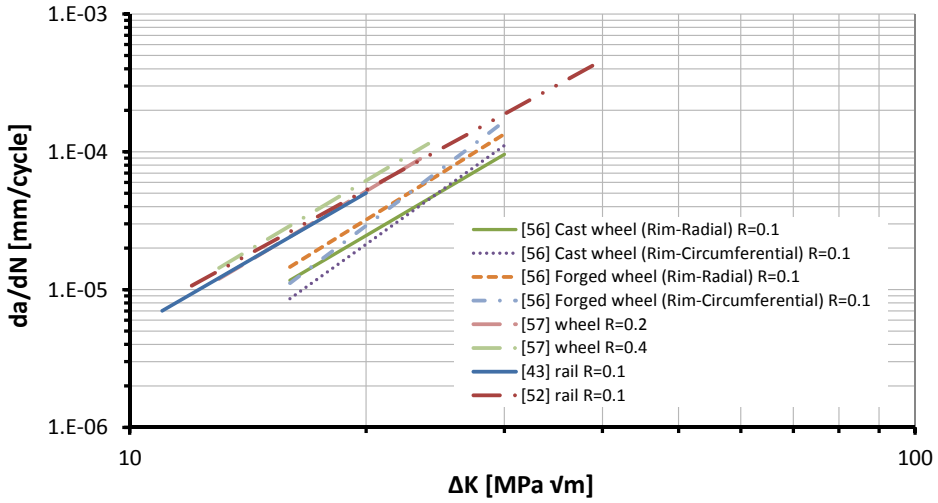

Figure 5.16: Simplified representation of the results presented in the literature.

5.5 Crack surface observations

Some fatigue surfaces were visually observed and on a Scanning Electron Microscope (SEM) allowing to observe the ductile behavior of the wheel material and the brittle behavior of the rail material, as shown in Figure 5.17 and Figure 5.18. In the railway wheel material dimpled appearance, typical of ductile fracture of metallic materials, is identified in the SEM picture of the final rupture and in the rail material the SEM picture shows intergranular fracture (brittle) in the SEM picture of the final rupture.

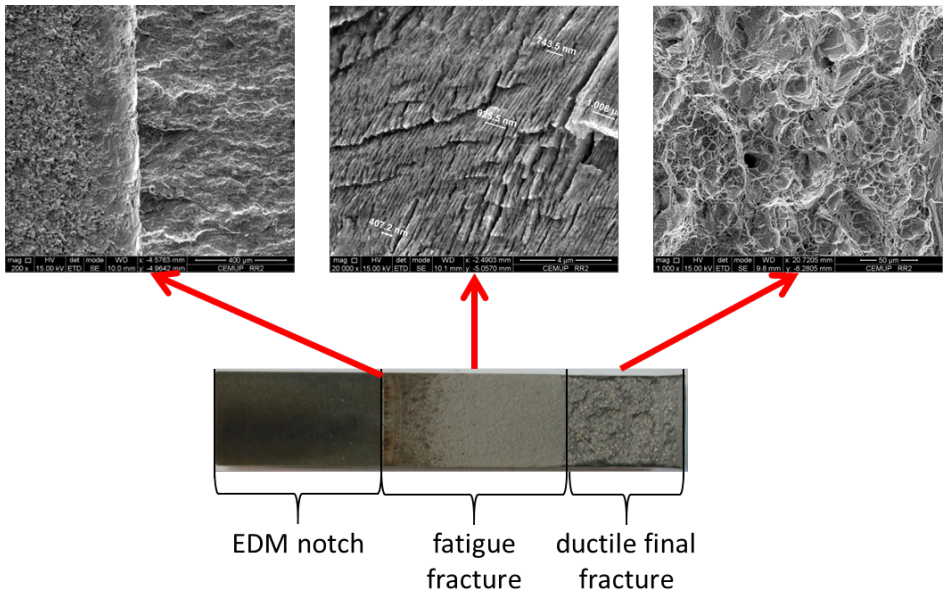

Figure 5.17: Wheel specimen fatigue surface.

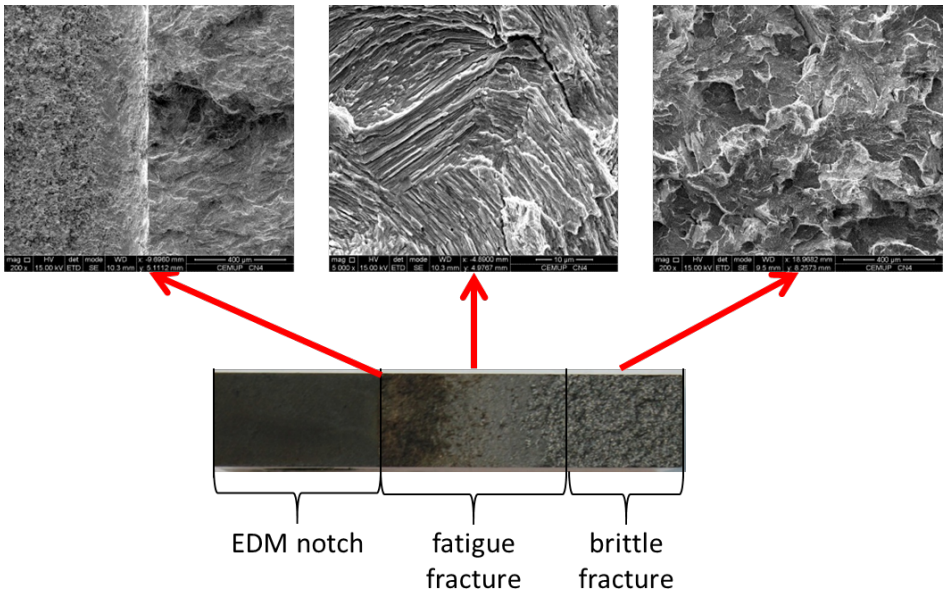

Figure 5.18: Rail specimen fatigue surface.

5.6 Concluding remarks

Mode I fatigue crack growth tests were performed according to the ASTM E647 standard on C(T) specimens taken from a Spanish high speed AVE train used wheel and a UIC60 rail, tested with 0.1, 0.4 and 0.7 load ratios.

The rail material presents higher fatigue crack growth rates than the wheel material.

The effect of $R-ratio$ is most noticeable in the rail material. A good agreement between results obtained with the *K*-decreasing and *K*-increasing methodologies was found in the fatigue crack growth rate transition, da/dN $\approx 10^{-5}$ mm/cycle.

Data obtained for the wheel and rail materials shows lower values of $\triangle K_{th}$ for higher $R-values$.

Present near threshold values are lower than published data found in the literature, also obtained using the load shedding technique.

On the basis of the limited experimental evidence obtained in this work, it is concluded that the ASTM method leads to higher $\triangle K_{th}$ values than K_{max} constant procedure.

It was observed that the measured threshold stress-intensity range for fatigue-crack propagation, $\triangle K_{th}$, decreases as the load ratio is increased.

In the K_{max} constant procedure it is assumed that the crack stops growing in a closure free situation due to the high $R-ratio$.

For the high $R-ratio$ tested according to the ASTM procedure the obtained results are very similar to the results obtained with K_{max} constant procedure.

Chapter 6

Mixed mode fatigue crack propagation

Mixed-mode (mode-I and mode-II) fatigue crack growth tests were performed on Compact Tension Shear (CTS) specimens with a thickness of 9 mm, taken from a Spanish AVE train wheel to evaluate the fatigue behavior of wheel steel under mixed mode loadings.
Fatigue crack growth rates and the propagation direction (angle) of a crack subjected to mixed mode loading were measured.
A finite element analysis was performed in order to obtain the K_I and K_{II} values for the tested loading angles.
The crack propagation direction (angle) for the tested mixed mode loading conditions was experimentally measured and numerically calculated, and the obtained results were then compared in order to validate the used numerical techniques.
The adopted methodologies, specimens' dimensions and extraction position, and the obtained results will be presented and discussed in the following paragraphs.

6.1 Introduction

A great number of the fatigue crack growth studies are commonly performed under mode-I loading conditions. However, single-mode loading rarely occurs in practice, and in many cases cracks are not normal to the maximum principal stress direction. Under mixed-mode loading conditions a crack will deviates from its original direction, [58].
Several research workers indicate that rolling contact fatigue cracks are subjected to mixed mode I and II loading cycles, see *e.g.* Wong *et al.* in [59]. Wheel shelling and rail squats are examples of defects originated in cracks that cause loss of large pieces of metal from wheel treads and rail head as a result of wheel-rail rolling contact fatigue. Fatigue tests performed to obtain the fatigue crack growth rate under the mixed loading (mode I + II) can be helpful to increase safety and reduce railway industry costs related with maintenance of wheels and rails.
It was found that a crack would turn to the direction perpendicular to the higher tensile load if it was initially perpendicular to the lower tensile load. Under shear only loading, the crack

turned to the direction perpendicular to the maximum principal stress [60].
Different specimen geometries and testing methodologies have been used to perform mixed mode tests. Some examples of specimens that can be used to perform mixed mode tests are the compact tension and shear specimen, three or four point bending specimens with an offset edge crack, plate specimen with inclined central or edge crack loaded under tension. These specimens were developed to be tested on uniaxial testing machines. However, there is the possibility to use in-plane biaxial testing machines specially designed to perform this type of tests, and in this case the most used specimen is the cruciform specimen with central crack.
Until now there is no standard methodology for mixed mode testing, making it difficult to compare experimental results from different specimen geometries or testing apparatus. In the literature it can be found that some experimental studies have been conducted under mixed mode loading.
Wheel and rail materials were tested by Akama using an in-plain biaxial testing machine and the obtained results were published in [61].
Wong *et al.* [59] investigated the mechanics of crack growth under non-proportional mixed mode loading using cruciform specimens made by BS 11 normal grade rail steel tested in a biaxial testing machine.
The fatigue crack growth behavior under mixed mode of a 60 kg rail steel, commonly used as a railroad track in Korea, was experimentally investigated by Jung-Kyu Kim and Chul-Su Kim in [52]. The authors reported that fatigue crack growth rate under mixed mode is slower than under mode I, and this difference decreases with the increase of the load *R*-ratio. In this study a special loading device proposed by Richard [62] was used to obtain the mixed-mode loading on a uniaxial testing machine.
Tanaka in [63] presented a study on sheet specimens of aluminum in which the mixed mode is obtained by using an initial crack inclined to the tensile axis.
Tests in compact mixed-mode specimens (CTS) were carried out for several stress intensity ratios of mode I and mode II, K_I/K_{II}, in AlMgSi1-T6 aluminum alloy by Borrego *et al.* [64].
AISI-304 stainless steel samples were tested under mixed-mode (mode-I and mode-II) loading conditions was studied using Compact Tension Shear Specimen (CTS) by Biner [58].
To evaluate the characteristics of mixed mode fatigue crack propagation, it is necessary to introduce a comparative stress intensity factor K_V that considers the effect of mode I (K_I) and mode II (K_{II}) simultaneously.
Several equivalent stress intensity factors have been proposed along times. Among them those presented by Tanaka [63], Richard [62, 65], Richard/Henn [66, 67], Tong *et al.*[68] and Yan *et al.*[69].
Tanaka dealt in [63] with the FCG behavior under mixed mode loadings using the K_V as presented in Eq. 6.1, which was derived from the dislocation model for fatigue crack propa-

gation proposed by Weertman [70].

$$K_V = \sqrt[4]{K_I^4 + K_{II}^4} \tag{6.1}$$

Tong *et al.* [68] and Yan *et al.* [69] combined mode I and mode II loadings based on maximum tangential stress criterion proposed by Erdogan and Sih [71] as:

$$K_V = K_I \cos^3 \frac{\theta}{2} - 3K_{II} \cos^2 \frac{\theta}{2} \sin \frac{\theta}{2} \tag{6.2}$$

where θ is the initial branch crack angle.

Richard [62, 65] proposed another comparative stress intensity factor K_V, that fracture toughness (K_{IC}) of the tested material as:

$$K_V = \frac{1}{2} K_I + \frac{1}{2} \sqrt{K_I^2 + 4 \left(\zeta K_{II}\right)^2} \tag{6.3}$$

where ζ denotes the fracture toughness ratio (K_{Ic}/K_{IIc}).

Accordingly to Richard/Henn criterion [66, 67] the comparative stress intensity factor K_V is calculated as:

$$K_V = \frac{K_I}{2} + \frac{1}{2} \sqrt{K_I^2 + 6K_{II}^2} \tag{6.4}$$

6.2 Experimental methodology

Mixed-mode (mode-I + II) fatigue crack growth tests were conducted on Compact Tension Shear (CTS) specimens with thickness $B = 9$ mm, width $W = 90$mm and a initial notch with a length $a_n = 42.5$mm and 2 mm of thickness opened by EDM, see Figure 6.1. These specimens were taken from an AVE train wheel with the notch oriented in the radial direction, as shown in Figure 6.2.

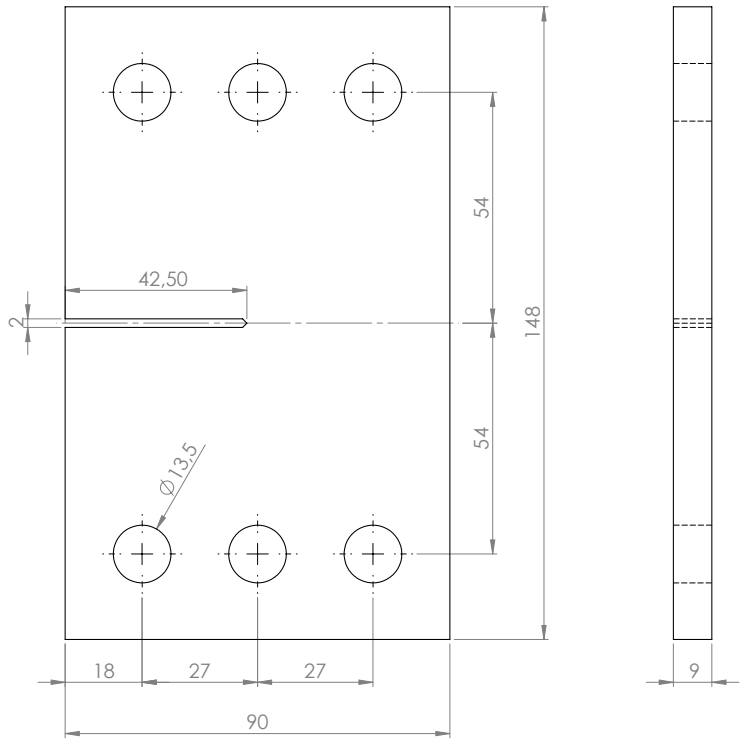

Figure 6.1: Tested CTS specimens dimensions.

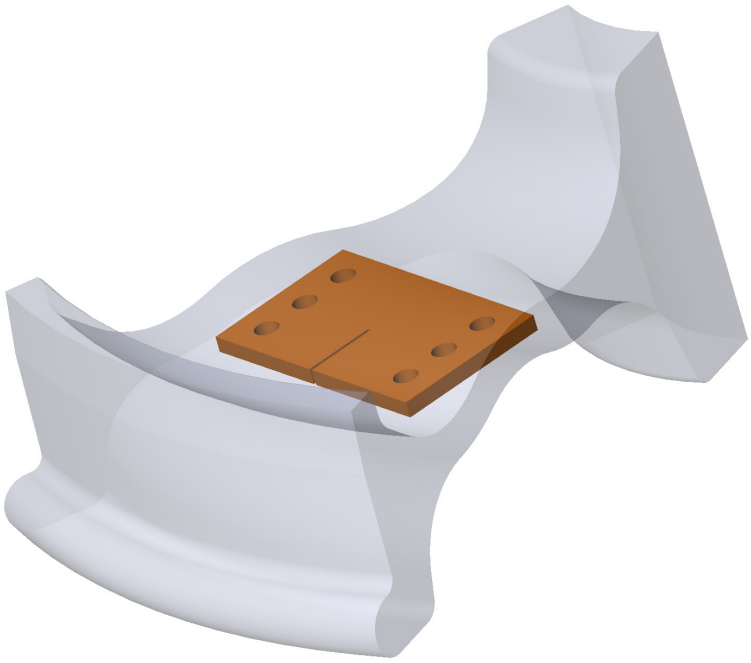

Figure 6.2: CTS specimens extraction position.

Before testing, the specimen surfaces were polished manually in order to facilitate the reading of the crack length.

These experiments were performed using the loading device shown in Figure 6.3.

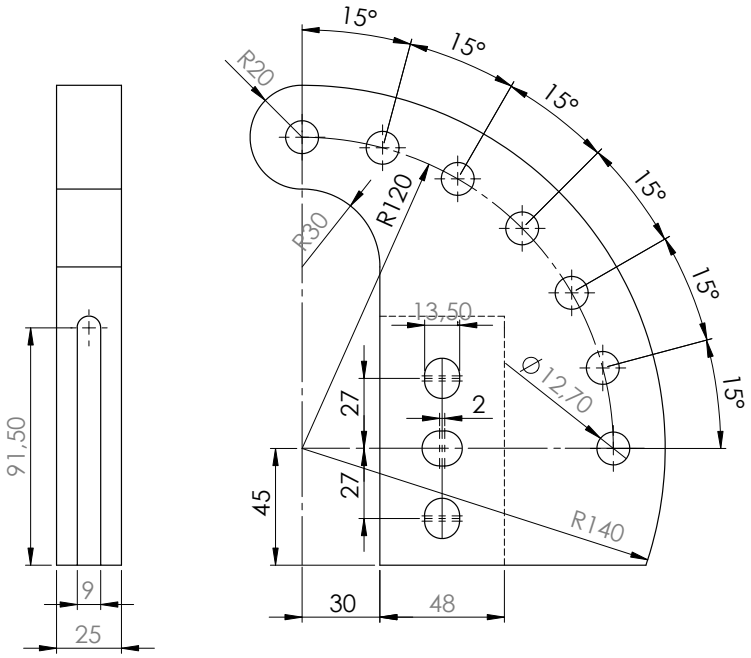

Figure 6.3: Loading device.

Figure 6.4 shows the CTS specimen mounted on the loading device. This apparatus is based on the mixed-mode testing technique proposed by Richard [62].

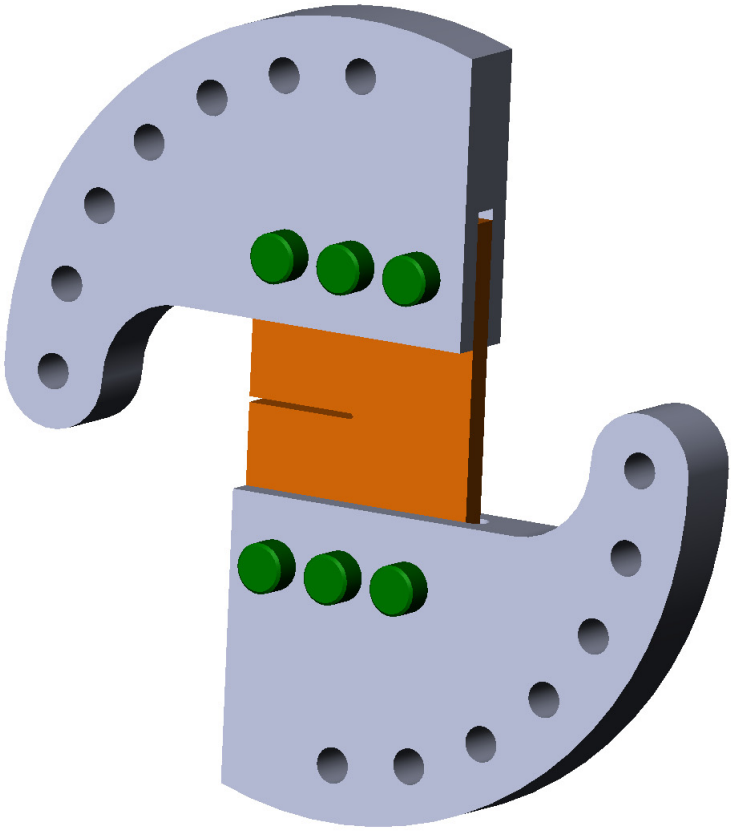

Figure 6.4: CTS specimen mounted on loading device.

This loading device allows to apply pure mode-I, pure mode-II, as well as mixed-mode loading to the CTS specimen using a uni-axial testing machine just by changing the loading angle between the longitudinal axis of the specimen and the load direction applied by the testing machine.
As shown in Figure 6.1 the specimen has circular holes while the loading device has elongated holes. The external holes are elongated in the direction parallel to the crack so that the transmitted forces are normal to the notch. On the other hand, middle holes are elongated perpendicularly to the crack so that only the forces parallel to the notch.
The pre-cracking of CTS specimens was performed under mode I loading with a sinusoidal waveform until an a/W ratio of 0.55 was achieved.
During pre-cracking the load range was decreased in steps of 20%. During the pre-cracking and until the loading device is rotated to obtain the mixed mode loading, the mode I and in mode II crack tip stress intensity factors can be calculated as [62]:

$$K_I = \frac{F\sqrt{\pi a}}{WB}\frac{\cos\alpha}{1-\frac{W}{a}}\sqrt{\frac{0.26+2.65\frac{a}{W-a}}{1+0.55\frac{a}{W-a}-0.08\left(\frac{a}{W-a}\right)^2}} \tag{6.5}$$

$$K_{II} = \frac{F\sqrt{\pi a}}{WB}\frac{\sin\alpha}{1-\frac{W}{a}}\sqrt{\frac{-0.23+1.40\frac{a}{W-a}}{1-0.67\frac{a}{W-a}+2.08\left(\frac{a}{W-a}\right)^2}} \tag{6.6}$$

where F is the applied load, B is the thickness of specimen, and α is the applied loading angle in radians. These equations are valid only in the range of a/W between 0.55 and 0.7.

Experimental apparatus

The experiments were performed in a MTS ® servo-hydraulic uni-axial machine with 100 kN of maximum load capacity. Due to small amount of wheel material only 3 different α angles were tested: 30º, 45º and 60º.
All tests were conducted in air and at room temperature, in load control mode and the load ratio for all loading angles and pre-cracking was kept constant and equal to 0.1. The loads were applied with a sinusoidal waveform.
Figure 6.5 shows the used experimental apparatus.
Because a visual measurement technique was used, the average value of the two surface crack lengths was considered to make all calculations.
Two traveling microscopes were used to measure the crack length variations down to 0.01 mm, using digital rulers and 20x magnifiers.

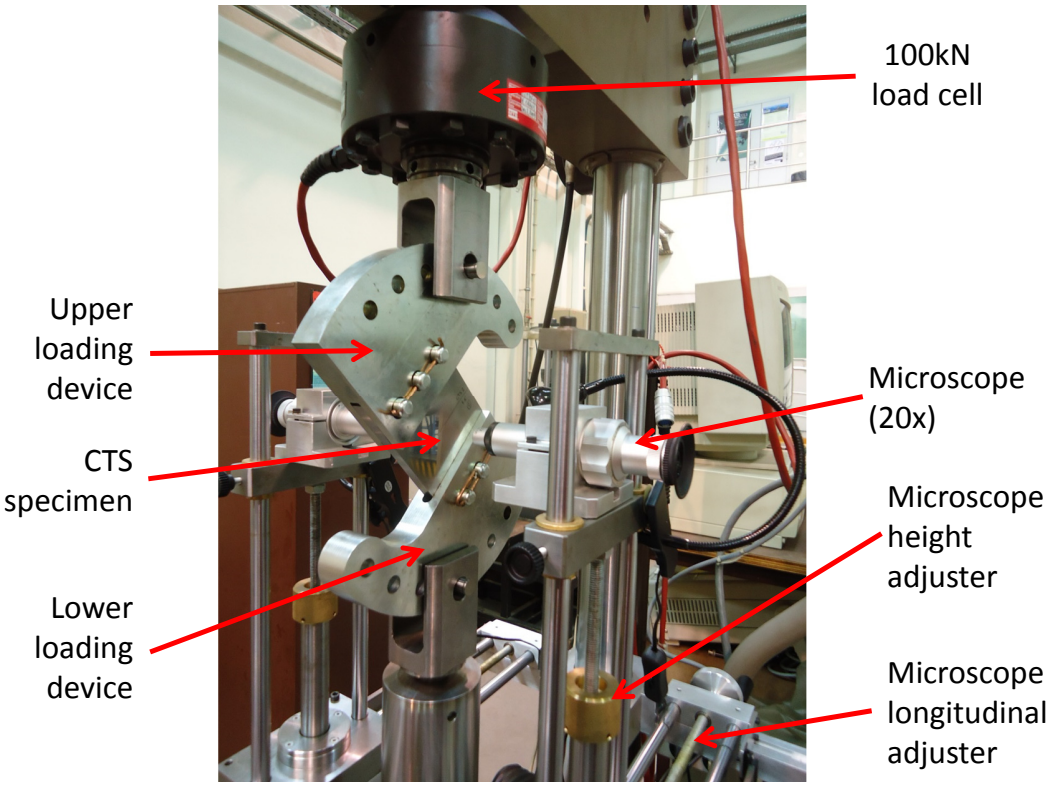

Figure 6.5: Experimental apparatus for fatigue crack growth measurements.

However, these traveling microscopes only allow to measure precisely the crack length in the horizontal direction, so along the mixed mode tests only the horizontal component of the crack propagation was measured.

In these circumstances, the crack profile was drawn using a microscope equipped with two digital micrometers, and the fatigue crack growth data was calculated using trigonometry considering the angle of propagation determined from the drawn crack profile and from the loading device rotation angle, as shown in Figure 6.6.

Eq. 6.7 and Eq. 6.8 were used to calculate the components x and y of the crack.

$$a_x = \frac{a_{i\,exp} - a_{0\,exp}}{\cos(\alpha - \beta)} \times \cos\beta \tag{6.7}$$

$$a_y = \frac{a_{i\,exp} - a_{0\,exp}}{\cos(\alpha - \beta)} \times \sin\beta \tag{6.8}$$

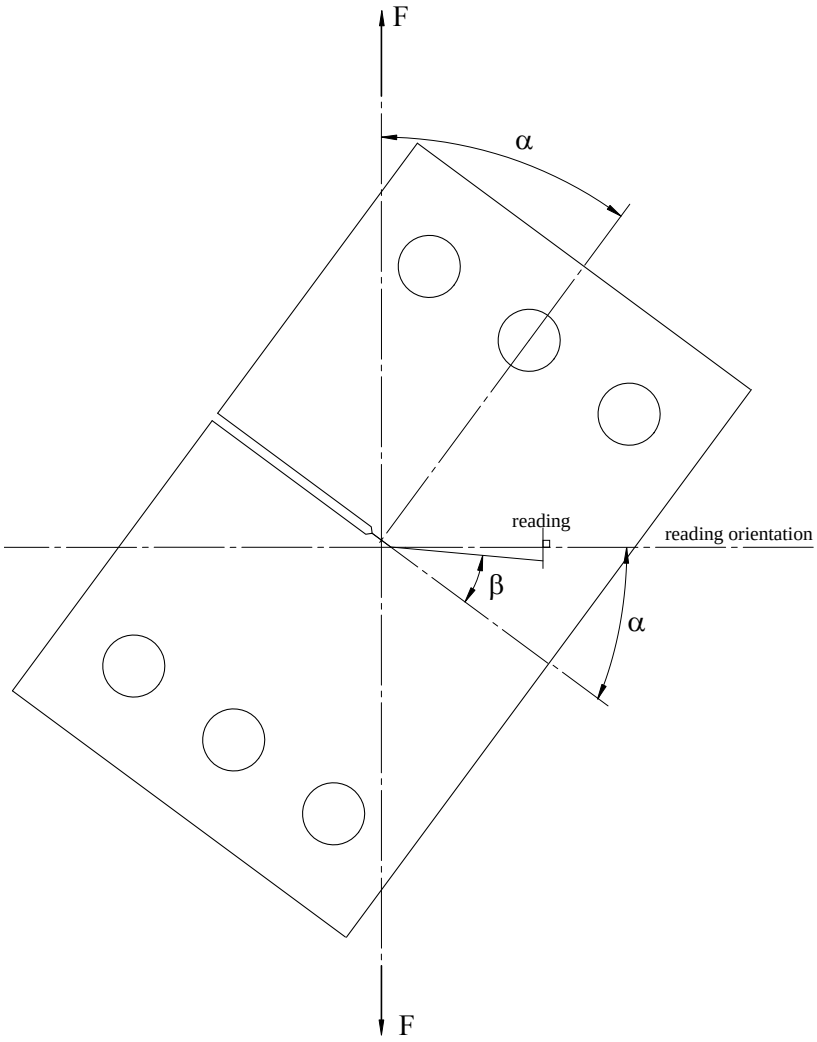

Figure 6.6: Experimental readings of the crack length.

6.3 Stress intensity factor calculations for CTS specimens

The stress intensity factor solutions presented in equations 6.5 and 6.6 are only adequate to be used during the pre-cracking (mode-I) and before the crack suffer any deflection due to mixed mode loading.
Therefore, a numerical analysis was performed in order to obtain K_I and K_{II} stress intensity factors and the initial crack deflection angle (β) under mixed-mode fatigue loading.

Finite element model

Plane stress quadrilateral elements were used to build a 2D finite element model of the tested CTS specimens. Due to lack of loading and geometry symmetry a complete model of the specimens was built.
The Abaqus 6.12-3 [72] commercial finite element package was used to build and analyze the model.

To apply the load and the boundary conditions reference points (*RP*) [72] were positioned ate the center of the specimens holes and then each one was “coupled” [72] to its respective hole. These reference points able to “distribute” the applied load or constraint to the hole circumference nodes. Figure 6.7 shows an example of this methodology for the CTS top-left hole, where the *RP* is located at the center of the hole (in black) and the “coupling” is schematic represented by the yellow lines.

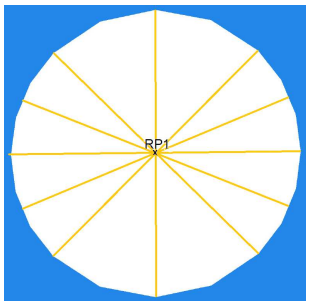

Figure 6.7: CTS top-left hole RP coupling

The considered boundary conditions are presented in Figure 6.8.

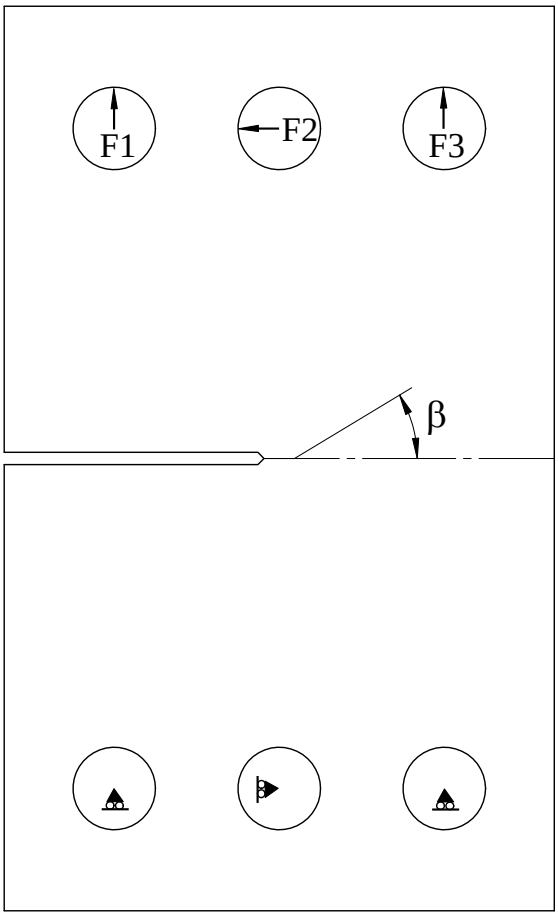

Figure 6.8: Considered boundary conditions.

The uni-axial load F is related with loads applied on the holes as follows, [62]:

$$F_1 = F_6 = F\left(\frac{1}{2}\cos\alpha + \frac{c}{b}\sin\alpha\right) \tag{6.9}$$

$$F_2 = F_5 = F\sin\alpha \tag{6.10}$$

$$F_3 = F_4 = F\left(\frac{1}{2}\cos\alpha - \frac{c}{b}\sin\alpha\right) \tag{6.11}$$

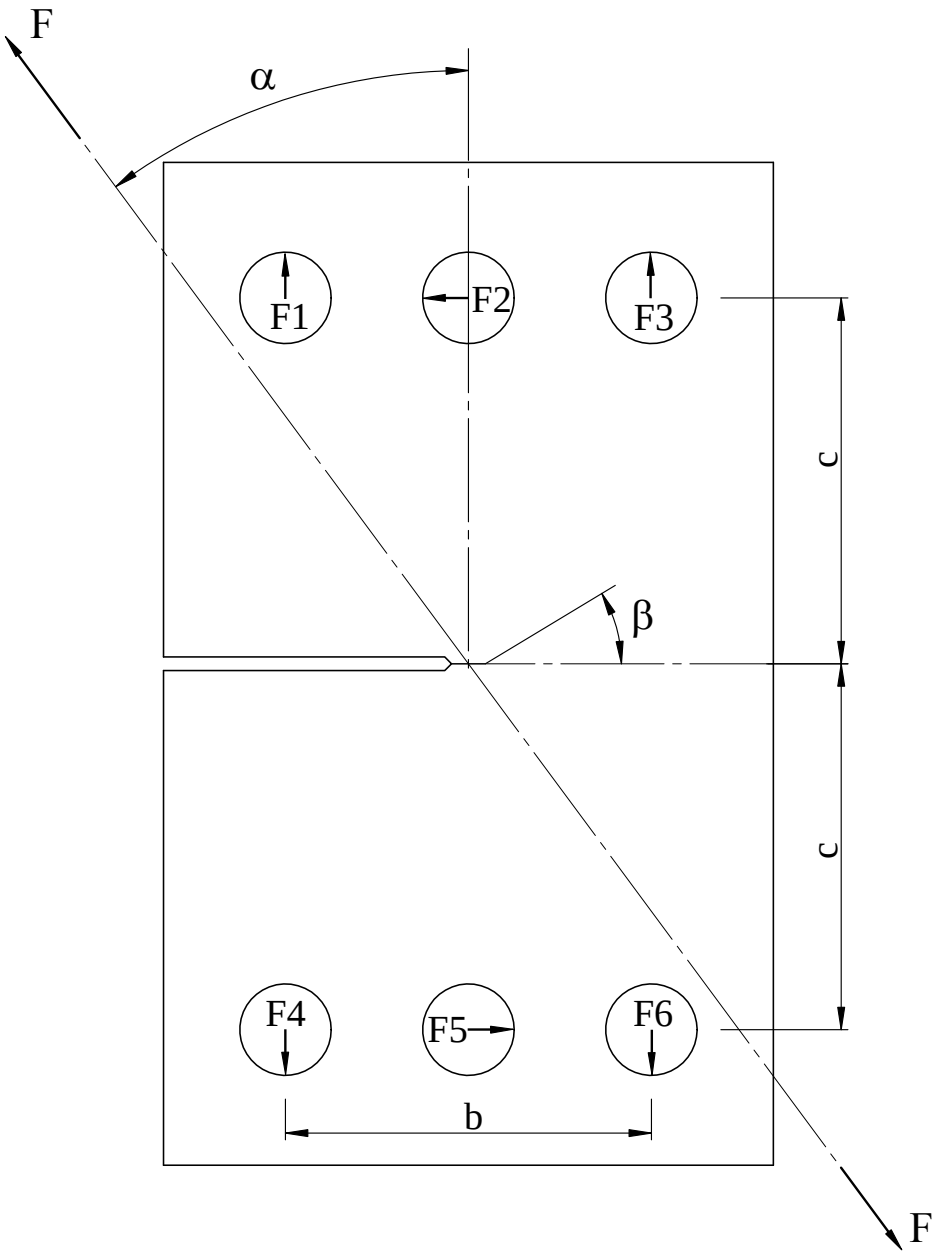

Figure 6.9: Applied load and loads on specimen holes.

Note that the α angle must be used in radians.

The geometrical parameter, β, depicted in Figure 6.8 and in Figure 6.9 is the crack growth direction under under mixed-mode load.
The material was assumed to be homogeneous, isotropic with linear elastic behavior. The considered elastic properties were $E = 210$ GPa and $\nu = 0.3$.
The accuracy of the methodologies implemented in the software Abaqus, namely the maximum energy release rate (MERR) and the maximum tangential stress (MTS), and the virtual crack closure technique (VCCT) [73] was checked by comparison with Eq. 6.5 and Eq. 6.6 for a straight crack with a ratio $a/W = 0.55$ and for the loading device possible loading angles.
Quadrilateral isoparametric elements with eight nodes were used (CPS8). However, for the VCCT technique quadrilateral isoparametric elements with four nodes (CPS4) were also used in this comparison.
Singular elements with nodes at quarter-point positions were considered at the crack tip.
The used mesh is shown in Figure 6.10.

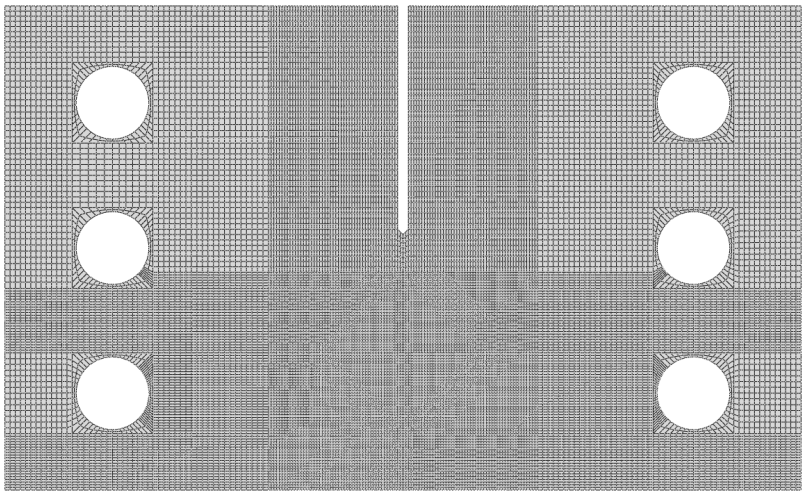

Figure 6.10: CTS90 specimens finite element mesh used for K_I and K_{II} determination techniques validation.

The obtained results are shown in Figure 6.11 and Figure 6.12. These results show the high accuracy of all methodologies used to calculate the mode I stress intensity factor (K_I). However, the VCCT technique presents the major difference relatively to the mode II stress intensity factor (K_{II}) numerical solution namely when CPS8 elements are used. Since the methodologies implemented in the software Abaqus showed high accuracy in the calculation of mode I and mode II stress intensity factor and are easy to be applied they will be used in the process to calculate the K_I and K_{II} factors from the experimental tests.

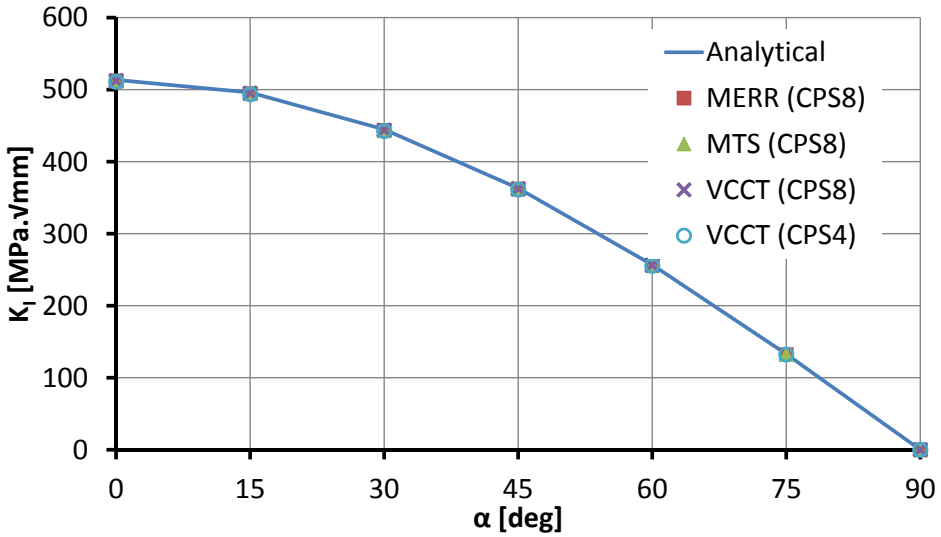

Figure 6.11: Comparison of K_I obtained with different methodologies.

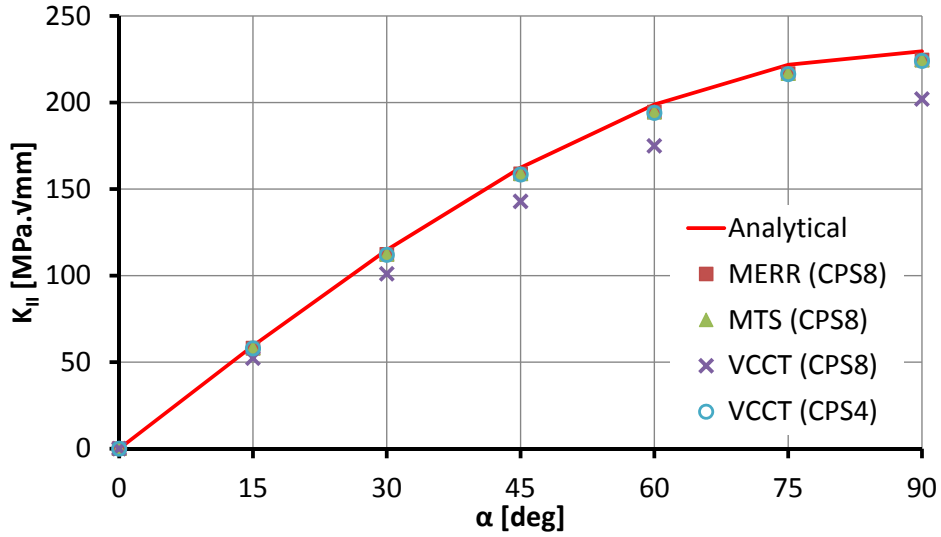

Figure 6.12: Comparison of K_{II} obtained with different methodologies.

Considering the previous results, three different finite element models, one for each tested specimen, were built to calculate the K_I and K_{II} stress intensity factors for the experimental crack propagation. Figure 6.13, Figure 6.14 and Figure 6.15 shows the built meshes and also a detail of the crack mesh. Note that the crack is open because the maximum load is applied to easily identify the crack path.

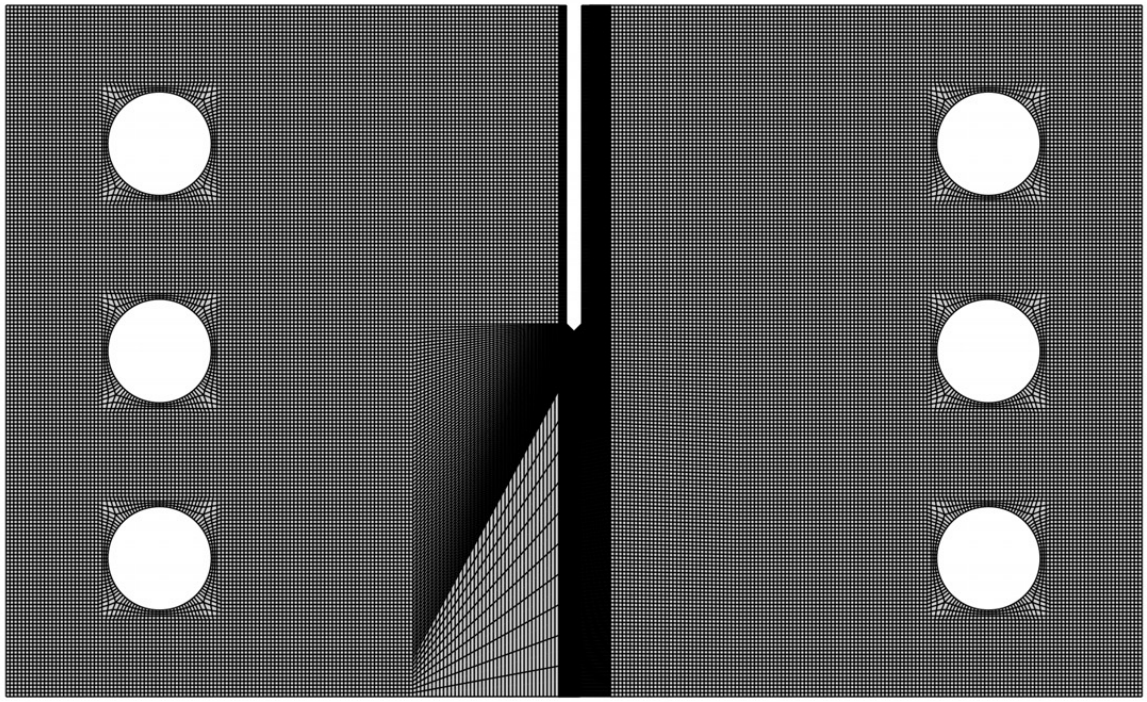

(a) Complete mesh with 221606 nodes and 73115 CPS8 elements

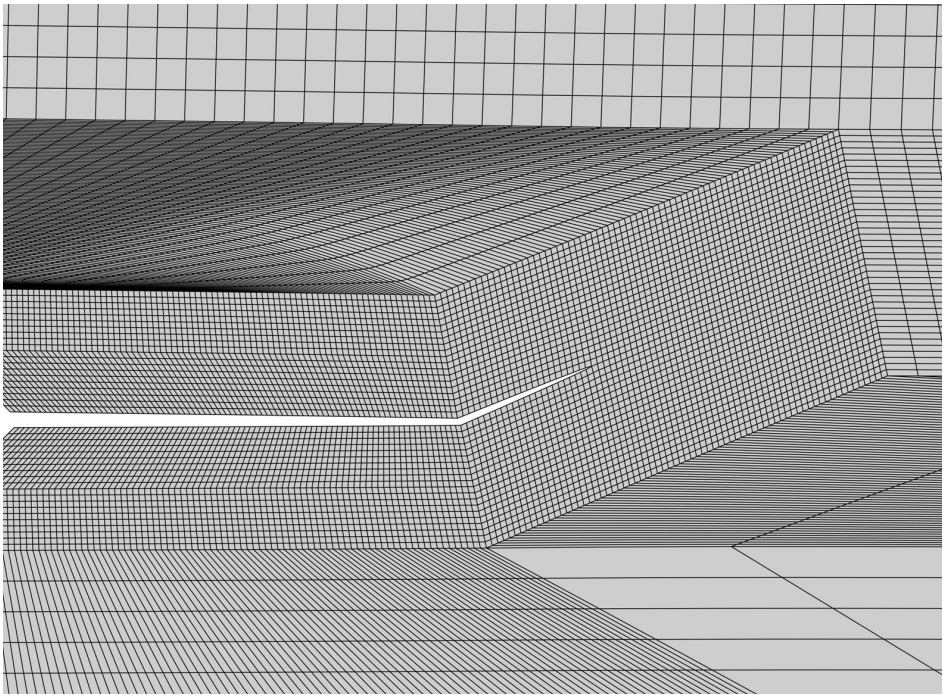

(b) Crack mesh detail.

Figure 6.13: CTS90 specimens finite element mesh used for experimental K_I and K_{II} determination with $\alpha = 30º$.

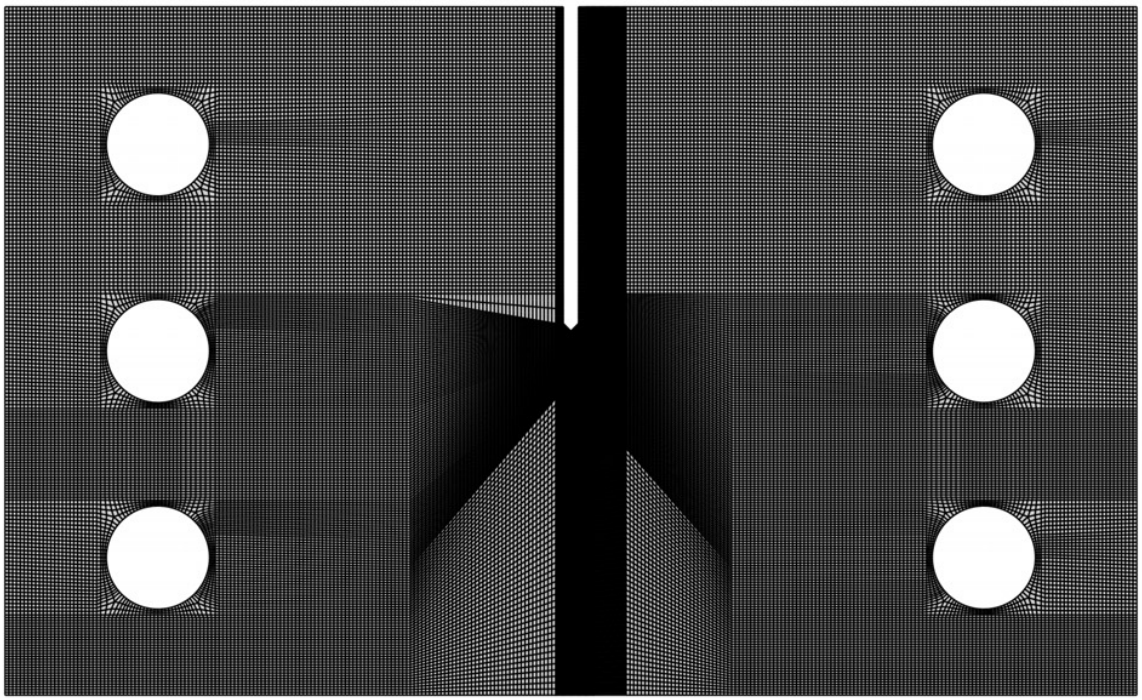

(a) Complete mesh with 266112 nodes and 87943 CPS8 elements

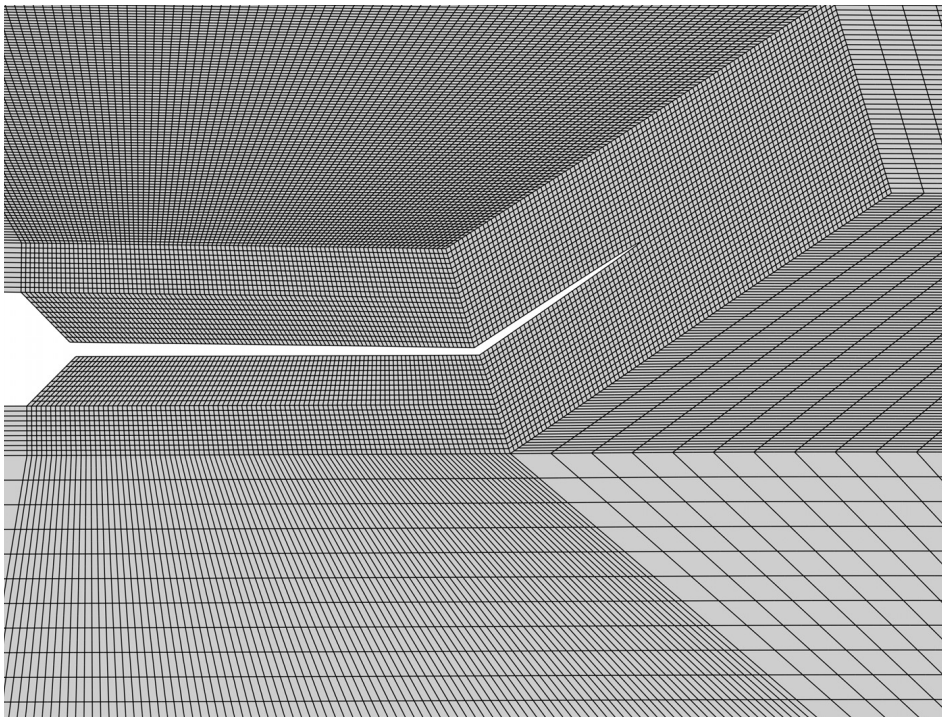

(b) Crack mesh detail.

Figure 6.14: CTS90 specimens finite element mesh used for experimental K_I and K_{II} determination with $\alpha = 45$º.

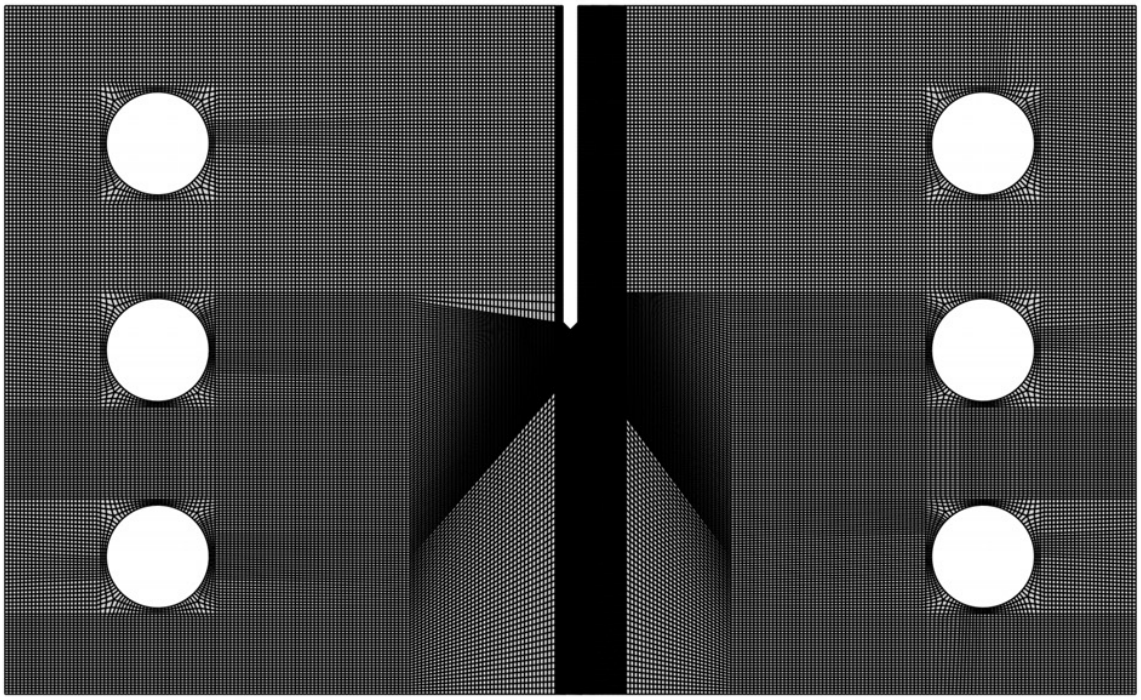

(a) Complete mesh with 246888 nodes and 81559 CPS8 elements

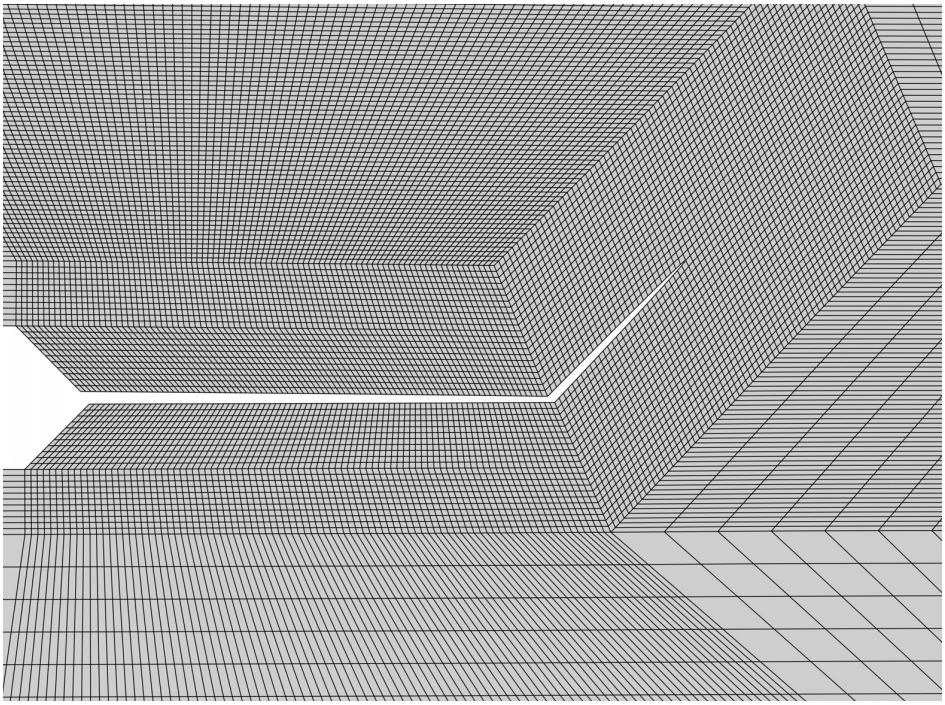

(b) Crack mesh detail.

Figure 6.15: CTS90 specimens finite element mesh used for experimental K_I and K_{II} determination with $\alpha = 60º$.

6.4 Experimental results

Table 6.1 shows the pre-crack length for each tested specimen, as well as the a_0/W ratio, the load $R-ratio$ (applied during pre-crack and mixed mode test), the applied load range during the test and the corresponding mode I and mode II stress intensity factors installed at the crack tip at the beginning of the mixed mode tests, calculated using the equations 6.5 and 6.6.

Table 6.1: Applied conditions after pre-cracking.

CTS#	α	a_0[mm]	a_0/W	R	$\triangle F$ [N]	$\triangle K_I$ [MPa mm$^{1/2}$]	$\triangle K_{II}$ [MPa mm$^{1/2}$]
1	30º	49.73	0.55	0.1	8820	396.9	101.7
2	45º	50.60	0.56	0.1	9216	353.7	153.9
3	60º	49.56	0.55	0.1	10557	271.8	210.6

The crack propagation path in mixed mode was measured using a microscope equipped with two micrometers, and these measurements are shown in Figure 6.16. Note that a1' and a2' are the CTS front and back crack paths, and a_x is the horizontal crack length and a_y the vertical crack length.

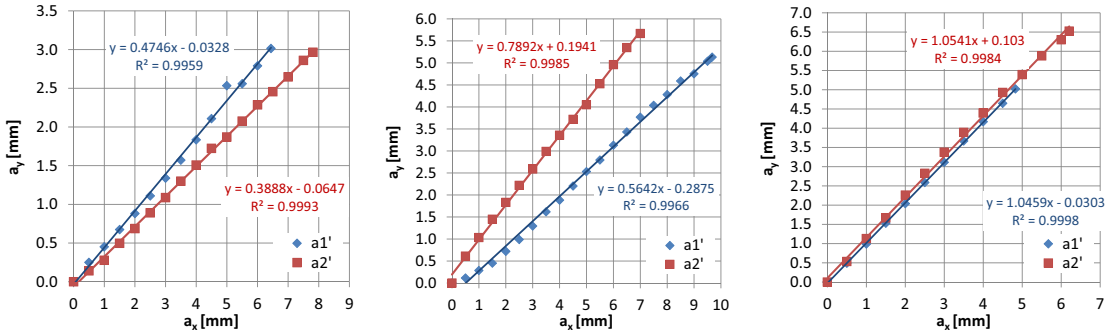

(a) Loading angle $\alpha = 30$º (b) Loading angle $\alpha = 45$º (c) Loading angle $\alpha = 60$º

Figure 6.16: Microscope measured crack paths under mixed mode loading.

To calculate the crack propagation angle (β) the slope of the linear regression made to measured points (m) was used as:

$$\beta = \arctan(m) \tag{6.12}$$

The obtained linear regression slops for each side of the specimens and the corresponding crack propagation angles are listed in Table 6.2.

Table 6.2: Experimental crack propagation angle β

α	m_1	m_2	β_1	β_2
30º	0.4746	0.3888	25.39º	21.25º
45º	0.5642	0.7892	29.43º	38.28º
60º	1.0459	1.0541	46.29º	46.51º

The experimental crack components x and y for the tested loading angles, shown in Figure 6.17, were calculated using the technique described at the end of section 6.2.

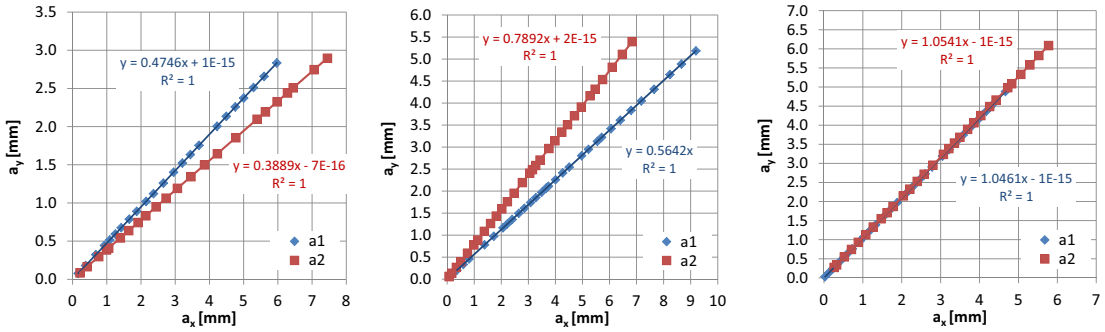

(a) Loading angle $\alpha = 30º$ (b) Loading angle $\alpha = 45º$ (c) Loading angle $\alpha = 60º$

Figure 6.17: Experimental calculated crack paths under mixed mode loading.

From the results presented in Figure 6.17, the fatigue crack growth rates in mixed mode were calculated using the secant method as:

$$\frac{da}{dN} = \frac{a_{i+1} - a_i}{N_{i+1} - N_i} \tag{6.13}$$

where $a = \sqrt{a_x^2 + a_y^2}$ is the average crack length, from a_1, front side crack of the specimens and a_2, back side crack of the specimen, and N the number of cycles.
For every experimentally measured point the corresponding K_I and K_{II} factors were calculated using the described finite element models and the Richard/Henn [66, 67] criterion was used to calculate the equivalent stress intensity factor (K_V), see Eq. 6.4.
The mixed mode fatigue crack growth rates obtained are graphically shown in Figure 6.18 as $da/dN = f(\triangle K_V)$.

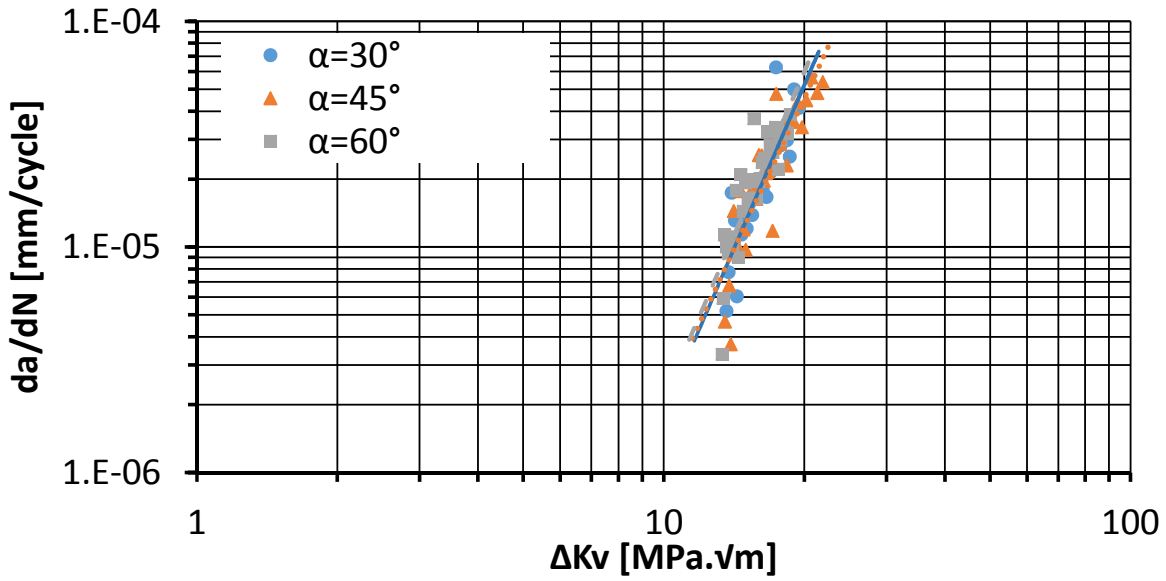

Figure 6.18: Mixed-mode fatigue crack growth rates.

The obtained Paris law constants, C and m, for mixed mode loading were obtained by fitting the results using a power function as:

$$\frac{da}{dN} = C\left(\triangle K_V\right)^m \tag{6.14}$$

These constants, including the R^2, for the tested loading angles are listed in Table 6.3.

Table 6.3: Paris law constants for the mixed mode loading.

α	C	m	R^2
30º	2.87E-11	4.81	0.748
45º	7.49E-11	4.45	0.765
60º	3.24E-11	4.82	0.739

Figure 6.19 shows a comparison between the obtained mixed mode fatigue crack growth with the mode I fatigue crack growth rates obtained and previously presented in this thesis.

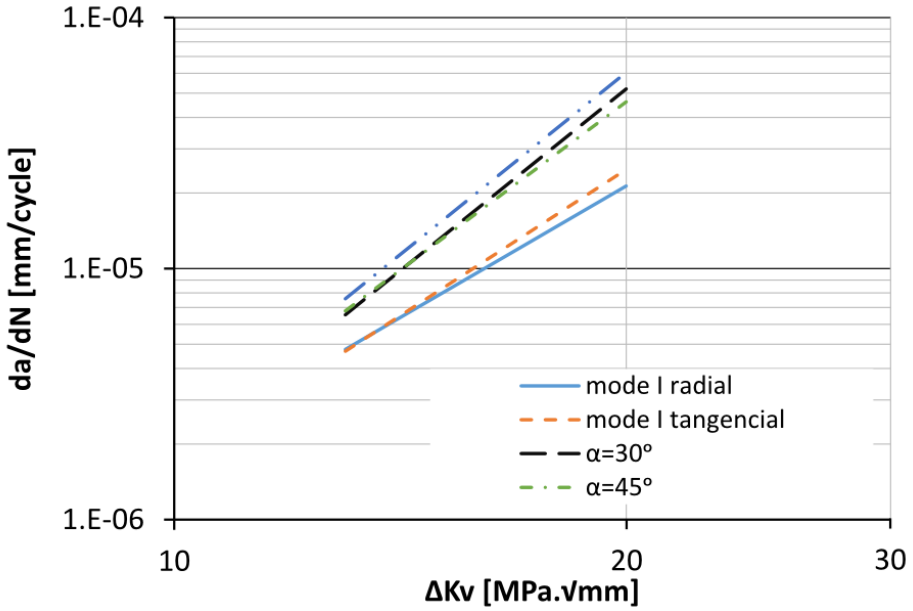

Figure 6.19: Comparison between the mixed mode fatigue crack growth with the mode I fatigue crack growth rates obtained.

Table 6.4 shows a comparison between the experimentally measured and numerically calculated crack propagation angle (β) for the tested mixed mode loading conditions (α).
The numerical crack propagation angle was calculated using the Broek equation as [74]:

$$K_I \sin\beta + K_{II}\left(3\cos\beta - 1\right) = 0 \tag{6.15}$$

To apply this equation the K_I and K_{II} factors were calculated using the Eq. 6.5 and Eq. 6.6 respectively.

Table 6.4: Crack propagation angle (β) obtained with different methods.

α		30º	45º	60º
numerical		26º	37º	49º
ABAQUS	MERR	26º	38º	51º
	MTS	25º	36º	48º
experimental		23º	34º	46º

The considered experimental propagation angle is the average of β_1 and β_2.

6.5 Concluding remarks

Fatigue crack growth rates and the propagation angle were evaluated under mixed-mode (mode-I and mode-II) conditions on Compact Tension Shear (CTS) specimens taken from a

Spanish AVE train wheel.
The used apparatus was based on the mixed-mode testing technique proposed by Richard [62] that allows to perform mixed-mode loading using a uniaxial testing machine just by changing the loading angle between the longitudinal axis of the specimen and the load direction applied by the testing machine.
Three different loading angles were tested 30º, 45º and 60º.
Since no numerical solution exists to calculate the K_I and K_{II} values a finite element analysis was also done in order to obtain them for the tested conditions.
It was observed that the fatigue crack growth direction changed immediately from the initial fatigue mode-I pre-crack orientation when load direction was changed.
The experimental growth direction of the cracks for different load mixities were compared with the predictions based on numerical approaches (ABAQUS and Broek equation) which provide a similar estimation of the crack growth direction and a good agreement with the experimental results.
It was observed that for the tested $\triangle K$ range the mixed mode fatigue crack growth rates are higher than the mode I fatigue crack growth rates. However, observing the results presented in Figure 6.19, for lower $\triangle K$ values or near the threshold the mixed mode fatigue crack growth rates could be lower than the mode I fatigue crack growths.

Chapter 7

Striation spacing measurements

Striation spacing measurements were performed in four different C(T) specimens, two taken from an AVE wheel and the other two from a UIC60 rail, which were used in fatigue crack growth rates tests. During these measurements it was observed that the striations have a random orientation. No striation spacing (*s*) vs. fatigue crack growth rates (da/dN) correlation was found, but values of s were approximately constant for lower $\triangle K$ values, whereas for higher values of $\triangle K$ striation spacing values are similar to *da/dN* values.

7.1 Introduction

During the fatigue crack growth process the formation of some periodic markings on the fatigue surface was observed. In order to characterize these markings the fatigue surface was observed on a scanning electron microscope (SEM) and striations were identified.
The striation formation process, during fatigue crack growth, is being an object of study, *e.g.* [75], since striations can help the study of rupture cases. If there is a relation between striation spacing and fatigue crack growth, measurements of striation spacing may help to evaluate the magnitude of the load acting during rupture. These studies can help to perform failure analysis and, generally, to contribute to the safety of structures and machine elements..

7.2 Experimental work

Specimens

In this study four different compact tension specimens, C(T), were analyzed, two of them were taken from a Spanish high speed train (AVE) wheel and other two from a UIC60 rail. These specimens were previously subjected to fatigue crack growth rates (FCGR) tests according to the standard ASTM E647. Some data from these FCGR tests are presented in Table 7.1.

Table 7.1: Fatigue crack growth rates experimental data.

Specimen	material	△P [N]	a_0[mm]	R
RR2	wheel	9090	10.15	0.1
RR4		9000	10.16	0.4
CN2	rail	8100	10.15	0.1
CN4		6000	10.19	0.4

At the end of FCGR tests the fatigue crack was propagated until the specimen becomes divided in two parts. These specimen halves were then used to observe the fatigue surfaces. Figure 7.1 shows the geometry of the specimen halves.

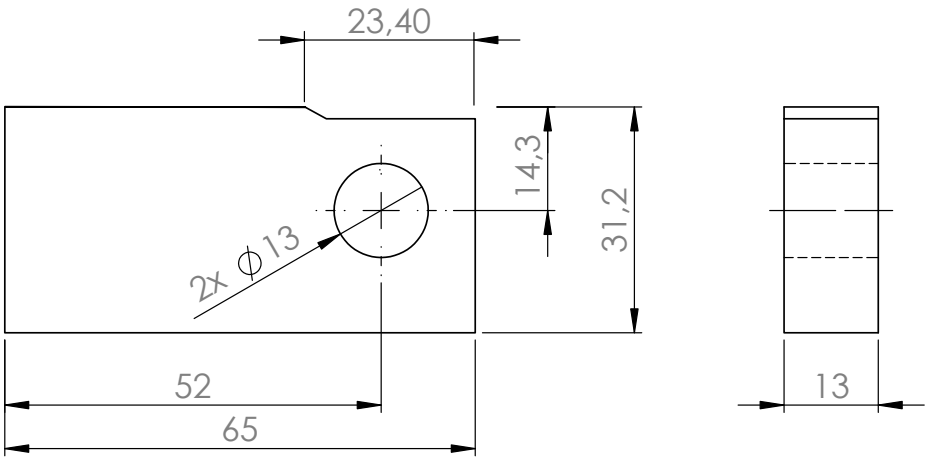

Figure 7.1: C(T) specimens' sample dimensions.

In order to allow better observation of the fatigue surfaces the four specimens were cleaned with ultrasounds using an alcohol bath.

Scanning Electron Microscope observations

All observations were performed at the Materials Center of the University of Porto (CEMUP) using a high resolution Scanning Electron Microscope (SEM) FEI Quanta 400 FEG ESEM \ EDAX Genesis X4M with X-Ray microanalyses and backscattered electron diffraction pattern analysis: FEG-ESEM \ EDS \ EBSD, shown in Figure 7.2.

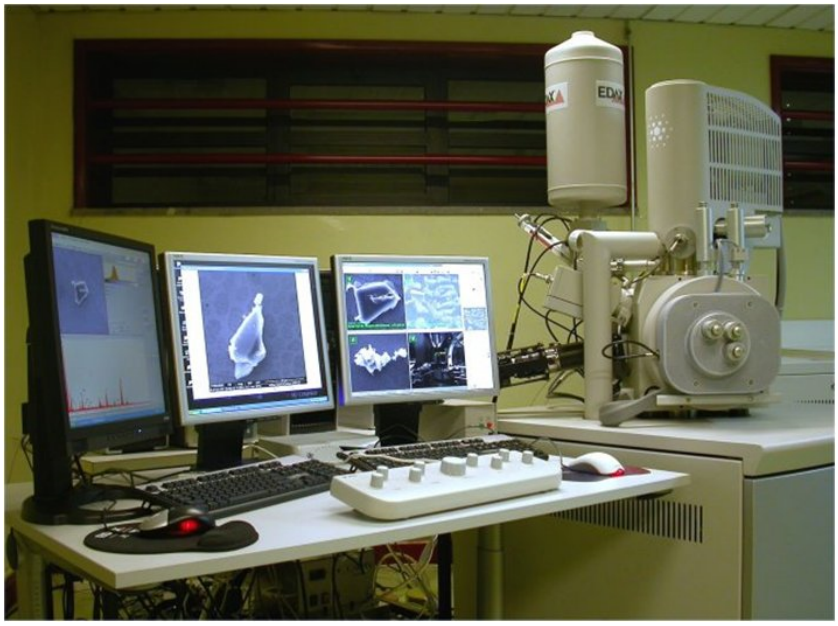

Figure 7.2: CEMUP Scanning Electron Microscope.

At the beginning of every specimen fatigue surface observation the location of a reference point located at the end of the EDM notch was recorded, as shown in Figure 7.3. This was possible because the EDM notch has a different topography from the fatigue crack. The obtained reference coordinates were used to calculate the fatigue crack length for any taken picture and then correlate striation spacing measured with the fatigue crack growth rates previously recorded.

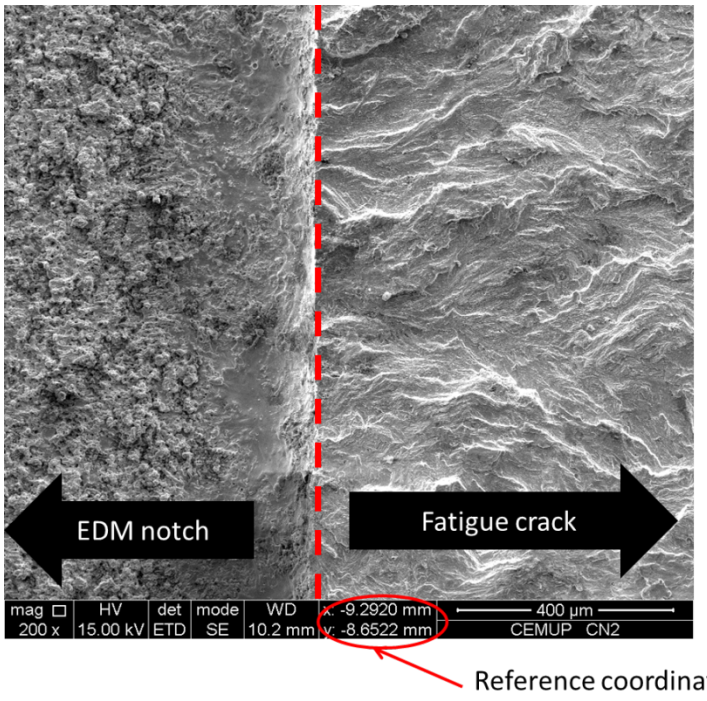

Figure 7.3: Specimen reference point

The location of all measurements shown in Figure 7.4.

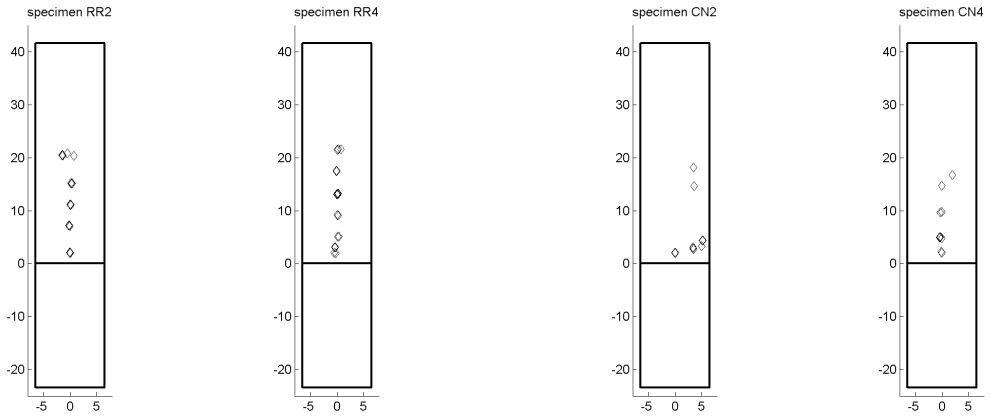

Figure 7.4: Measured points' location.

The randomness of fatigue striations orientation is strongly emphasized in Figure 7.5 were a picture taken from the fatigue surface of specimen CN2 is shown.

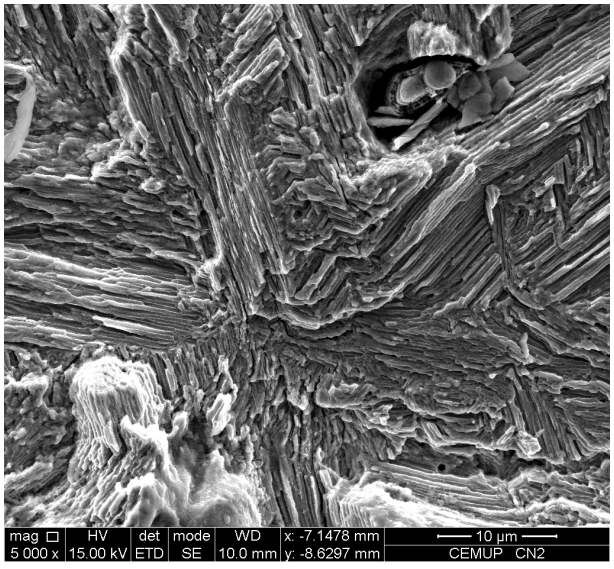

Figure 7.5: CN2 specimen fatigue surface striations.

Figure 7.6 shows some pictures taken along the observed specimen surface where different topographies can be identified. It can be observed the randomness of striation orientation on the fatigue crack.7.6

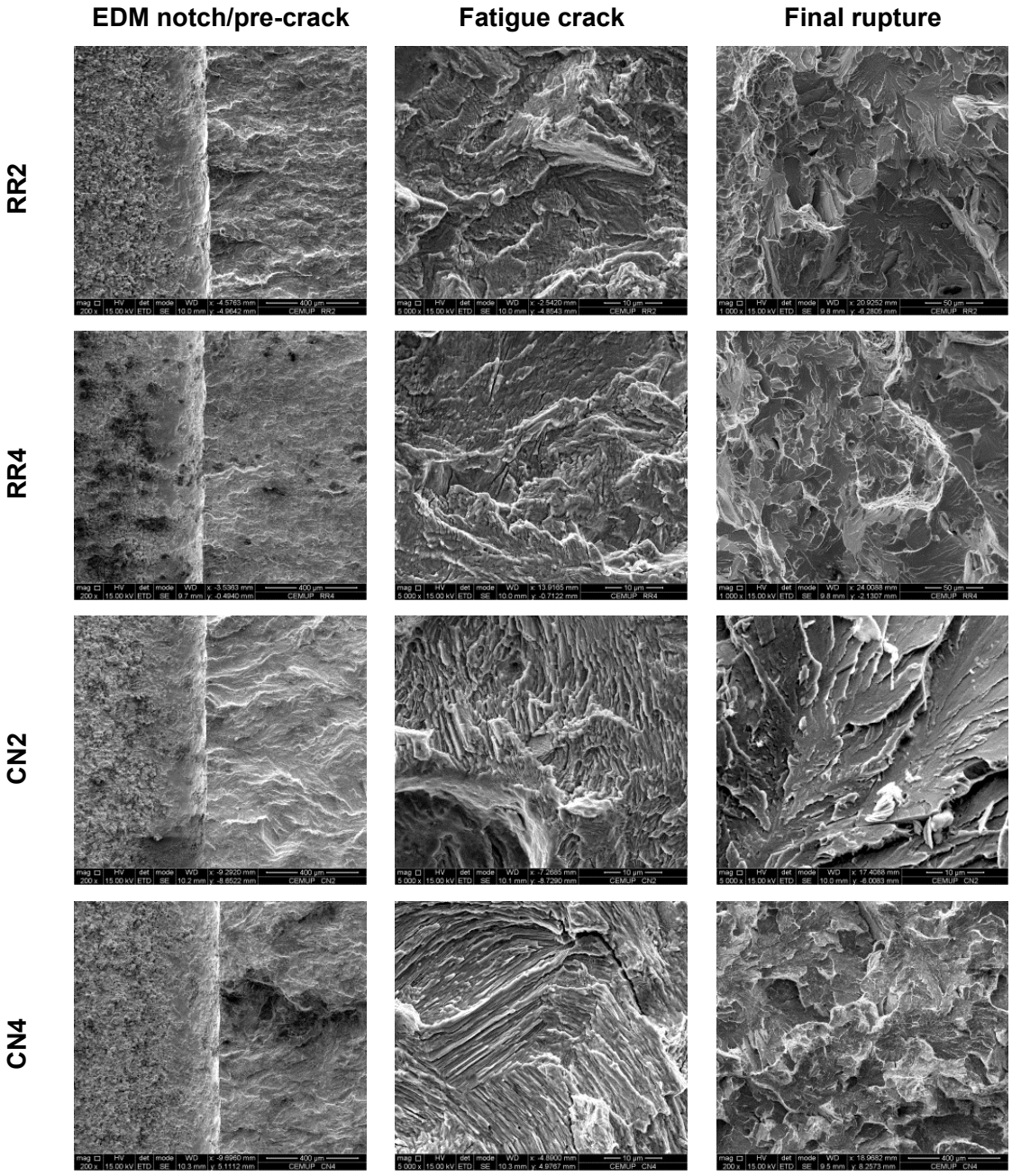

Figure 7.6: Differences between surfaces along specimens' length.

Striation spacing measurements

During the SEM observations several pictures were taken in locations were striations can be identified. Striation spacing was evaluated drawing lines perpendicular to striations, as shown in Figure 7.7, and its length was divided by the number of striations.

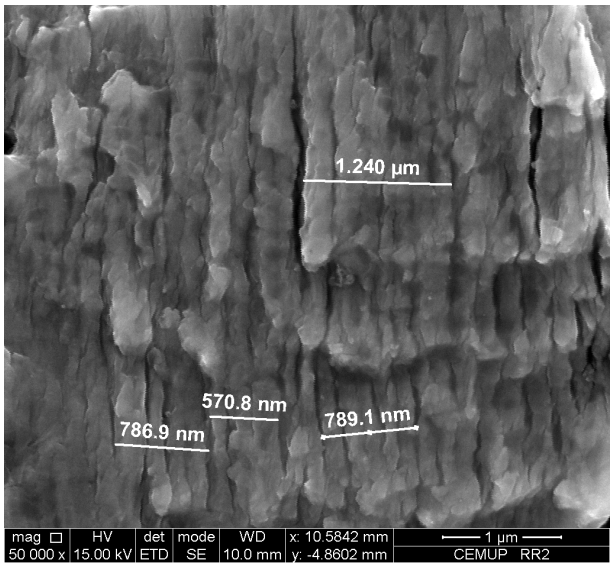

Figure 7.7: Striation spacing measurements.

7.3 Experimental results

One of the aims of this study is to verify if a correlation between the fatigue crack growth rate and striation spacing is found. Another objective is to identify possible similitudes or differences in the observed behavior of wheel and rail materials, and finally to compare this with results published in the literature for steels. Figure 7.8 shows the obtained average striation spacing values for different crack lengths and the location of the measured points.

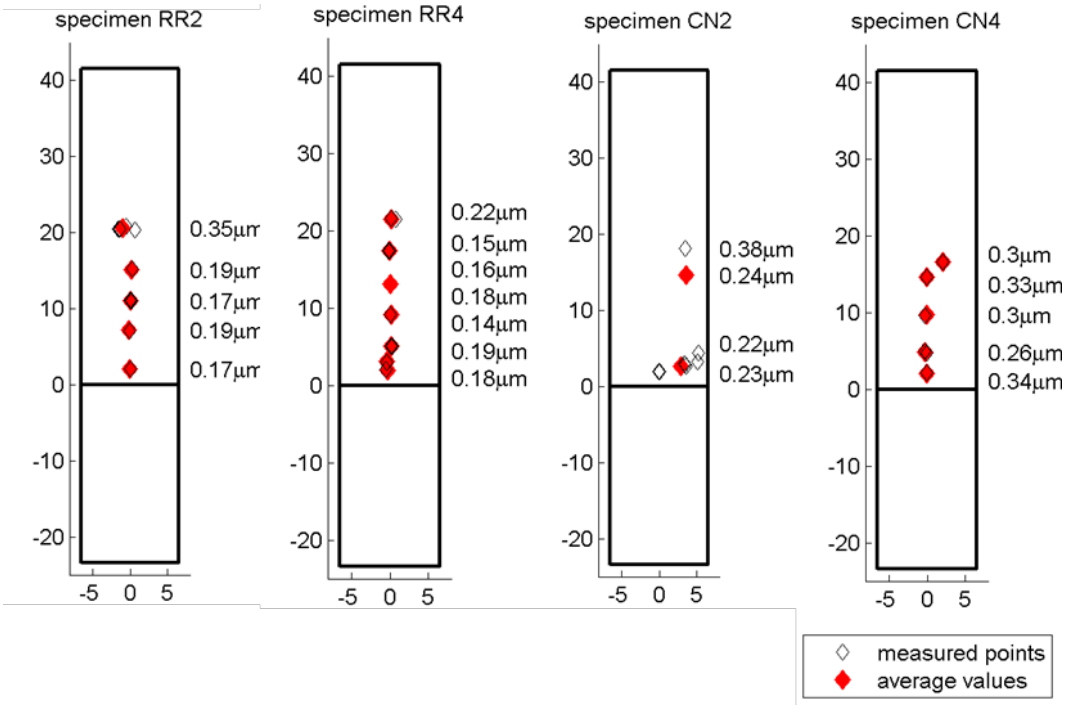

Figure 7.8: Measured points' location and striation spacing average values.

A summary of the obtained striation spacing average values for all specimens is shown as a function fatigue crack growth rates in Figure 7.9.

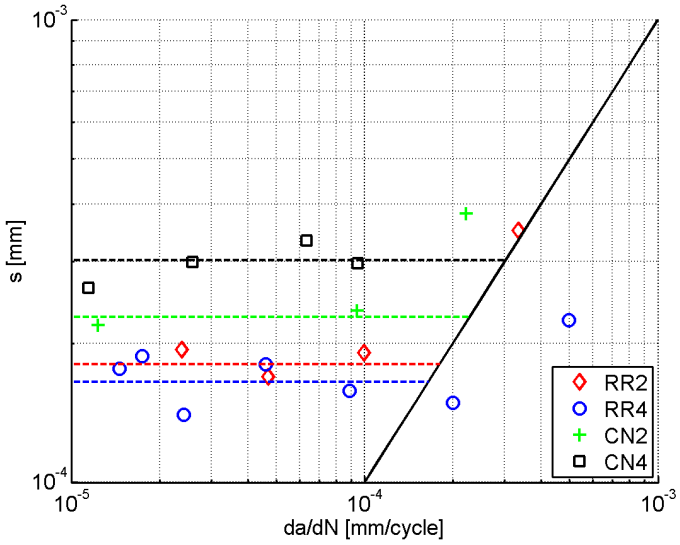

Figure 7.9: Striation spacing *vs.* fatigue crack growth rates average values obtained for all studied specimens.

The Figure 7.9 suggests that striation spacing for the rail material is higher than for wheel material. Furthermore, in the case of rail material s increases with R, an effect not found in the wheel steel. Striation spacing was found to be approximately constant for values of *da/dN* between approximately10^{-5} and 10^{-4} mm/cycle. No striation spacing *vs. da/dN* correlation was found, as in other studies, *e.g.* [76].

7.4 Concluding remarks

Striation spacing measurements were performed in four different C(T) specimens, taken from an AVE wheel and UIC60 rail, which were previously used in fatigue crack growth rates tests. These measurements revealed that there is no correlation between fatigue crack growth and striation spacing and the striation orientation is randomness without any relation to the fatigue crack propagation direction.

Part II

NUMERICAL WORK

Chapter 8

Wheel/rail 2D fatigue crack propagation simulation

This work attempts to model a wheel's subsurface crack propagation under RCF with particular attention dedicated to the propagation direction of the crack at every increment of its length.
Considering the results and numerical methodology's validated by the experimental work on the mixed mode fatigue crack propagation, presented before, the Maximum Tangential Stress (MTS) [71] criterion was used to calculate the mode I and II stress intensity factors and the crack propagation direction along the crack tips loading cycle.
The commercial finite element package Abaqus was used to build and analyze the model.
As rolling contact induces complex non-proportional mixed-mode conditions at crack tips, the evolution of mode I and mode II stress intensity factors was followed along the loading cycle.
It can be assumed that the crack is far enough to be out of the near surface layer that is heavily plastically deformed by rolling contact. According to this, linear elastic fracture mechanics concepts can be considered and the crack propagation can be analyzed under these assumptions [77].

8.1 Finite element model

The commercial finite element package ABAQUS 6.12-3 [72] was used to build and analyze the 2D model.
To improve the performance of the simulation, it was decided to build a different part were the crack will growth and were the mesh is more refined apart from wheel model and then this part was "tied" to the wheel. This construction is shown in Figure 8.1.

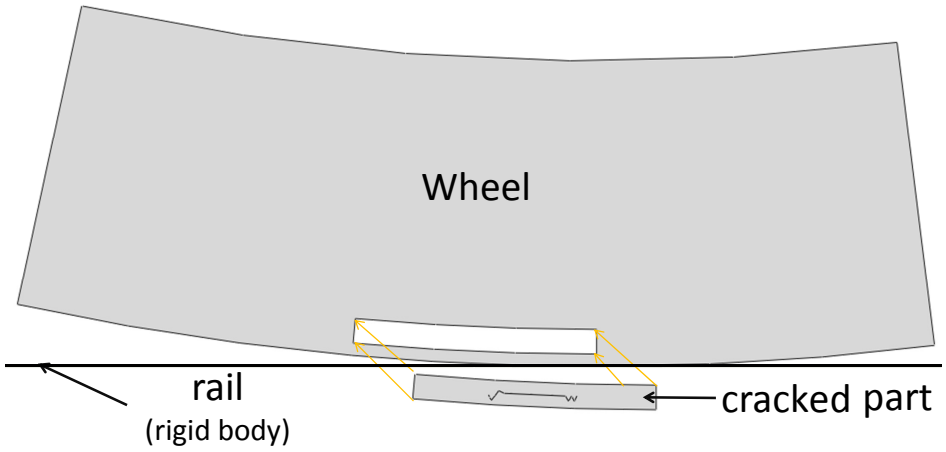

Figure 8.1: Finite element model construction.

Plane strain quadrilateral with 8-node elements (CPE8) were used to build a 2D finite element mesh of the wheel. Since the objective of this work is to simulate the propagation of a subsurface crack in the wheel, the rail was modeled as a rigid line.

Singular elements with nodes at quarter-point positions were considered at the crack tip. As the crack will be loaded in compression it was necessary to use self-contact formulations to avoid interpenetration of the crack faces node. In this study the penalty method was considered as contact enforcement in the crack faces contact.

No hydrodynamic or entrapment fluid effect or interfacial crack friction was considered between crack faces.

As boundary conditions, the rail was fixed and the wheel was loaded against the rail by a vertical force of 11.5 kN and translated 40 mm in small increments. This translation associated with the friction force generated by the friction makes the wheel to turn around its geometric center that is free to rotate.

The penalty method was also used has contact enforcement on the contact between the wheel and the rail and a friction coefficient of 0.1 was considered.

The material was assumed to be homogeneous, isotropic with linear elastic behavior. The elastic properties considered were $E = 210$ GPa and $\nu = 0.3$.

8.2 Methodologies

Since the finite element model have a great local transition on the mesh refinement between the wheel and crack parts, it was decided to perform an analysis of the contact stresses distribution on an un-cracked model to verify if that transition has any important influence on the stress field. In Figure 8.2 the un-cracked model finite element mesh is shown and the obtained Tresca and minimum stress fields are shown in Figure 8.3 and Figure 8.4 respectively, where no influence of the great local transition on the mesh refinement is observed.

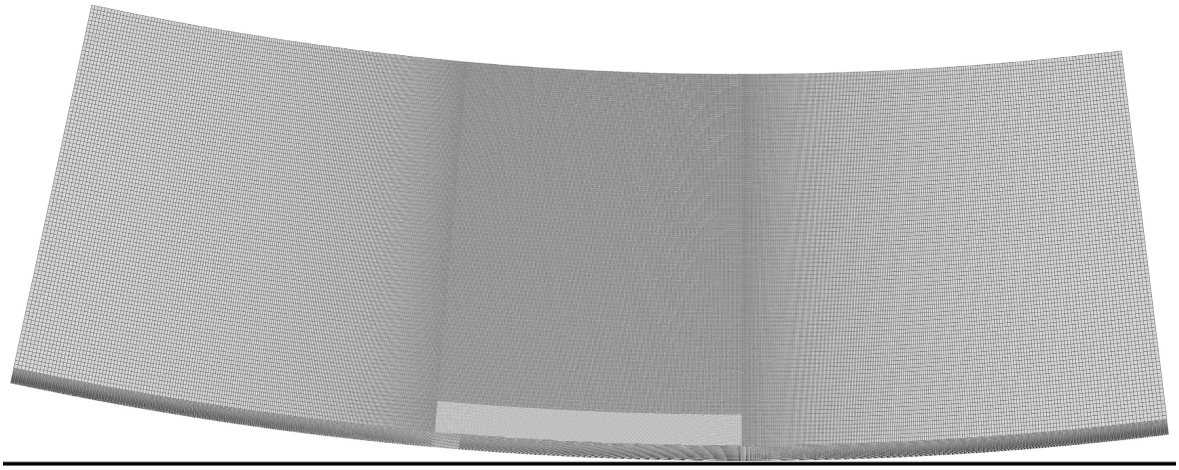

Figure 8.2: Un-cracked model mesh build with 841009 nodes and 278474 quadratic quadrilateral elements of type CPE8.

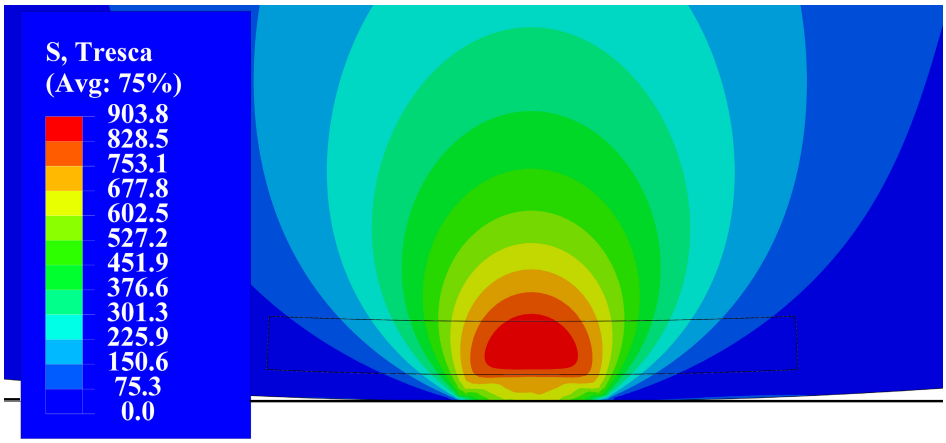

Figure 8.3: Un-cracked model τ_{Tresca} field on the wheel in [MPa].

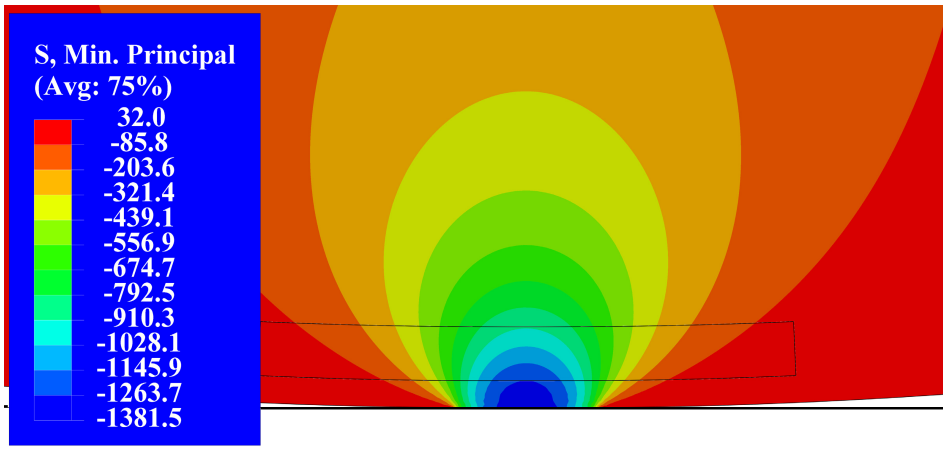

Figure 8.4: Un-cracked model $\sigma_{min} = P_0$ field on the wheel in [MPa].

Table 8.1 shows some variables as the applied normal force (F_N), the considered friction coefficient (μ). Other variables obtained with the un-cracked model are also listed as the

maximum Hertz pressure (P_0), the contact width ($a_{contact}$), the maximum value of the Tresca stress ($\tau_{Tresca\,max}$) and the depth at it occurs (Z_s).

Table 8.1: Un-cracked model results.

F_N [kN]	μ	P_0 [GPa]	$a_{conatct}$ [mm]	Tresca criterion	
				Z_S [mm]	$\tau_{Tresca\,max}$ [MPa]
11.5	0.10	1.39	5.52	3.98	905.10

The depth at the maximum value of the Tresca stress occurs (Z_s) is an important variable for this work, as the initial crack was positioned at that depth.
From the un-cracked model, the same applied load and the friction coefficient were used in the cracked model to guarantee the same contact conditions.
The initial crack has 10 mm in length and is located at the depth of the maximum value of the Tresca stress, in this case at 4 mm.
At every increment each crack tip was analyzed independently, and the crack length was increased 1mm, at each crack tip, in the direction of the calculated maximum mixed mode equivalent stress intensity factor along the load cycle, observed at the correspondent crack tip.
The maximum tangential stress criterion, available in the software ABAQUS, was used to calculate the mode I and mode II stress intensity factors as the direction of the crack propagation.
For homogeneous, isotropic elastic materials the direction of cracking propagation can be calculated using the maximum tangential stress criterion as [72]:

$$\theta = \cos^{-1}\left(\frac{3K_{II}^2 + \sqrt{K4_I^2 + 8K_I^2K_{II}^2}}{K_I^2 + 9K_{II}^2}\right) \tag{8.1}$$

The Richard/Henn [66, 67] criterion was considered to calculate the equivalent stress intensity factor (K_V), as:

$$K_V = \frac{K_I}{2} + \frac{1}{2}\sqrt{K_I^2 + 6K_{II}^2} \tag{8.2}$$

It was defined that the process of increasing the crack will be repeated until the maximum mixed mode equivalent stress intensity factor reaches the threshold or reaches a value that can be considered that is within the unstable crack propagation zone.

8.3 Results

As results, in the next paragraphs the obtained crack path and the evolution of the stress intensity factor will be shown in Figures 8.5 to 8.11. In Table 8.2 the obtained crack propa-

gation angles are listed. This angles are measured relatively to the horizontal plane.
In this case the calculation process ended when the maximum mixed mode equivalent stress intensity factor reached a value considered in the unstable propagation zone, see Figure 8.11, which implies that the crack will growth rapidly until reaches the wheel surface, in this case, considering the propagation angle the crack will reach the wheel tread.
In Figure 8.12 the maximum value of K_V recorded for each crack length is represented in function of the crack length.

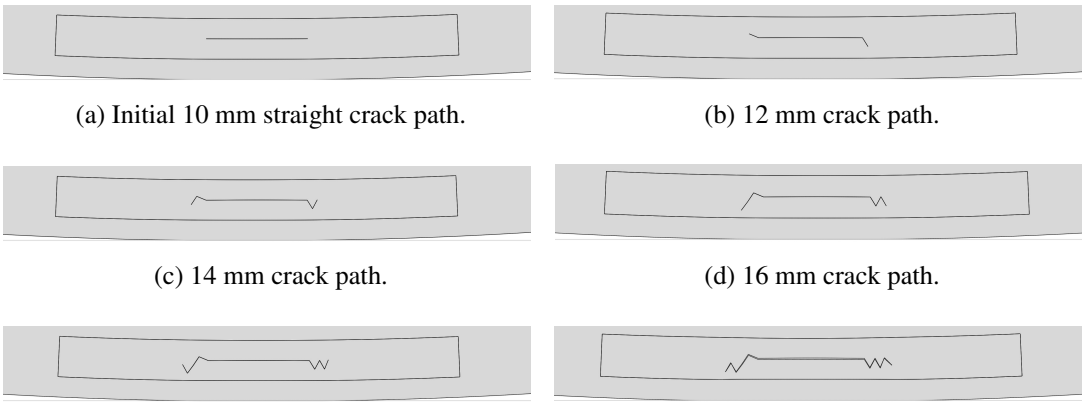

(a) Initial 10 mm straight crack path.

(b) 12 mm crack path.

(c) 14 mm crack path.

(d) 16 mm crack path.

(e) 18 mm crack path.

(f) 20 mm crack path.

Figure 8.5: Wheel crack propagation path.

Table 8.2: Wheel crack propagation angles.

crack length [mm]	left crack tip angle [deg]	right crack tip angle [deg]
10	67	-58
12	-58	62
14	-53	-60
16	61	68
18	-58	-43
20	-54	59

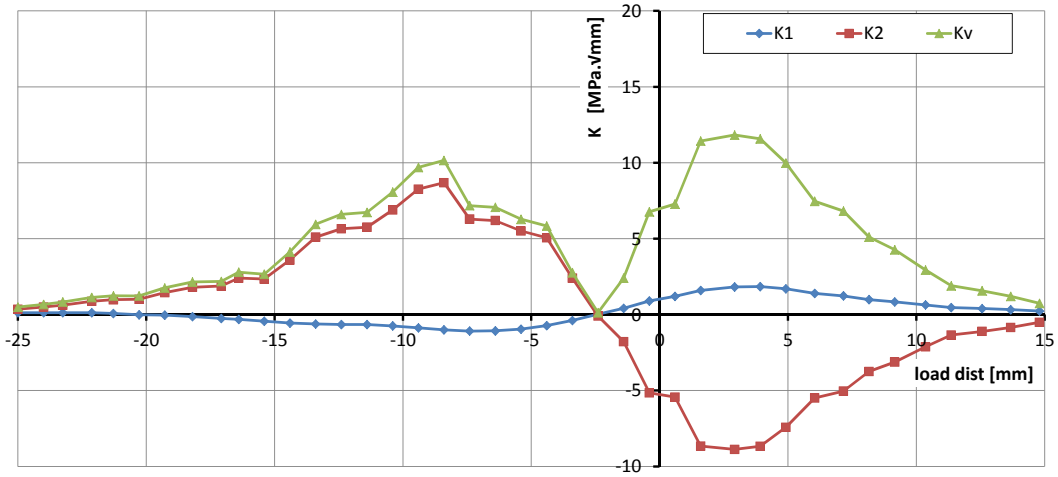

(a) Left crack tip K_I, K_{II} and K_V evolution.

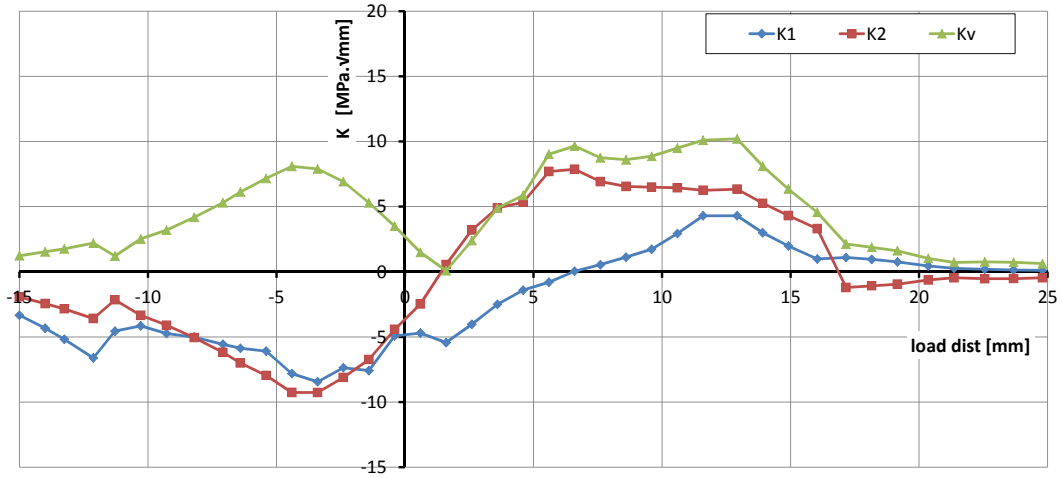

(b) Right crack tip K_I, K_{II} and K_V evolution.

Figure 8.6: Stress intensity factors evolution during load passage on the initial straight 10 mm crack.

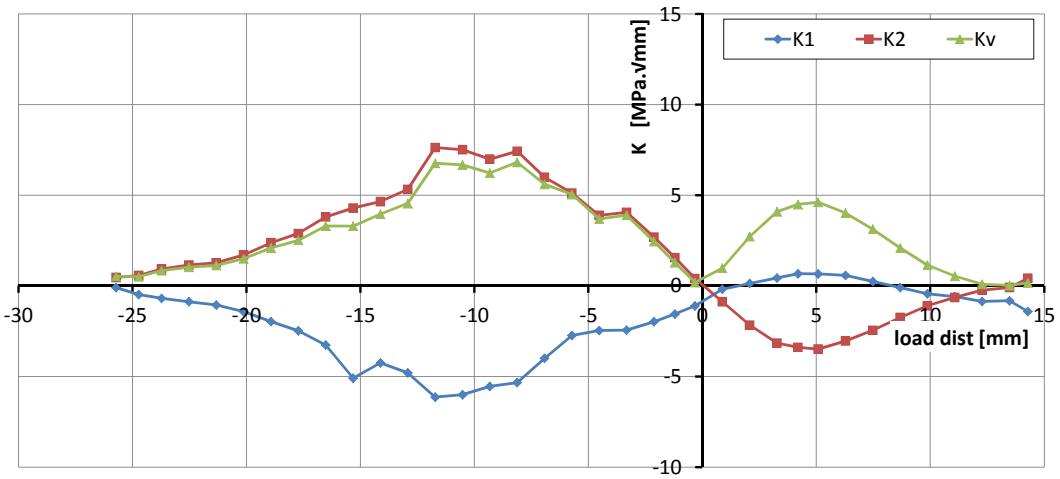

(a) Left crack tip K_I, K_{II} and K_V evolution.

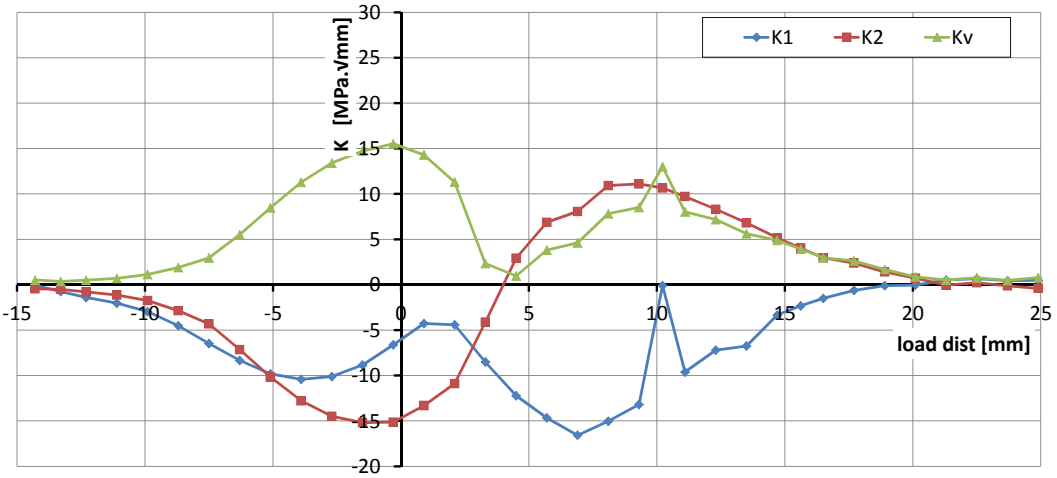

(b) Right crack tip K_I, K_{II} and K_V evolution.

Figure 8.7: Stress intensity factors evolution during load passage on the 12 mm crack.

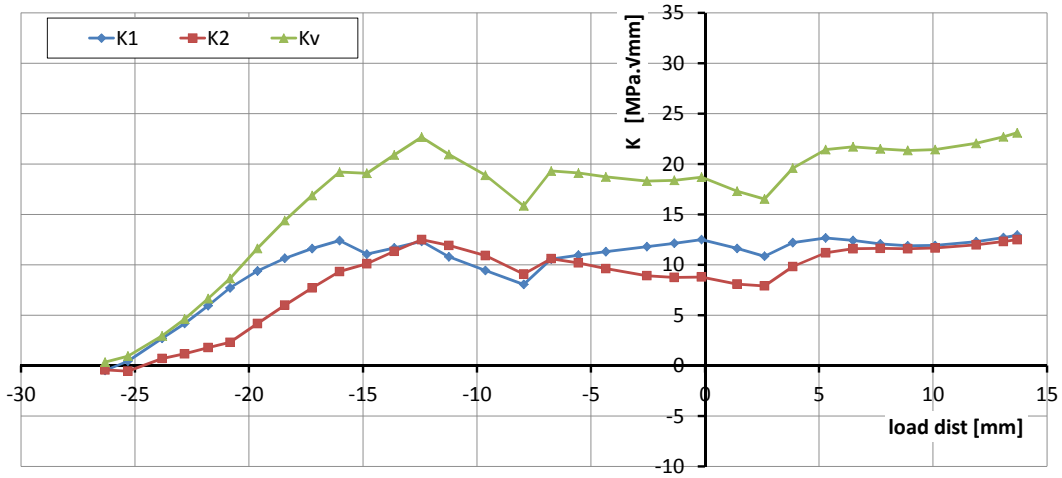

(a) Left crack tip K_I, K_{II} and K_V evolution.

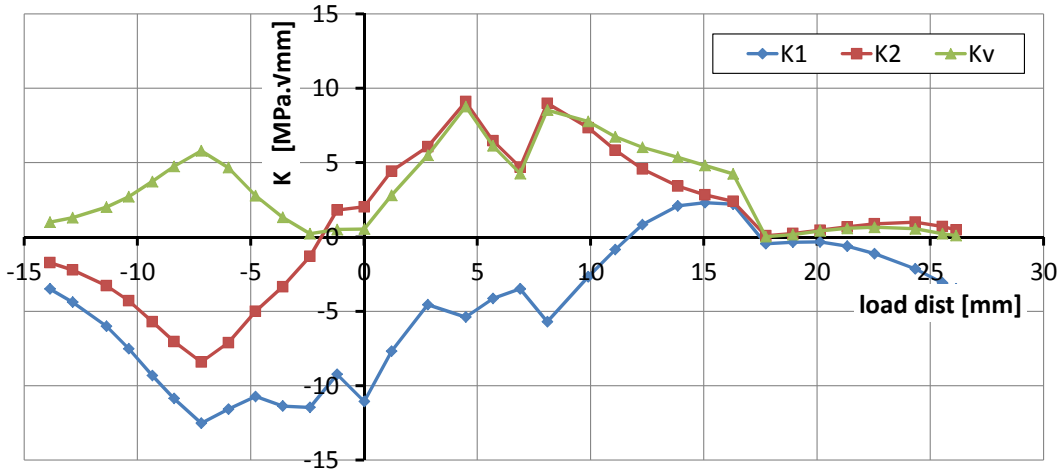

(b) Right crack tip K_I, K_{II} and K_V evolution.

Figure 8.8: Stress intensity factors evolution during load passage on the 14 mm crack.

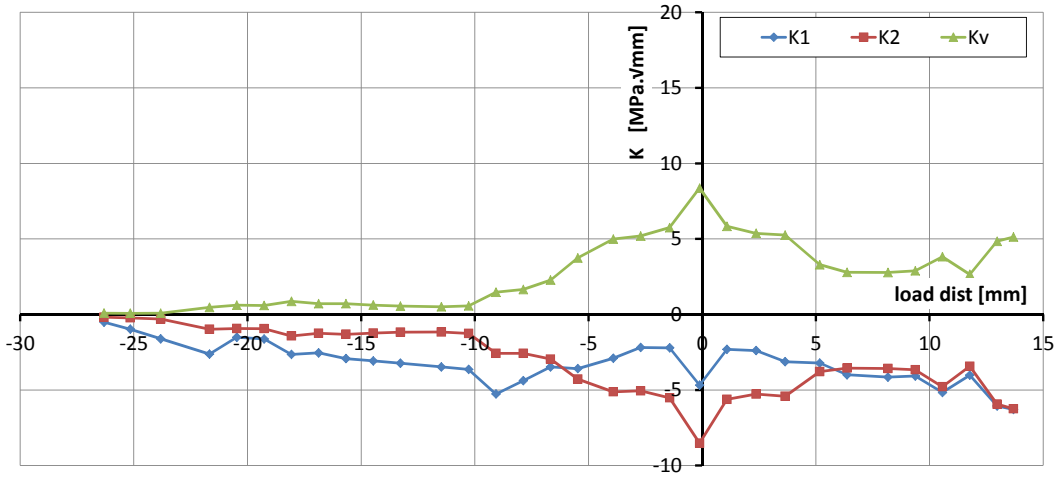

(a) Left crack tip K_I, K_{II} and K_V evolution.

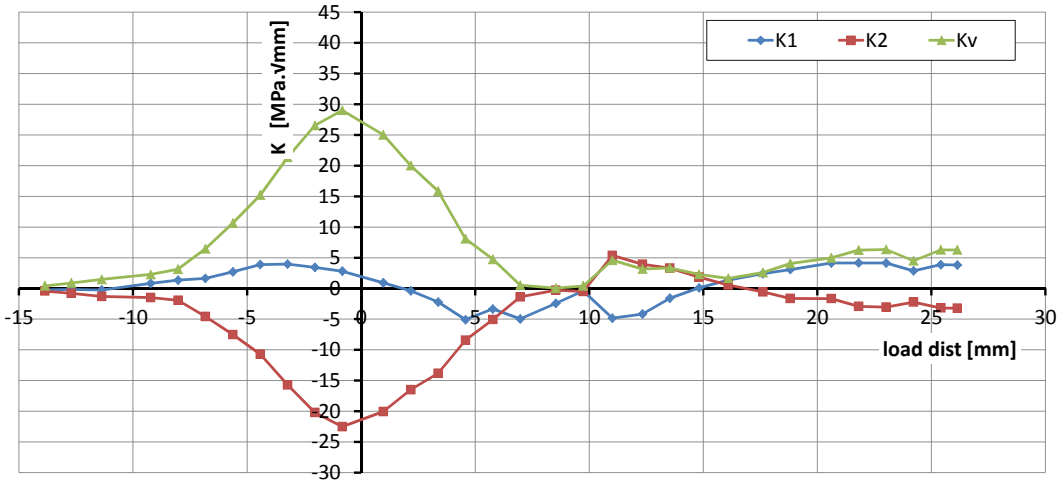

(b) Right crack tip K_I, K_{II} and K_V evolution.

Figure 8.9: Stress intensity factors evolution during load passage on the 16 mm crack.

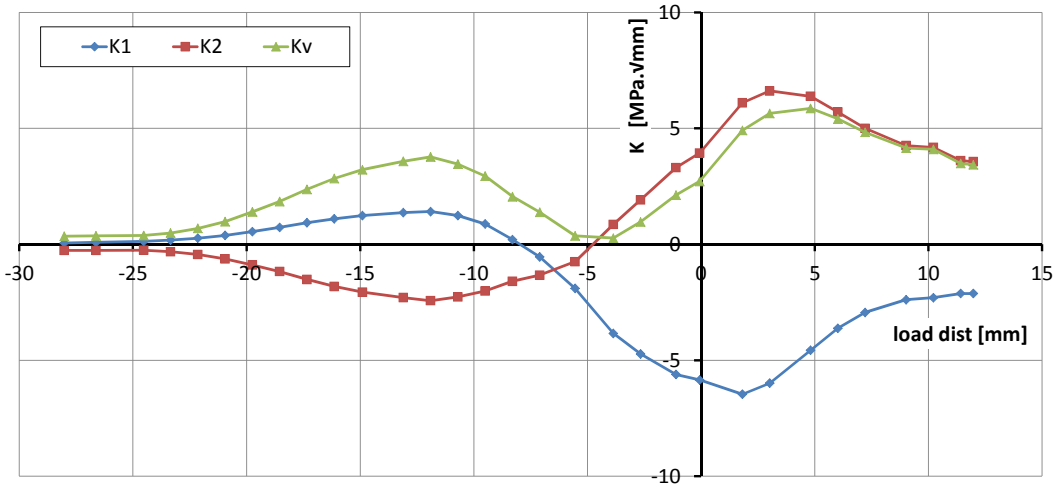

(a) Left crack tip K_I, K_{II} and K_V evolution.

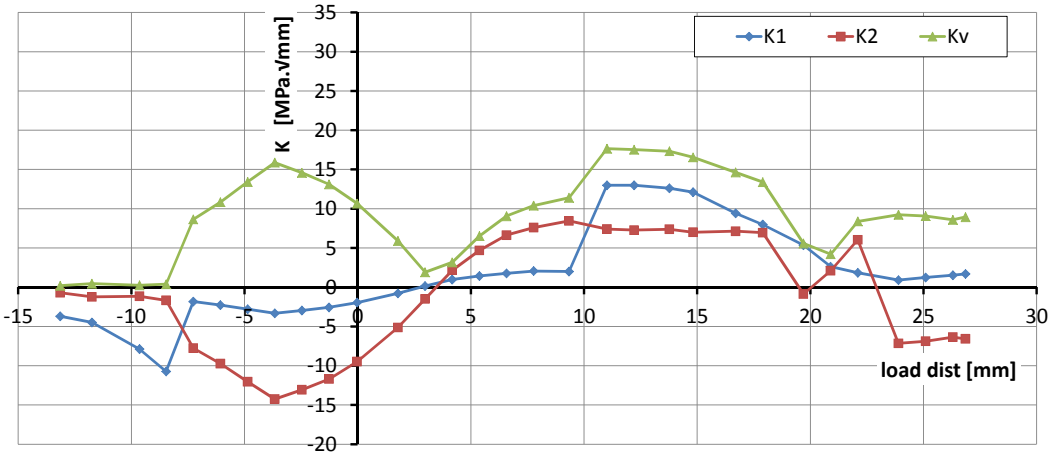

(b) Right crack tip K_I, K_{II} and K_V evolution.

Figure 8.10: Stress intensity factors evolution during load passage on the 18 mm crack.

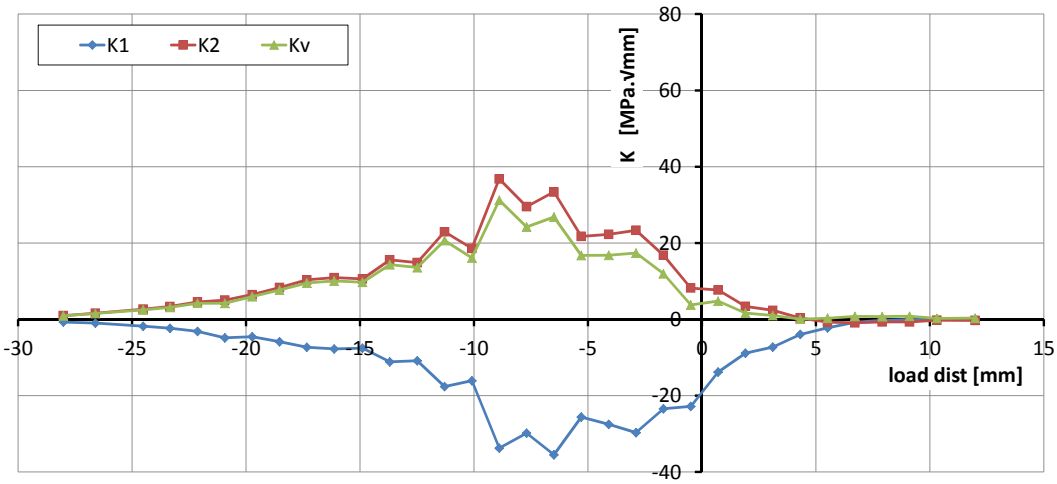

(a) Left crack tip K_I, K_{II} and K_V evolution.

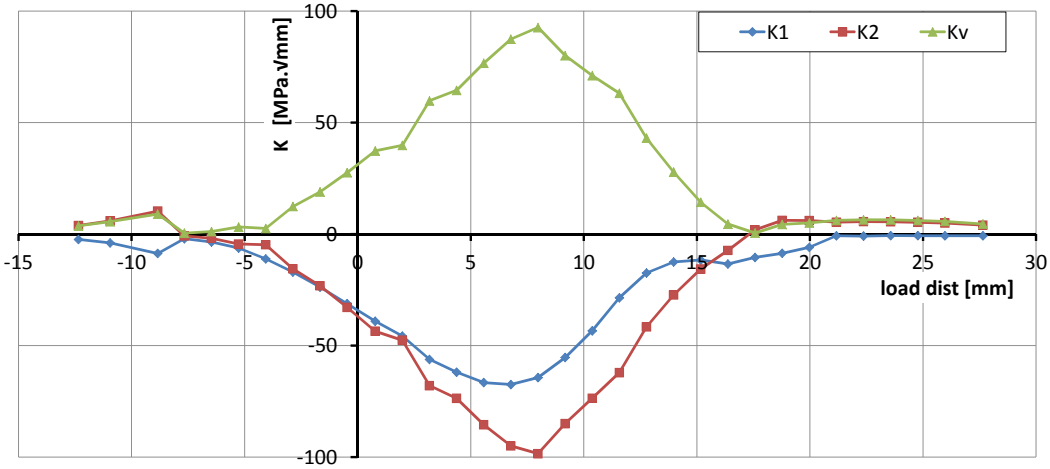

(b) Right crack tip K_I, K_{II} and K_V evolution.

Figure 8.11: Stress intensity factors evolution during load passage on the 20 mm crack.

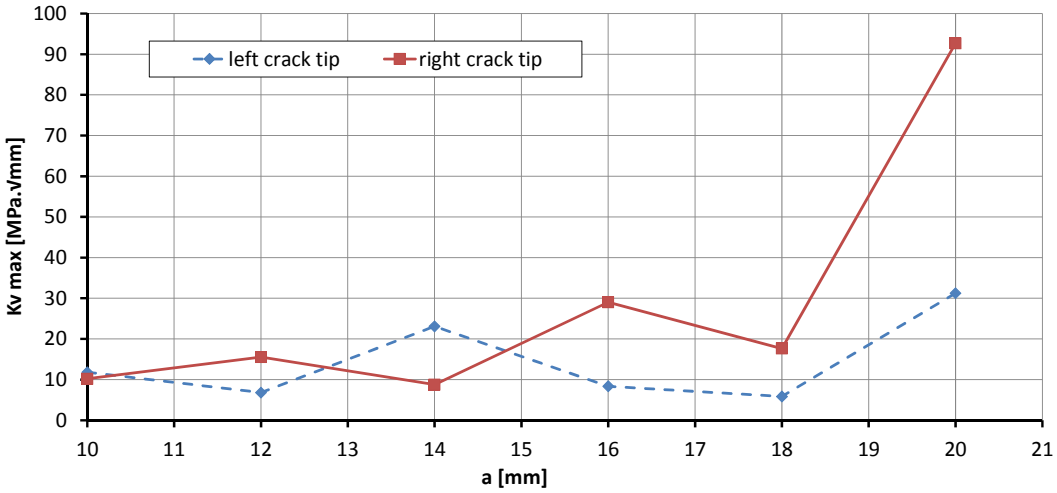

Figure 8.12: $K_{V\,max}$ *vs.* crack length.

8.4 Concluding remarks

The commercial finite element package ABAQUS 6.12-3 was used to build and analyze a 2D model a subsurface crack propagation on the wheel/rail contact.

The Maximum Tangential Stress (MTS) criterion was used to calculate the mode I and II stress intensity factors and the crack propagation direction along the crack tips loading cycle. Particular attention dedicated to the propagation direction of the crack at every increment of its length.

As can be observed in the presented results the crack change its direction from approximately +60º to -60º ate every increment of the crack length. This will promote a very irregular crack surface until the final fracture occurs.

As rolling contact induces complex non-proportional mixed-mode conditions at crack tips, the evolution of mode I and mode II stress intensity factors was followed along the loading cycle and no dominant mode at the crack tip was observed despite of the equivalent stress intensity factor being very sensitive to the variation of the mode II stress intensity factor.

In this study the calculation process ended when the maximum mixed mode equivalent stress intensity factor reached a value considered in the unstable propagation zone, which implies that the crack will growth rapidly until reaches the wheel surface.

It was observed that the presence of material defects, such a crack, cause very high localized stresses, mainly when it becomes longer.

One disadvantage of the used technique is that for every increment of the crack length it is necessary to rebuild the mesh considering the new crack length and its propagation angle. The propagation angle is also determined manually considering the angle given by the maximum tangential stress (MTS) technique, used to calculate the stress intensity factor at the crack tip, at which the maximum equivalent stress intensity factor at the crack tip has its maximum. All of this could be avoided if the extended finite element method (XFEM) was used[7], however some material properties that are needed to introduce in the model were not available.

[7] XFEM is now starting to be implemented in commercial FEM packages, as it is the case with ABAQUS 6.12-3.

Chapter 9

Contact fatigue damage on waved surfaces

Although the roughness of the contact surfaces varies with time, it is always present in service, and therefore a model for the prediction of its effect on fatigue damage initiation is a component of the overall problem of this thesis.
The influence of the surface waviness and roughness on the contact pressure, contact area and applied stresses, in particular the primary and secondary sub-surface stresses, was analyzed using a numerical solution of the Hertzian contact problem with waved surfaces.
The Hertz theory for the contact between elastic solids of revolution in line contact, subjected to normal and tangential loads, the contact pressure distribution on contact area, the stress fields in the contact surface and sub-surface are considered.
After considering the most common fatigue damage criteria applied to surfaces under contact stresses, in particular multi-axial fatigue models, a numerical tool was developed to predict contact fatigue damage initiation of waved surfaces in contact.
A parametric study was also performed to identify the influence of the material fatigue parameters and waviness wavelength and waviness amplitude on the fatigue resistance of the contact bodies.

9.1 Introduction

The behavior of solids in contact is analyzed by the theories of contact between elastic bodies.
These theories, firstly developed by Boussinesq, Cerutti and Hertz, e.g. [34], are concerned with the quantification of displacements, deformations and stresses resulting from an applied load.
The stresses and strains in the contact zone between the mechanical elements must be known to properly design the mechanisms and prevent fatigue phenomena or other damage.

Nowadays, surface and sub-surface contact fatigue damage is the most common failure mechanism in rolling bearings and gears.
Such failures are strongly dependent on the operating conditions (load, speed, sliding, ...), lubricant formulation (additives) and properties, surface roughness or waviness and lubricant specific film thickness.
Although several contact fatigue damage criteria are available there is not, yet, a clear basis to predict the fatigue damage of rough surfaces in contact.

9.2 Influence of surface waviness on surface and sub-surface stresses

The presence of a waved/rough surface on a contact causes modifications on the pressure distribution on the contact, with the appearance of several peaks - significantly higher than the maximum Hertz pressure - and the contact area is then formed by several small areas - generally smaller than the hertzian area. An example of this phenomenon is shown in Figures 9.1 and 9.2

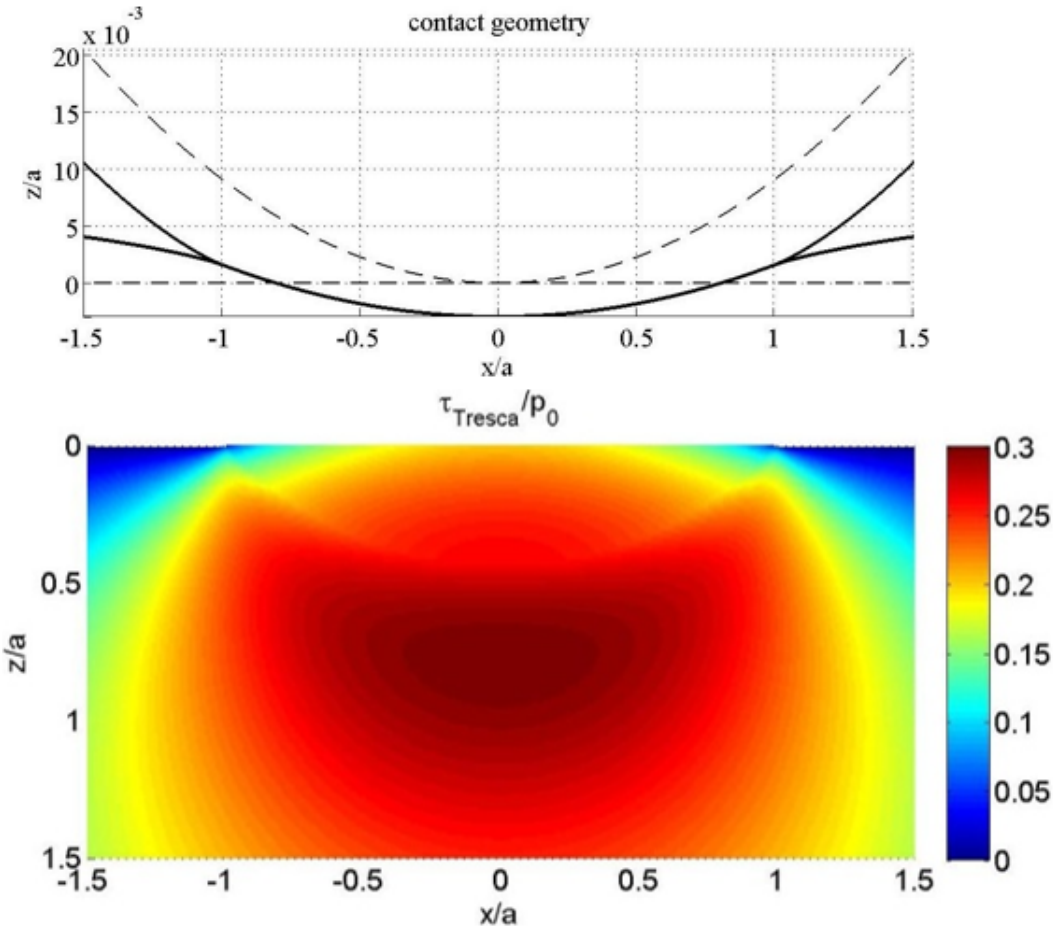

Figure 9.1: τ_{Tresca}/P_0 distribution in a contact between a smooth plane and a smooth cylinder ($P_0 = 1$ GPa).

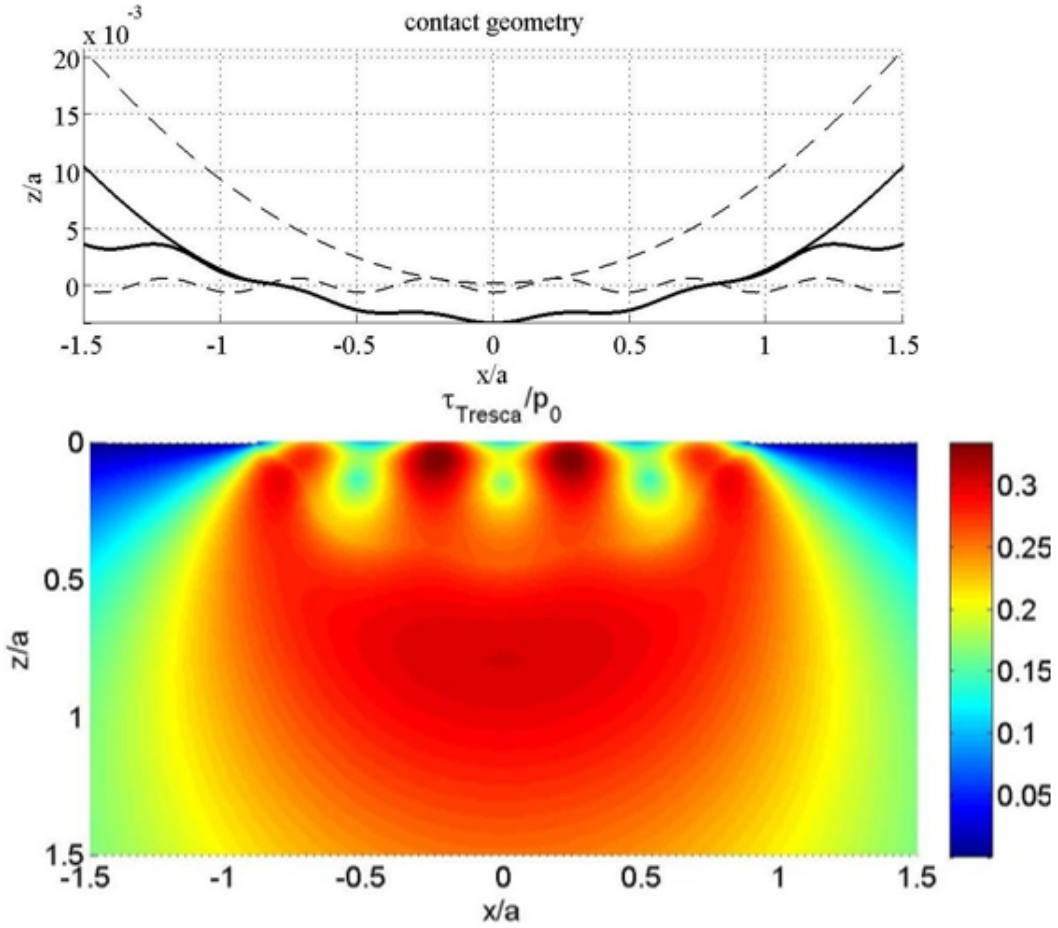

Figure 9.2: τ_{Tresca}/P_0 distribution in a contact between a waved plane with smooth cylinder contact ($P_0 = 1$ GPa).

However, in some cases the waviness effect can be negligible, *e.g.* if the waviness amplitude is too low or the load to high, the waviness peaks will be smashed by the load and the contact width will be approximately the hertzian contact width; or if the waviness wavelength is similar to the hertzian contact width, the contact width will be approximately equal to the hertzian contact width.
The stress distribution determination in waved/rough contacts implies the development of a numerical tool where the contact domain is discretized.

9.3 Influence of surface waviness on multiaxial fatigue criteria

The modifications on the stress field promoted by the irregular surface geometry imply that the resistance to contact fatigue of the contact bodies will be affected. After knowing the new stress field, changed by the presence of irregular surfaces on the contact, a fatigue analysis

must be performed to evaluate how the fatigue resistance was affected. The fatigue analysis of contact problems is a very complex problem since it implies the analysis of a multiaxial stress state. In order to solve this issue several multiaxial fatigue criteria were developed. In general, these criteria aim to establish an equivalent stress which can be comparable with material parameters obtained by uniaxial tests. This equivalent stress state can be established using several different methodologies as the critical plane approach proposed by Findley in [78] and by Matake in [79], the stress invariant approach proposed by Crossland in [80], and by Sines in [81]. Another approach presented by Dang Van in [6], proposes that the equivalent stress must be based on the analysis of local stresses distinguishing the macroscopic stresses, in the scale of the mm, from the mesoscopic stresses at the scale of a few grains of the material. In the present study it was decided to consider the Dang Van's fatigue criterion to perform the fatigue analysis. According to this criterion the equivalent stress at time t is calculated as a combination of the amplitude of the shear stress (τ_a) and of the hydrostatic stress (σ_h) evaluated during a load cycle. This criterion states that fatigue damage will occur if one or both conditions are verified:

$$\begin{aligned} \tau_a(t) + a_{DV} \times \sigma_h(t) > b \\ \tau_a(t) - a_{DV} \times \sigma_h(t) > -b \end{aligned} \tag{9.1}$$

where $b = \tau_{-1}$, the material fatigue limit in reversed torsion and a_{DV} is an non-dimensional constant, which represents the influence of hydrostatic stress, and can be determined by:

$$a_{DV} = 3\frac{\tau_{-1}}{\sigma_{-1}} - \frac{3}{2} \tag{9.2}$$

where σ_{-1} is the material fatigue limit in reversed bending. Figure 9.3 highlights that the fatigue resistance of the contact is highly affected by the presence of waved surfaces in the contact between two cylinders, since some points of the loading path become closer to the material fatigue limit.

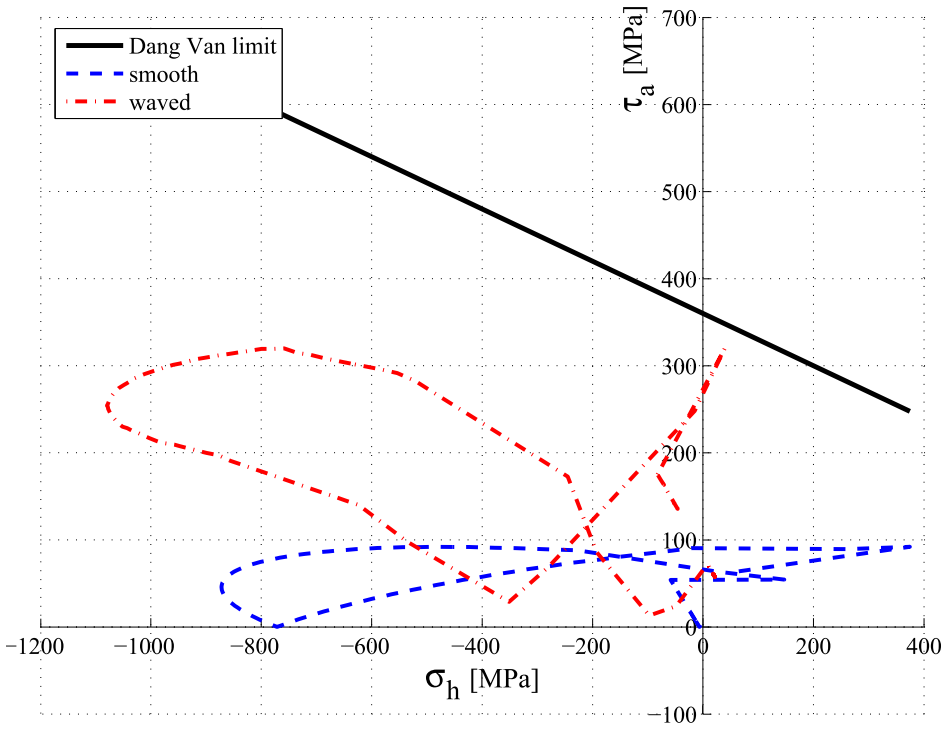

Figure 9.3: Loading paths for smooth and waved contact represented on the Dang Van's diagram.

9.4 Numerical tool

An algorithm capable to predict contact fatigue damage in waved surfaces in line contact, under normal and tangential loads, was developed.

That algorithm follows the method described in ref. [82], by Seabra *et al.*, to calculate the stress field in a waved contact and performs a fatigue analysis based on the Dang Van criterion.

The length of the analyzed elastic half-space was $20a$ (-$10a$ $< x <$ $10a$) and the load was moved between -$5a$ and $5a$ with $a/50$ increments aiming at obtaining a complete load cycle stress history.

In order to make the analysis of results more intuitive it was decided use a fatigue parameter concept, as the one presented by Qiao *et al.* in [83], based on the Dang Van criterion, as:

$$FP = \frac{\tau_a(t,\theta) + a_{DV} \times \sigma_h(t)}{b} \tag{9.3}$$

According to this concept if $FP > 1$ contact fatigue damage is predicted to occur. The developed code evaluates the highest FP parameter in every point of the discretization.

9.5 Parametric study

In this parametric study the influence of the waviness parameters, the wavelength and amplitude, and material fatigue properties on the contact fatigue resistance was studied.
To reach this objective the contact between a smooth cylinder and a waved cylinder, both with a radius of 70 mm, was considered as a reference contact problem. The applied normal load was $F_N = 1000$ N/mm and a friction coefficient of $\mu = 0.1$ was considered. The same Young modulus and Poisson's ratio were assumed for the cylinder and for the plane, equal to 200 GPa and 0.3 respectively.
The contact width and the maximum contact pressure for this reference contact problem were calculated using the Hertz theory and the obtained values were $a = 0.6368$ mm and $P_0 = 999.70$ MPa. The adopted methodology and the obtained results are presented in the subsequent paragraphs.

Influence of the surface waviness

To understand the effect of a non-smooth surface in the fatigue resistance of the contact, some values of the waviness wavelength and waviness amplitude were combined and the corresponding maximum value of the considered fatigue parameter was determined.
The influence of the waviness amplitude was analyzed from an amplitude of 0.1 to 1.0 μm ($0.16\times10^{-3} \leq amp/a \leq 1.57\times10^{-3}$) and the wavelength influence in the range from 0.006 to 0.32 mm ($0.01 \leq \lambda/a \leq 0.5$), where a is the hertzian contact width. The considered material fatigue parameters, as the material fatigue limit in reversed bending, the material fatigue limit in reversed torsion are presented in Table 9.1.

Table 9.1: Material fatigue properties considered.

σ_{-1} [MPa]	τ_{-1} [MPa]
600	360

The obtained results are presented in Figure 9.4 where the maximum value of the fatigue parameter obtained is represented as a function of waviness parameters.

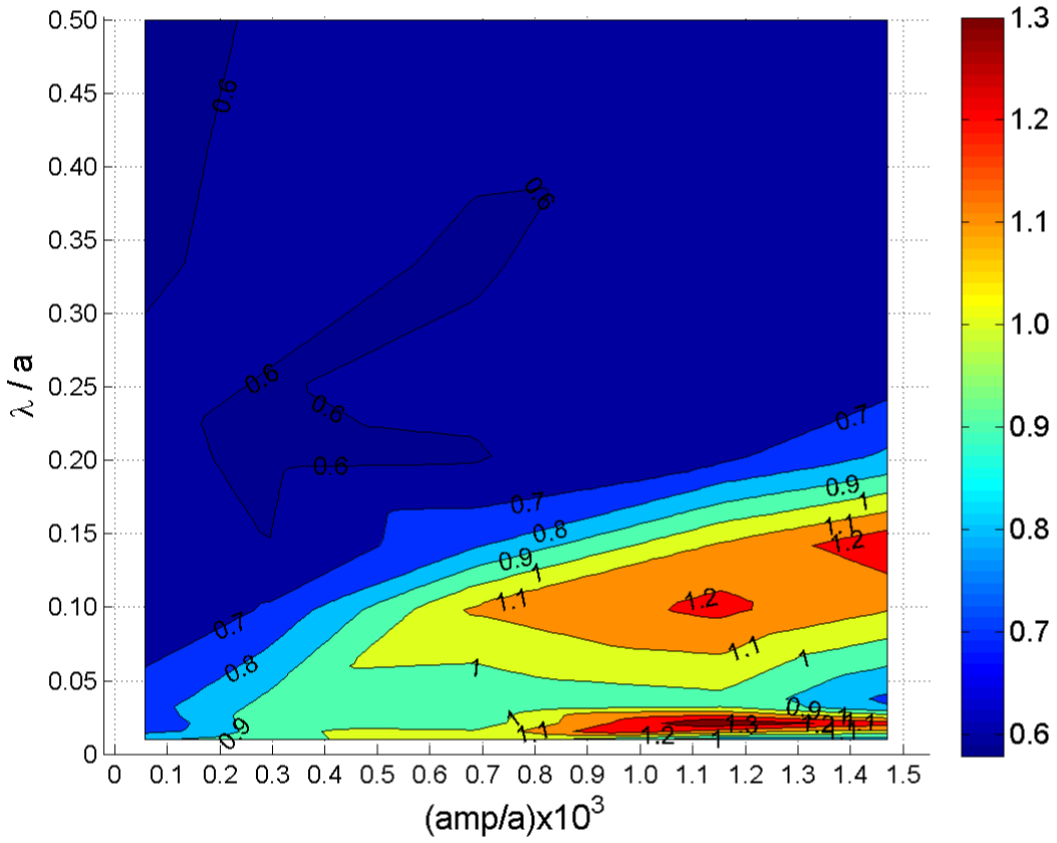

Figure 9.4: Contour representation of the influence of the waviness parameters on the fatigue parameter.

The analysis of these results revealed that for very low λ/a values ($0.015 \leq \lambda/a \leq 0.035$), which are far away from real surfaces, the highest fatigue parameter is obtained for amp/a values higher than 0.8×10^{-3}.

For λ/a values in the range 0.07 to 0.15, more interesting in terms of real surfaces, the fatigue parameter gets higher than 1.0 when amp/a increases from 0.5×10^{-3} to 1.2×10^{-3}.

So, the numerical method developed puts into evidence that some micro-geometries are more harmful than others in terms of contact fatigue damage. Four combinations of λ/a *vs.* amp/a were chosen from Figure 9.4 and their loading paths were represented in the Dang Van diagram, as shown in Figure 9.5.

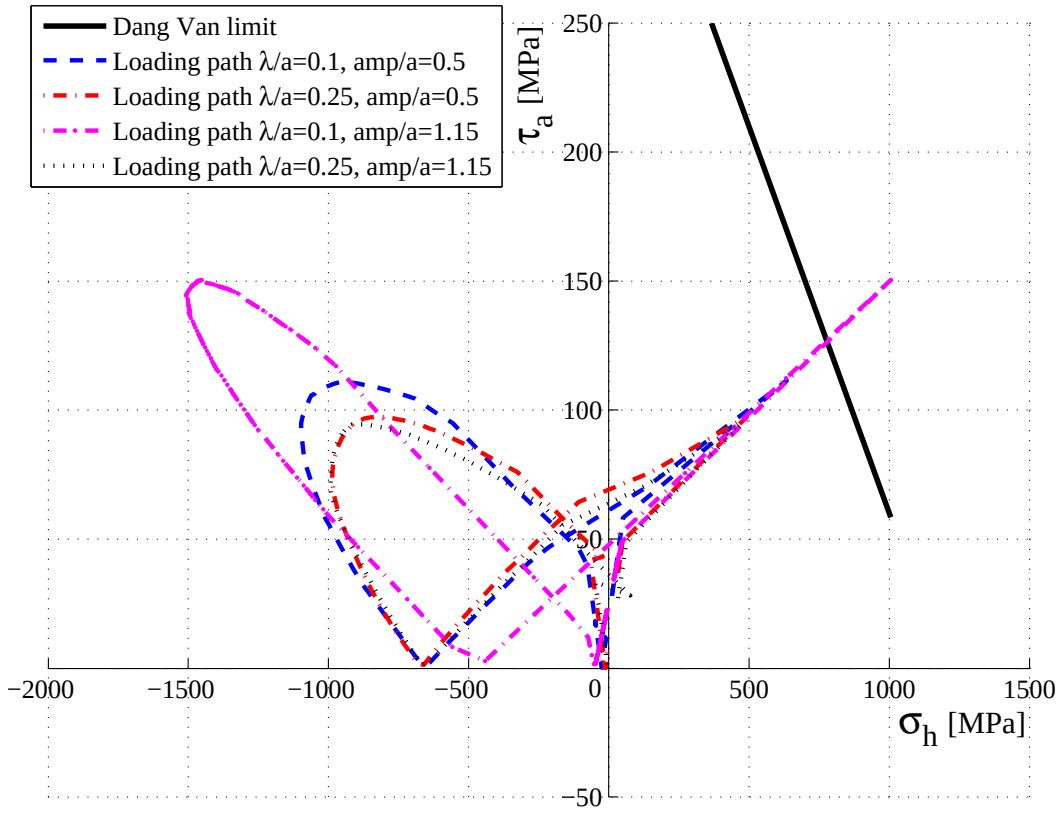

Figure 9.5: Dang Van's diagram for four different combinations of waviness parameters.

Figure 9.5 highlights the effect of waviness parameters of the contact bodies on the loading path, including a case were the fatigue limit is exceeded ($\lambda/a = 0.1$ and $amp/a = 1.15$) only due to the waviness characteristics.

Influence of the material fatigue properties

According to the Dang Van criterion, considered in this study, the materials fatigue resistance is represented by the a_{DV} and b parameters. Thereby, these two parameters were combined to evaluate the material fatigue properties influence maintaining constant the waviness of the contact bodies.

For metals the material fatigue limit in reversed bending and the fatigue limit in reversed torsion, according to Zenner *et al.* [84], can be related as:

$$0.577 \leq \frac{\tau_{-1}}{\sigma_{-1}} \leq 0.866 \tag{9.4}$$

Thus thea_{DV} parameter range can be estimated as:

$$0.2 \leq a_{DV} \leq 1 \tag{9.5}$$

However, the influence of the a_{DV} parameter was analyzed in the range 0.1 to 1.1 in order to understand the influence of a_{DV} if the limits established by equation (9.5) are exceeded.

On the other hand the influence of the parameter b was studied between 100 and 600 MPa. The considered waviness of one of the waved cylinder is characterized by a wavelength $\lambda =$ 0.2 mm ($\lambda/a = 0.31$) and amplitude amp =0.25 μm ($amp/a = 3.9\times10^{-4}$). The obtained results are presented in Figure 9.6 and Figure 9.7, where the maximum Dang Van fatigue parameter is represented as a function of a_{DV} and b values.

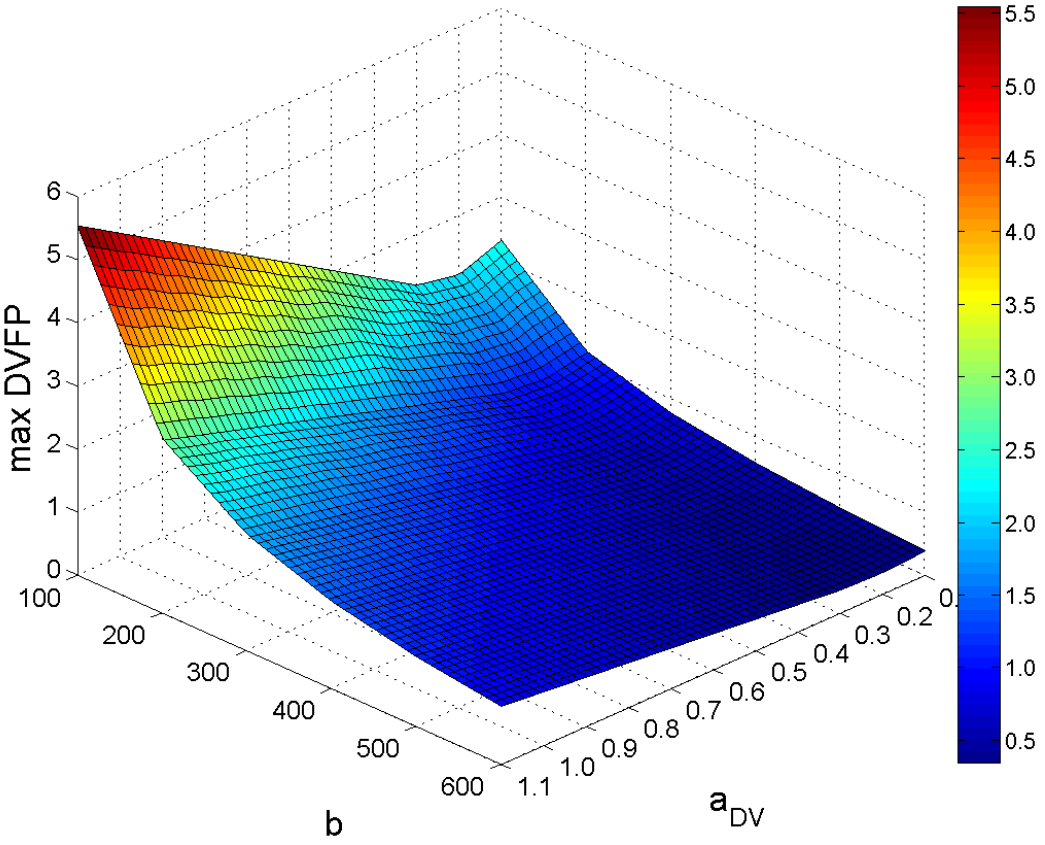

Figure 9.6: 3D representation of material properties influence on the maximum value of the Dang Van fatigue parameter.

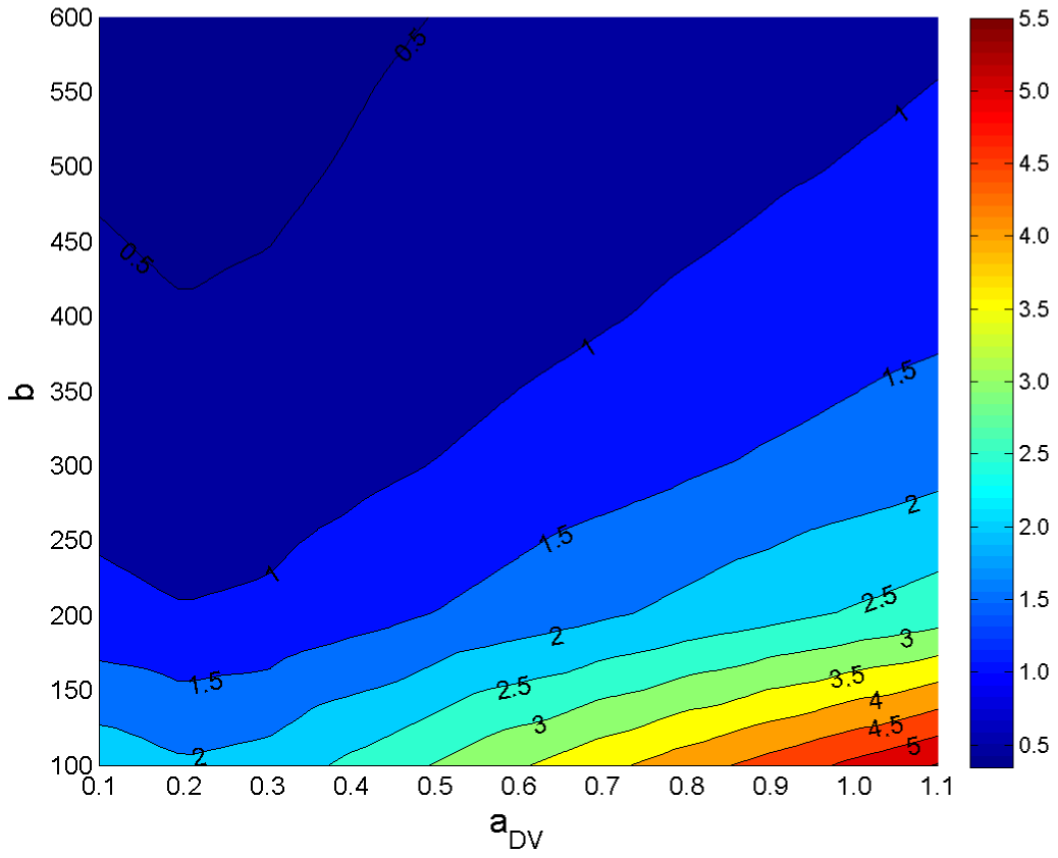

Figure 9.7: Contour representation of material properties influence on the maximum value of the Dang Van fatigue parameter.

Analyzing these results it can be concluded that the maximum value of the fatigue parameter decreases as the parameter b increases, for the same value of a_{DV} parameter, and the a_{DV} parameters has higher influence on the contact fatigue resistance for lower values of b.

9.6 Concluding remarks

The influence of the surface waviness, friction coefficient and load magnitude on the stresses distribution and also the method to calculate the stress field distribution was analyzed leading to the following conclusions:

- the presence of a waved surface on the contact promotes the appearance of several stress peaks near the contact surface;
- decreasing the amplitude of the roughness increases the contact area and thus lowers the maximum pressure peaks
- increasing the contact load smashes the waviness peaks which increases the contact area and decreases the effect of the waviness on the stress distribution.

The numerical tool based on the Dang Van criterion developed to predict contact fatigue damage of waved surfaces in line contact was used to perform a parametric study on the influence of the waviness parameters and Dang Van's criterion parameters.

The obtained results led to conclude that for waviness amplitudes near to 0.1 the maximum value of the Dang Van's fatigue parameter is almost constant and for wavelengths higher then 0.15 ($\lambda > a/4$) the influence of waviness (wavelength and amplitude) is almost negligible. These results suggest that when the waviness amplitude is too low and/or the waviness wavelength is similar to the hertzian contact width we have a theoretical contact problem described by the Hertz theory and the waviness has a negligible effect on the results.

Analyzing the obtained results it can be concluded, also, that the maximum value of the Dang Van's fatigue parameter decreases as the parameter b increases, for the same value of a_{DV} parameter and the minimum value of the Dang Van's fatigue parameter is obtained with a a_{DV} parameter of about 0.2, which is equivalent to say that a material with a ratio$\tau_{-1}/\sigma_{-1} \approx$ 0.57 has a good fatigue resistance.

Concluding remarks

A material characterization including chemical composition analysis, mechanical properties determination, microstructure and hardness measurements, was performed on samples taken from an AVE train wheel that reached the geometrical limits for continued usage and from a UIC60 section rail.

These tests revealed that the material tested are the ER7/ER8 grade wheel steel, according to the EN 13262 standard and the R260 MN grade rail steel according to the EN 13674 standard. Both steels revealed a pearlitic microstructure.

The twin-disc rolling contact fatigue tests performed in the wheel and rail materials allowed to conclude that under the chosen test conditions the running-in phase of the studied materials ends after approximately 5 million rotations, and rolling contact fatigue cracks appear at the contact surface after 15 to 18 million cycles in lubricated conditions.

It was verified, during lubricated tests, that the wheel material is more sensitive to defect initiation, since the larger number of defects was observed in the wheel specimens.

However, during dry tests no defect was detected, probably due to the high wear rate that removes any crack that appears at the contact surface.

The wheel material presents a higher wear rate than the rail material, which is more noticeable in dry tests.

The disc specimens tested in the twin-disc machine were extracted from the wheel and rail profiles in different orientations and locations, without significant influence on the results.

A methodology to calculate the mass loss from the variation of the discs' roughness profile was developed and good agreement was found with mass measurements.

Mode I fatigue crack growth tests were performed according to the ASTM E647 standard on C(T) specimens taken from a Spanish high speed AVE train wheel and a UIC60 rail, tested with 0.1, 0.4 and 0.7 load ratios.

These tests shown that the rail material presents higher fatigue crack growth rates than the wheel material, the effect of R-ratio is most notable in the rail material.

Data obtained for the wheel and rail materials shows lower values of $\triangle K_{th}$ for higher *R-values*. Present near threshold values are lower than published data found in the literature, also obtained using the load shedding technique.

On the basis of the limited experimental evidence obtained by the authors, it is concluded that the ASTM method leads to higher $\triangle K_{th}$ values than K_{max} constant procedure.

It was observed that the measured threshold stress-intensity range for fatigue-crack propagation, $\triangle K_{th}$, decreases as the load ratio is increased. For the high *R-ratio* tested according to the ASTM procedure the obtained results are very similar to the results obtained with K_{max} constant procedure.

Fatigue crack growth rates and the propagation angle were evaluated under mixed-mode (mode-I and mode-II) conditions on Compact Tension Shear (CTS) specimens taken from a Spanish AVE train wheel. Three different loading angles were tested 30º, 45º and 60º.

Since no numerical solution exists to calculate the K_I and K_{II} values a finite element analysis was also performed in order to obtain their values for the tested conditions.

It was observed that the fatigue crack growth direction changed immediately from the initial fatigue mode-I pre-crack orientation when load direction was changed.

The experimental growth direction of the cracks for different load mixities were compared with the predictions based on numerical approaches (ABAQUS and Broek equation) which provide a similar estimation of the crack growth direction and a good agreement with the experimental results.

It was observed that for the tested $\triangle K$ range the mixed mode fatigue crack growth rates are higher than the mode I fatigue crack growth rates. However, for lower $\triangle K$ values or near the threshold the mixed mode fatigue crack growth rates could be lower than the mode I fatigue crack growths.

Striation spacing measurements were performed in four different C(T) specimens, taken from an AVE wheel and UIC60 rail, which were previously used in fatigue crack growth rates tests. These measurements led to the conclusion that there is no correlation between fatigue crack growth and striation spacing and the striation orientation is randomness without any relation to the fatigue crack propagation direction.

The commercial finite element package ABAQUS 6.12-3 was used to build and analyze a 2D model a subsurface crack propagation on the wheel/rail contact.

The Maximum Tangential Stress (MTS) criterion was used to calculate the mode I and II stress intensity factors and the crack propagation direction along the crack tips loading cycle. The crack changed its direction from approximately +60º to -60º at every increment of the crack length which promotes a very irregular crack surface until the final fracture occurs.

In this study the calculation process ended when the maximum mixed mode equivalent stress intensity factor reached a value considered in the unstable propagation zone, which implies that the crack will growth rapidly until it reaches the wheel surface.

It was observed that the presence of material defects, such a crack, promotes very high localized stresses, mainly when it becomes longer.

The numerical tool based on the Dang Van criterion developed to predict contact fatigue damage of waved surfaces in line contact was used to perform a parametric study on the influence of the waviness parameters and Dang Van's criterion parameters. The obtained results led to conclude that for waviness amplitudes near to 0.1 the maximum value of the Dang Van's

fatigue parameter is almost constant and for wavelengths higher then 0.15 ($\lambda > a/4$) the influence of waviness (wavelength and amplitude) is almost negligible. These results suggest that when the waviness amplitude is too low and/or the waviness wavelength is similar to the hertzian contact width we have a theoretical contact problem described by the Hertz theory and the waviness has a negligible effect on the results. These obtained results also led to the conclusion that the maximum value of the Dang Van's fatigue parameter decreases as the parameter b increases, for the same value of a_{DV} parameter and the minimum value of the Dang Van's fatigue parameter is obtained with a a_{DV} parameter of about 0.2, which is equivalent to say that a material with a ratio$\tau_{-1}/\sigma_{-1} \approx 0.57$ has a good fatigue resistance.
Thus, the fatigue and wear behaviour, the most important aspects of wheel/rail interaction, were analysed in this work, contributing to improve the knowledge of the behaviour in service of the relevant materials in the presence of defects and when they are put into contact in different conditions (lubricated and dry contact). It was verified that the presence of a lubricant in the contact between these two materials can reduce significantly the amount of wear.
The experimental results obtained in the mixed mode tests were crucial in the validation of the numerical techniques that were then applied to the 2D numerical simulation of fatigue crack propagation on the wheel.
As it was not possible to study experimentally the fatigue crack initiation in the twin-disc tests, a numerical tool was helpful to understand this phenomenon in the perspective of the influence of some involved parameters as the surface quality (roughness) and material properties.
In conclusion, the objectives that motivated this thesis (contribute to develop a methodology to anticipate the need for repair or replacement of wheels or rails) were achieved.

Suggestion for future work

This is a brief list of further work that could be done to continue the research developed and presented in this thesis:

- Hardness profile measurements of a used rail section;
- Reconfiguration of the twin disc machine to perform tests with controlled slip in contact with materials with different wear rates;
- Perform twin-disc tests using other operating parameters such as loads, speeds and other types of lubricants (*e.g.* greases);
- Mixed mode tests on wheel material using other *R-ratios* and other loading angles;
- Mixed mode tests on rail material;
- Use other techniques, such image processing, to measure the crack length and even obtain experimentally the stress intensity factor at the crack tip during fatigue crack growth tests;
- Use the more complete results of the mixed mode tests to perform a life prediction after defect initiation on the wheel.

References

[1] A. Ekberg and E. Kabo, "Fatigue of railway wheels and rails under rolling contact and thermal loading - an overview," *Wear*, vol. 258, no. 7, pp. 1288 – 1300, 2005.

[2] D. Cannon and H. Pradier, "Rail rolling contact fatigue research by the european rail research institute," *Wear*, vol. 191, no. 1, pp. 1 – 13, 1996.

[3] P. Clayton, "Tribological aspects of wheel-rail contact: a review of recent experimental research," *Wear*, vol. 191, no. 1, pp. 170 – 183, 1996.

[4] E. Kabo and A. Ekberg, "Fatigue initiation in railway wheels - a numerical study of the influence of defects," *Wear*, vol. 253, no. 1, pp. 26 – 34, 2002.

[5] U. Zerbst and S. Beretta, "Failure and damage tolerance aspects of railway components," *Engineering Failure Analysis*, vol. 18, no. 2, pp. 534 – 542, 2011.

[6] K. Dang-Van, "Macro-micro approach in high-cycle multiaxial fatigue," *ASTM STP 1191*, pp. 120 – 120, 1993.

[7] G. Donzella, M. Faccoli, A. Ghidini, A. Mazzu, and R. Roberti, "The competitive role of wear and rcf in a rail steel," *Engineering Fracture Mechanics*, vol. 72, no. 2, pp. 287 – 308, 2005.

[8] UIC, "Atlas of wheel and rail defects," 2004.

[9] C. Esveld, *Modern railway track*. MRT-productions Zaltbommel, The Netherlands, 2001.

[10] G. Marquis and D. Socie, "Crack propagation under cyclic hydraulic pressure loading," *International Journal of Fatigue*, vol. 19, no. 7, pp. 543–550, 1997.

[11] A. Bower, "The influence of crack face friction and trapped fluid on surface initiated rolling contact fatigue cracks," *Journal of Tribology*, vol. 110, pp. 704–712, 1988.

[12] B. Zafošnik, Z. Ren, J. Flašker, and G. Mishuris, "Modelling of surface crack growth under lubricated rolling–sliding contact loading," *International Journal of Fracture*, vol. 134, no. 2, pp. 127–149, 2005.

[13] J. Kalousek, E. Magel, J. Strasser, W. Caldwell, G. Kanevsky, and B. Blevins, "Tribological interrelationship of seasonal fluctuations of freight car wheel wear, contact fatigue shelling and composition brakeshoe consumption," *Wear*, vol. 191, no. 1, pp. 210 – 218, 1996.

[14] A. Ekberg, "Rolling contact fatigue of railway wheels - a parametric study," *Wear*, vol. 211, no. 2, pp. 280 – 288, 1997.

[15] M. Clarke, "Wheel steel guide," Rail Safety and Standards Board, Tech. Rep., 2008.

[16] R. A. Agarwal, A., *Rail Steel*, 3rd ed. Indian Railways Institute of Civil Engineering, March 2007.

[17] F. Hernández, N. Demasb, D. Davisa, A. Polycarpou, and L. Maalc, "Mechanical properties and wear performance of premium rail steels," *Wear*, vol. 263, pp. 766 – 772, 2007.

[18] J. Pacyna, "The microstructure and properties of the new bainitic rail steels," *Journal of Achievements in Materials and Manufacturing Engineering*, vol. 28, pp. 19–22, 2008.

[19] J. Ringsberg, A. Skyttebol, and B. Josefson, "Investigation of the rolling contact fatigue resistance of laser cladded twin-disc specimens: Fe simulation of laser cladding, grinding and a twin-disc test," *International Journal of Fatigue*, vol. 27, no. 6, pp. 702–714, 2005.

[20] E. Gallardo-Hernandez, R. Lewis, and R. Dwyer-Joyce, "Temperature in a twin-disc wheel/rail contact simulation," *Tribology International*, vol. 39, no. 12, pp. 1653–1663, 2006.

[21] M. Takikawa and Y. Iriya, "Laboratory simulations with twin-disc machine on head check," *Wear*, vol. 265, no. 9, pp. 1300 – 1308, 2008.

[22] N. Tassini, X. Quost, R. Lewis, R. Dwyer-Joyce, C. Ariaudo, and N. Kuka, "A numerical model of twin disc test arrangement for the evaluation of railway wheel wear prediction methods," *Wear*, vol. 268, no. 5, pp. 660 – 667, 2010.

[23] A. Rovira, A. Roda, R. Lewis, and M. Marshall, "Application of FASTSIM with variable coefficient of friction using twin disc experimental measurements," *Wear*, vol. 274, pp. 109 – 126, 2012.

[24] J. Seo, S. Kwon, D. Lee, and H. Choi, "Analysis of contact fatigue crack growth using twin-disc tests and numerical evaluations," *International Journal of Fatigue*, 2013.

[25] C. Hooke, S. Kukureka, P. Liao, M. Rao, and Y. Chen, "Wear and friction of nylon-glass fibre composites in non-conformal contact under combined rolling and sliding," *Wear*, vol. 197, no. 1, pp. 115 – 122, 1996.

[26] J. Sukumaran, M. Ando, P. De Baets, V. Rodriguez, L. Szabadi, G. Kalacska, and V. Paepegem, "Modelling gear contact with twin-disc setup," *Tribology International*, vol. 49, pp. 1–7, 2012.

[27] L. Magalhães, J. Seabra, and C. Sá, "Experimental observations of contact fatigue crack mechanisms for austempered ductile iron (ADI) discs," *Wear*, vol. 246, no. 1, pp. 134 – 148, 2000.

[28] L. Magalhães and J. Seabra, "Artificial indentations for the study of contact fatigue of austempered ductile iron (adi) discs," *Wear*, vol. 258, no. 11, pp. 1755 – 1763, 2005.

[29] R. Amaro, R. Martins, J. Seabra, N. Renevier, and D. Teer, "Molybdenum disulphide/titanium low friction coating for gears application," *Tribology International*, vol. 38, no. 4, pp. 423–434, 2005.

[30] S. Kukureka, C. Hooke, M. Rao, P. Liao, and Y. Chen, "The effect of fibre reinforcement on the friction and wear of polyamide 66 under dry rolling–sliding contact," *Tribology International*, vol. 32, no. 2, pp. 107–116, 1999.

[31] V. M. M. B. da Mota, P. M. G. P. Moreira, and L. A. A. Ferreira, "A study on the effects of dented surfaces on rolling contact fatigue," *International Journal of Fatigue*, vol. 30, no. 10, pp. 1997–2008, 2008.

[32] V. Mota and L. A. A. Ferreira, "Influence of grease composition on rolling contact wear: Experimental study," *Tribology International*, vol. 42, no. 4, pp. 569–574, 2009.

[33] A. Rego, D. F. C. Peixoto, and L. A. A. Ferreira, "Rolling contact fatigue tests in a twin disc machine," in *IBERTRIB 2011- VI Iberian Congress on Tribology*, June 16-17, Madrid, Spain, 2011.

[34] K. L. Johnson, *Contact mechanics*. Cambridge University Press, 1987.

[35] V. Hauk and E. Macherauch, *Eigenspannungen und Lastspannungen: moderne Ermittlung Ergebnisse Bewertung*. Carl Hanser, 1982.

[36] V. Hauk, *Structural and Residual Stress Analysis by Nondestructive Methods: Evaluation-Application-Assessment*. Access Online via Elsevier, 1997.

[37] G. Maeder, "Mesure de contraintes résiduelles par diffraction x," *Revue Française de Mácanique*, vol. 82, pp. 57–70, 1982.

[38] ASTM, *Standard Test Method for Measurement of Fatigue Crack Growth Rates*, American Society for Testing and Materials, standard E647 Std., 2008.

[39] A. El-Shabasy and J. Lewandowski, "Effects of load ratio, R, and test temperature on fatigue crack growth of fully pearlitic eutectoid steel (fatigue crack growth of pearlitic steel)," *International Journal of Fatigue*, vol. 26, pp. 305–309, 2004.

[40] A. Skyttebol, B. Josefson, and J. Ringsberg, "Fatigue crack growth in a welded rail under the influence of residual stresses," *Engineering Fracture Mechanics*, vol. 72, no. 2, pp. 271–285, 2005.

[41] H. Aglan and Y. Gan, "Fatigue crack growth analysis of a premium rail steel," *Journal of Materials Science*, vol. 36, no. 2, pp. 389–397, 2001.

[42] J. Bulloch, "Fatigue crack growth studies in rail steels and associated weld metal," *Theoretical and Applied Fracture Mechanics*, vol. 6, no. 2, pp. 75–84, 1986.

[43] M. Zain, N. Jamaludin, Z. Sajuri, M. Yusof, and Z. Hanafi, "Acoustic emission study of fatigue crack growth in rail track material," in *National Conference in Mechanical Engineering Research and Postgraduate Studies (2nd NCMER)*, 2010, pp. 82–90.

[44] C. Feddersen and D. Broek, "Fatigue crack propagation in rail steels," *ASTM STP 644*, pp. 414 – 429, 1978.

[45] P. Liaw, "Overview of crack closure at near-threshold fatigue crack growth levels," *Mechanics of Fatigue Crack Closure, ASTM STP 982*, pp. 62–92, 1988.

[46] B. Boyce and R. Ritchie, "Effect of load ratio and maximum stress intensity on the fatigue threshold in Ti–6Al–4V," *Engineering Fracture Mechanics*, vol. 68, no. 2, pp. 129 – 147, 2001.

[47] S. Forth, J. Newman Jr, and R. Forman, "On generating fatigue crack growth thresholds," *International Journal of Fatigue*, vol. 25, no. 1, pp. 9–15, 2003.

[48] S. Smith and R. Piascik, "An indirect technique for determining closure-free fatigue crack growth behavior," *ASTM STP 1372*, pp. 109 – 122, 2000.

[49] M. Carboni and D. Regazzi, "Effect of the experimental technique onto R dependence of ΔK_{th}," *Procedia Engineering, 11th International Conference on the Mechanical Behavior of Materials (ICM11)*, vol. 10, pp. 2937 – 2942, 2011.

[50] R. Davenport and R. Brook, "The stress intensity range in fatigue," *Fatigue and Fracture of Engineering Materials and Structures*, vol. 1, pp. pp. 151–158, 1979.

[51] R. Ritchie, "Near-threshold fatigue crack propagation in ultra-high strength steel: influence of load ratio and cyclic strength," *Journal of Engineering Materials and Technology*, vol. 99, no. 3, 1977.

[52] J. Kim and C. Kim, "Fatigue crack growth behavior of rail steel under mode i and mixed mode loadings," *Materials Science and Engineering: A*, vol. 338, no. 1, pp. 191–201, 2002.

[53] S. Suresh and R. Ritchie, "On the influence of environment on the load ratio dependence of fatigue thresholds in pressure vessel steel," *Engineering Fracture Mechanics*, vol. 18, no. 4, pp. 785–800, 1983.

[54] R. Ritchie, "Near-threshold fatigue-crack propagation in steels," *International Materials Reviews*, vol. 24, no. 1, pp. 205–230, 1979.

[55] A. Heshmat, "Fatigue crack growth and fracture behavior of bainitic rail steel," U.S. Department of Transportation, Federal Railroad Administration, Office of Railroad Policy and Development, Washington DC 20590, Tech. Rep., September 2011.

[56] S. Sivaprasad, S. Tarafder, V. Ranganath, and N. Parida, "Fatigue and fracture behaviour of forged and cast railway wheels," in *11th International Conference on Fracture*, Turin, Italy, March 2005, pp. 20–25.

[57] R. Hamam, S. Pommier, and F. Bumbieler, "Variable amplitude fatigue crack growth, experimental results and modeling," *International Journal of Fatigue*, vol. 29, no. 9, pp. 1634–1646, 2007.

[58] S. Biner, "Fatigue crack growth studies under mixed-mode loading," *International Journal of Fatigue*, vol. 23, pp. 259–263, 2001.

[59] S. Wong, P. Bold, M. Brown, and R. Allen, "Fatigue crack growth rates under sequential mixed-mode I and II loading cycles," *Fatigue and Fracture of Engineering Materials and Structures*, vol. 23, no. 8, pp. 667–674, 2000.

[60] J. Qian and A. Fatemi, "Mixed mode fatigue crack growth: a literature survey," *Engineering Fracture Mechanics*, vol. 55, no. 6, pp. 969 – 990, 1996.

[61] M. Akama, "Fatigue crack growth under mixed loading of tensile and in-plane shear modes," *QR of RTRI*, vol. 44, no. 2, pp. 65 – 71, 2003.

[62] H. Richard, "Bruchvorhersagen bei überlagerter Normal - und Schubbeanspruchung von Rissen," *VDI Forschungsheft*, no. 631, pp. 1 – 60, 1985.

[63] K. Tanaka, "Fatigue crack propagation from a crack inclined to the cyclic tensile axis," *Engineering Fracture Mechanics*, vol. 6, no. 3, pp. 493–507, 1974.

[64] L. Borrego, F. Antunes, J. Costa, and J. Ferreira, "Mixed-mode fatigue crack growth behaviour in aluminium alloy," *International Journal of Fatigue*, vol. 28, pp. 618 – 626, 2006.

[65] H. Richard, "Crack problems under comples loading," *In: G.S. Sih, H. Nisitani, T. Ishihara, "Role of Fracture Mechanics in Modern Technology", Proceedings of the Int. Conf., Fukuoka, Japan, June 2-6, 1986, North-Holland, Amsterdan*, pp. 577 – 588, 1987.

[66] H. Richard, W. Linnig, and K. Henn, "Fatigue crack propagation under combined loading," *Forensic Eng*, vol. 3, pp. 99–109, 1991.

[67] K. Henn, H. Richard, and W. Linnig, "Fatigue crack growth under mixed mode and mode ii cyclic loading," *In: Czoboly E., Fracture analysis - theory and practice, EMAS Ltd, Warley*, vol. 2, pp. 1104 – 1113, 1988.

[68] J. Tong, J. Yates, and M. Brown, "The formation and propagation of mode i branch cracks in mixed mode fatigue failure," *Engineering Fracture Mechanics*, vol. 56, no. 2, pp. 213–231, 1997.

[69] Y. Xiangqiao, D. Shanyi, and Z. Zehua, "Mixed-mode fatigue crack growth prediction in biaxially stretched sheets," *Engineering Fracture Mechanics*, vol. 43, no. 3, pp. 471 – 475, 1992.

[70] J. Weertman, "Rate of growth of fatigue cracks calculated from the theory of infinitesimal dislocations distributed on a plane," *International Journal Fracture Mechanics*, vol. 2, pp. 460–467, 1966.

[71] F. Erdogan and G. Sih, "On the crack extension in plates under plane loading and transverse shear," *Journal of Basic Engineering*, vol. 85, pp. 519–525, 1963.

[72] ABAQUS, *ABAQUS v6.12-3 documentation*, Dassault Systèmes.

[73] E. Rybicki and M. Kanninen, "A finite element calculation of stress intensity factors by a modified crack closure integral," *Engineering Fracture Mechanics*, vol. 9, no. 4, pp. 931 – 938, 1977.

[74] D. Broek, *Elementary Engineering Fracture Mechanics*, 4th ed. Dordrecht: Martinus Nijhoff Publishers, 1987.

[75] P. M. G. P. Moreira and P. M. S. T. de Castro, "Fractographic analysis of fatigue crack growth in lightweight integral stiffened panels," *International Journal of Structural Integrity*, vol. 1, no. 3, pp. 233–258, 2010.

[76] H. Roven and E. Nes, "Cyclic deformation of ferritic steel ii. stage ii crack propagation," *Acta Metallurgica et Materialia*, vol. 39, no. 8, pp. 1735–1754, 1991.

[77] M. Dubourg and V. Lamacg, "A predictive rolling contact fatigue crack growth model: onset of branching, direction, and growth-role of dry and lubricated conditions on crack patterns," *Journal of Tribology*, vol. 124, no. 4, pp. 680–688, 2002.

[78] W. Findley, "A theory for the effect of mean stress on fatigue of metals under combined torsion and axial load or bending," *Journal of Engineering Industry, Trans ASME 81*, pp. 301–306, 1959.

[79] T. Matake, "An explanation on fatigue limit under combined stress," *Bull JSME*, vol. 20, pp. 257 – 263, 1977.

[80] B. Crossland, "Effect of large hydrostatic pressures on the torsional fatigue strength of an alloy steel," in *Proceedings of the International Conference on Fatigue of Metals*, Institution of Mechanical Engineers, London, 1956, pp. 138–149.

[81] G. Sines, *Metal Fatigue*, G. Sines and J. Waisman, Eds. N.Y: McGraw Hill, 1959.

[82] J. Seabra and D. Berthe, "Influence of surface waviness and roughness on the normal pressure distribution in the hertzian contact," *Journal of Tribology*, vol. 109, no. 3, pp. 462–470, 1987.

[83] H. Qiao, H. Evans, and R. Snidle, "Comparison of fatigue model results for rough surface elastohydrodynamic lubrication," *Proceedings of the Institution of Mechanical Engineers, Part J: Journal of Engineering Tribology*, vol. 222, no. 3, pp. 381–393, 2008.

[84] H. Zenner, A. Simbürger, and J. Liu, "On the fatigue limit of ductile metals under complex multiaxial loading," *International Journal of Fatigue*, vol. 22, no. 2, pp. 137–145, 2000.

Appendix A

Constant K_{max} test MATLAB code

This MATLAB ® code makes the calculations required to design a $\triangle K_{th}$ threshold test according to the ASTM E647 requirements, within the constraints of the chosen C(T) specimen dimensions.

```
%% Kmax CONSTANT TESTS SIMULATION
close all
clear all
clc

%% C(T) Specimen dimensions
    W=51.85/1000;     %[m]
    B=13.10/1000;     %[m]
    h=0.31/1000;      %[m]
    an=10.61/1000;    %[m]

%% Material yield stress
    Sy=504; %[MPa]

%% Simulation data for Da=constant

DK0=6;           %[MPa m^-1/2]
Da=0.6/1000;     %[m]
Kmax=10;         %[MPa m^-1/2]
C=-65;           %[1/m]
a0=20/1000;      %[m]

%% Average values claculations

i=1;
DK_average(i)=DK0;
Kmin_average(i)=Kmax-DK0;
Kmax_average(i)=Kmax;
R_average(i)=Kmin_average(i)/Kmax_average(i);
a_average(i)=a0+Da/2;
aW=a_average(i)/W;
f=(2+aW)/(1-aW)^(3/2)*(0.886+4.64*aW-13.32*aW^2+14.72*aW^3-5.6*aW^4);
Pmin(i)=Kmin_average(i)*B*sqrt(W)/f*1e6;
Pmax(i)=Pmin(i)/R_average(i);


```

```
while (W-a_average(i))>=(4/pi())*(Kmax_average(i)/Sy)^2&&DK_average(i)>0

    i=i+1;
    a_average(i)=a_average(i-1)+Da;
    DK_average(i)=DK0*exp(C*(a_average(i)-a0));
    Kmax_average(i)=Kmax;
    Kmin_average(i)=Kmax_average(i)-DK_average(i);
    R_average(i)=Kmin_average(i)/Kmax_average(i);
    aW=a_average(i)/W;
    f=(2+aW)/(1-aW)^(3/2)*(0.886+4.64*aW-13.32*aW^2+14.72*aW^3-5.6*aW^4);
    Pmin(i)=Kmin_average(i)*1e6*B*sqrt(W)/f;
    Pmax(i)=Pmin(i)/R_average(i);

end

Kmin_average(i)=NaN;
Kmax_average(i)=NaN;
DK_average(i)=NaN;
R(i)=NaN;
a_average(i)=NaN;
Pmax(i)=NaN;
Pmin(i)=NaN;

%% Experimental test simulation

for j=1:length(a_average)-1

    %Starting step values
    a(2*j-1)=a_average(j)-Da/2;
    aW=a(2*j-1)/W;
    f=(2+aW)/(1-aW)^(3/2)*(0.886+4.64*aW-13.32*aW^2+14.72*aW^3-5.6*aW^4);
    Kmin(2*j-1)= Pmin(j)/(B*sqrt(W))*f*1e-6;
    Kmax(2*j-1)= Pmax(j)/(B*sqrt(W))*f*1e-6;
    R(2*j-1)=Kmin(2*j-1)/Kmax(2*j-1);

        %Ending step values
    a(2*j)=a_average(j)+Da/2;
    aW=a(2*j)/W;
    f=(2+aW)/(1-aW)^(3/2)*(0.886+4.64*aW-13.32*aW^2+14.72*aW^3-5.6*aW^4);
    Kmin(2*j)= Pmin(j)/(B*sqrt(W))*f*1e-6;
    Kmax(2*j)= Pmax(j)/(B*sqrt(W))*f*1e-6;
    R(2*j)=Kmin(2*j)/Kmax(2*j);

%     Raux(j)=R(2*j)-R(2*j-1);

end


%% Graphical presentation of results
figure('color',[1.0 1.0 1.0])
subplot(2,2,1)
    hold on
    set(gca,'fontsize',14,'LineWidth',1.5)
    plot1=plot(a_average.*1000,Kmax_average);
    plot2=plot(a_average.*1000,Kmin_average);
    plot3=plot(a.*1000,Kmax);
```

```
93      plot4=plot(a.*1000,Kmin);
94      set(plot1,'LineWidth',1,'LineStyle','x','color','red')
95      set(plot2,'LineWidth',1,'LineStyle','x','color','blue')
96      set(plot3,'LineWidth',2,'LineStyle','-','color','red')
97      set(plot4,'LineWidth',2,'LineStyle','-','color','blue')
98      axis([10 60 0 12]);
99      xlabel('a [mm]')
100     ylabel('K [MPa.\surdm]')
101     legend('Kmáx','Kmin','Location','SouthEast')
102     grid on
103
104 subplot(2,2,2)
105     hold on
106     set(gca,'fontsize',14,'LineWidth',1.5)
107     plot5=plot(a_average.*1000,DK_average);
108     set(plot5,'LineWidth',2,'LineStyle',':','color','blue')
109 %     axis([10 60 0 DK0]);
110     xlabel('a [mm]')
111     ylabel('\DeltaK [MPa.\surdm]')
112 %     legend('\DeltaK','Location','NorthEast')
113     grid on
114
115 subplot(2,2,3)
116     hold on
117     set(gca,'fontsize',14,'LineWidth',1.5)
118     plot6=plot(a_average.*1000,Pmax);
119     plot7=plot(a_average.*1000,Pmin);
120     set(plot6,'LineWidth',2,'LineStyle','-','color','r')
121     set(plot7,'LineWidth',2,'LineStyle','--','color','b')
122 %       axis([10 60 0 5e3]);
123     xlabel('a [m]')
124     ylabel('Load [N]')
125     legend('Pmáx','Pmin','Location','NorthEast')
126     grid on
127
128 subplot(2,2,4)
129     hold on
130     set(gca,'fontsize',14,'LineWidth',1.5)
131     plot8=plot(a_average.*1000,R_average);
132     plot9=plot(a.*1000,R);
133     set(plot8,'LineWidth',2,'LineStyle','--','color','black')
134     set(plot9,'LineWidth',2,'LineStyle','-','color','blue')
135 %     axis([10 60 0 1]);
136     xlabel('a [m]')
137     ylabel('Load ratio (\it{R})')
138 %     legend('\DeltaK','Location','NorthEast')
139     grid on
140
141 % saveas(gcf,'Kmax_const_Da.png')
142 % close all
```

Appendix B

Articles published during this PhD work

- A.C. Batista, D.F.C. Peixoto, J.P. Nobre, L. Coelho, D.M. Ramos, L.A.A. Ferreira, P.M.S.T. de Castro, "Wear and surface residual stress evolution on twin-disc tests of rail/wheel steels", *Materials Science Forum*, Vols. 768-769, pp. 707-713, 2014.
- D.F.C. Peixoto, L.A.A. Ferreira, P.M.S.T. de Castro, "The Dang Van criterion for fatigue design", *Materials Science Forum*, Vols. 730-732, pp.555-560, 2013.
- D.F.C. Peixoto, L.A.A. Ferreira, "Fatigue crack propagation behavior in railway steels", *International Journal of Structural Integrity*, accepted, in press, 2013
- D.F.C. Peixoto, L.A.A. Ferreira, P.M.S.T. de Castro, "Application of the Dang Van fatigue criterion to the rail/wheel contact problem", *Materials Science Forum*, Vols. 636-637, pp. 1178-1185, 2010
- D.F.C. Peixoto, L.A.A. Ferreira, P.M.S.T. de Castro, "O critério de Dang Van para dimensionamento à fadiga: comparação com outros critérios", *Manutenção*, nº101, pp.22-27, 2009